CHIP-BASED SPECTROSCOPY USING MICRORESONATOR FREQUENCY COMBS

A Dissertation

Presented to the Faculty of the Graduate School

of Cornell University

in Partial Fulfillment of the Requirements for the Degree of

Doctor of Philosophy

by

Mengjie Yu

August 2018

CHIP-BASED SPECTROSCOPY USING MICRORESONATOR FREQUENCY COMBS

Mengjie Yu, Ph.D.

Cornell University 2018

The development of a spectroscopy device on a chip that could realize real-time, label-free and high-throughput detection of trace molecules presents one of the biggest challenges in sensing. This is particularly challenging in the mid-infrared (mid-IR) domain where strong and characteristic molecular absorption occurs but optical sources are still in full development. In the past decade, there has been a remarkable development of a miniaturized optical frequency comb source using parametric nonlinear interactions in microresonators. Such integrated devices present as unique tools for direct generation of broadband mid-IR light and ultrafast acquisition speed of molecular absorption information.

In this thesis, we address the microresonator technology for the generation of a broadband modelocked frequency comb in the mid-IR. The properties of such microcombs can be precisely controlled, tuned, and characterized. We show that microresonator-based combs is not only an ideal testbed for studying a variety of nonlinear dynamics but, more importantly, can be used to realize a silicon-based platform for vibrational spectroscopy. We demonstrate two different types of mid-IR microcomb-based spectroscopy, dual-comb spectroscopy, and scanning comb spectroscopy which are suitable for condensed phase study and trace gas sensing, respectively.

BIOGRAPHICAL SKETCH

Mengjie Yu was born in Nanchang, Jiangxi, China on December 3, 1991. She got a Bachelor of Optical Engineering degree from Zhejiang University in 2012. She then continued on the Ph.D program at School of Electrical and Computer Engineering at Cornell University in August 2012. She joined the Quantum and Nonlinear Optics Group under the guidance of Professor Alexander L. Gaeta in June 2013. In 2015, she moved to Columbia University with the group to continue her Ph.D research in New York City. Her graduate research includes chip-based mid-infrared frequency comb generation, comb spectroscopy, and other applications of microresonator-based nonlinear photonics.

To my parents, Shenghua Yu and Guoying Pan

ACKNOWLEDGEMENTS

First of all, I would like to thank my advisor, Professor Alexander L. Gaeta. He brought me into nonlinear photonics and is sharp, knowledgable and insightful so that we can always pursue the most cutting-edge research in the field with the best people and lots of freedom. He is also a very understanding and reliable person that I know he will always be there to support us.

I would also like to thank my committee members, Professor Michal Lipson and Professor Farhan Rana. As a pioneering scientist in silicon photonics, Michal is always very motivating and encouraging. Michal is also like a very good friend. I can always seek advice from her from life decisions to presentation skills. Prof. Rana taught very hardcore courses which I took most of them in Cornell. I enjoyed his teaching and learned a lot in quantum optics and solid state physics which lay a solid foundation in my future research. It is my honor to have both of Michal and Farhan to serve as my committee members.

I would like to thank the members of the Lipson Group. Especially, Dr. Austin Griffith has fabricated those great silicon devices which laid the foundation of our mid-infrared work and has taught me a lot on the experimentation. Dr. Steven Miller has become a good friend of mine, and I am happy that we have shared some exciting moments in the mid-IR lab. I would also like to thank Euijae Shim who recently joined the mid-IR family and has brought a lot of positive energy to me. Thank you to Dr. Raphael and Gaurang Bhatt for their great accompany in the lab during my years in Cornell. Thank you to Dr. Jaime Cardenas for his help in the SiC experiment. Thank you to Dr. Kevin Luke for teaching me the coupling skill. Thank you to Dr. Avik Dutt and Gaurang Bhatt as teammates for great jokes! I would also like to thank Dr. Aseema Mohanty who has helped me with the device modeling and has always been a very en-

couraging and heartwarming person. Thank you to William Ji who has been a very responsive and reliable friend.

I am so grateful and fortunate that I met the Gaeta Group family which has changed me, influenced me and shaped me into a better person. Writing this acknowledgement is particularly hard for me because it forces me to think of leaving the group. And my tears just can't stop falling. You are the people who I met almost every day and I shared so many memories with during the past five years. You are part of my life, and my family, and will always be. Special thanks to Ryan who always listens to me on the way back home from lab. Together with Xi, you have become very important friends to me. To Chaitanya who I have share the entire PhD years with, you are the friend that I always feel comfortable and relaxed wherever you are around. To Adrea, Gauri and Chaitali, we are the super girls in the group and I really enjoyed your accompany. To Jae, Alexander and Ara, you made the transition to Columbia much easier and happier. Lot of thanks to Prathamesh, Henry, Yun, Bok, Jared and Cecilia for the pleasure of working alongside all of you. Lastly, I would like to thank, my very best friend, Yoshi. We have come through from misunderstanding, disagreement and arguments to finally communications, respects and understanding. It has been quite a journey of the past five years and thank you for encouraging, supporting and believing in me no matter what happened. You are my best friend and best partner at work. And thanks for bringing Kai into my life, a kid with the magical power, who can always bring me the purest happiness.

Finally, I must thank my parents for their unconditional support and love throughout my life. I am so grateful that I am your daughter. Mum and dad, love you forever.

TABLE OF CONTENTS

LIST OF TABLES

LIST OF FIGURES

CHAPTER 1

INTRODUCTION

1.1 Nonlinear photonics

Nonlinear optics studies the phenomena where the optical properties of the material are modified in the presence of strong light field [1]. The optical response can be expressed by the polarization $\tilde{P}(t)$ as a function of the field strength $\tilde{E}(t)$

$$\tilde{P}(t) = \epsilon_0 \left[\chi^{(1)} \tilde{E}(t) + \chi^{(2)} \tilde{E}^2(t) + \chi^{(3)} \tilde{E}^3(t) + \cdots \right] \tag{1.1}$$

where $\chi^{(2)}$ and $\chi^{(3)}$ are known as the second order and third order nonlinear susceptibilities. While $\chi^{(3)}$ exists in all materials, $\chi^{(2)}$ only occurs in noncentrosymmetric media such as lithium niobate or gallium arsenide.

For decades, developing efficient nonlinear optical devices at low optical power has been one of the ultimate goals actively pursued by researchers. Silicon nanophotonics has emerged as a highly promising platform for such devices and for enabling massively parallel, monolithically integrated optoelectronic devices on a single chip. The key features of silicon photonics for nonlinear process are: first, there has been tremendous progress in fabricating ultra-low loss silicon-based waveguides and high Q-factor cavities over the past decade. Table 1.1 lists the propagation loss and Q-factor of some silicon-based platforms demonstrated for chip-based nonlinear interactions. Linear loss of a Si_3N_4 waveguide is 1 dB/m in the near-infrared (near-IR) and that of a silicon waveguide is 0.2 - 1 dB/cm in the mid-infrared (mid-IR) regime. Such low loss silicon-

Table 1.1: Linear loss parameters of silicon-based platforms.

Platfrom	**Dimension (nm) [width × height]**	**Linear loss (dB/cm)**	**Quality factor [cavity]**
Silicon-on-insulator (SOI)	2300 × 4000* [2]	0.2 @ 3.8 μm	1×10^6
	500 × 1400 [3,4]	0.7 @ 2.6 μm; 1.3 @ 3 μm	6×10^5; 2.5×10^5
Silicon-on-sapphire (SOS, air-cald)	480 × 2400 [5]	1.0 @ 4 μm	not applicable
	812 × 1500 [6]	0.7 @ 4.5 μm	2.8×10^5
Silicon nitride (oxide-clad)	730 × 2500 [7]	0.01 @1.55 μm	3.7×10^7
	730 × 10000 [7]	0.006 @ 1.55 μm	6.7×10^7
	600 × 3000 [8]	0.02 @ 1.55 μm	1.7×10^7
	950 × 2700 [9]	0.2 @ 2.6 μm	1×10^6

*air-clad

based nanowaveguides would allow for nonlinear process at sub-milliwatts optical power at near-IR and at tens of milliwatts at mid-IR.

Second, the Kerr nonlinearity of silicon or silicon nitride is orders of magnitude larger than that of glass. A change of refractive index that is proportional to the optical intensity is called optical Kerr effect, which can be expressed as $\Delta n = n_2 \times I$ where Δn is the refractive index change, n_2 is nonlinear index and I is optical intensity. n_2 is an optical constant that characterized the strength of the optical nonlinearity. It can be expressed based on the third order nonlinear susceptibility, $n_2 = 3\chi^{(3)}/4n_0^2\epsilon_0 c$ where n_0, ϵ_0 and c denote the linear refractive index, the electrical permittivity and the speed of light. Table 1.2 lists the nonlinear index n_2 of different materials that has been used to demonstrate the Kerr effect in an integrated platform. Glass (silica) which is often used for the optical fiber is listed as a comparison. As shown in Table 1.2, Si (or Si_3N_4) has 100 times (or

Table 1.2: Material properties

Material	**Linear refractive index [n_0]**	**Nonlinear index [n_2] (m^2/W)**	**Transparency window (μm)**
Silica	1.45	3×10^{-20}	0.2 - 4
Si	3.47	5.0×10^{-18}	1.2 - 8
Si_3N_4	2.0	2.5×10^{-19}	0.4 - 4.6
CaF_2	1.4	1.9×10^{-20}	0.12 - 10
MgF_2	1.4	1.0×10^{-20}	0.13 - 7.7
Al_3N_4	2.12	2.3×10^{-19}	0.2 - 13.6
Diamond	2.38	0.8×10^{-19}	0.23 - >50
AlGaAs	3.3	2.6×10^{-17}	0.7 - 17
GaP	3.05	6.0×10^{-18}	0.54 - 10.5
$LiNbO_3$	2.21	1.8×10^{-19}	0.35 - 5.2
Ge*	4.04	4.4×10^{-17}	1.8 - 15
SiC	2.6	8.6×10^{-19}	0.4 - 5.6

Al_3N_4, AlGaAs, GaP and $LiNbO_3$ have $\chi^{(2)}$ nonlinearity; Parameters for 1.5 μm except for *, * at 3 μm

10 times) larger nonlinear index than glass.

Third, tight confinement of light in the waveguide core further reduces the threshold power and enables tuning of the dispersion. Group-velocity dispersion (GVD) is an important parameter for achieving the phase-matching conditions for parametric nonlinear optical processes such as four wave mixing (FWM).

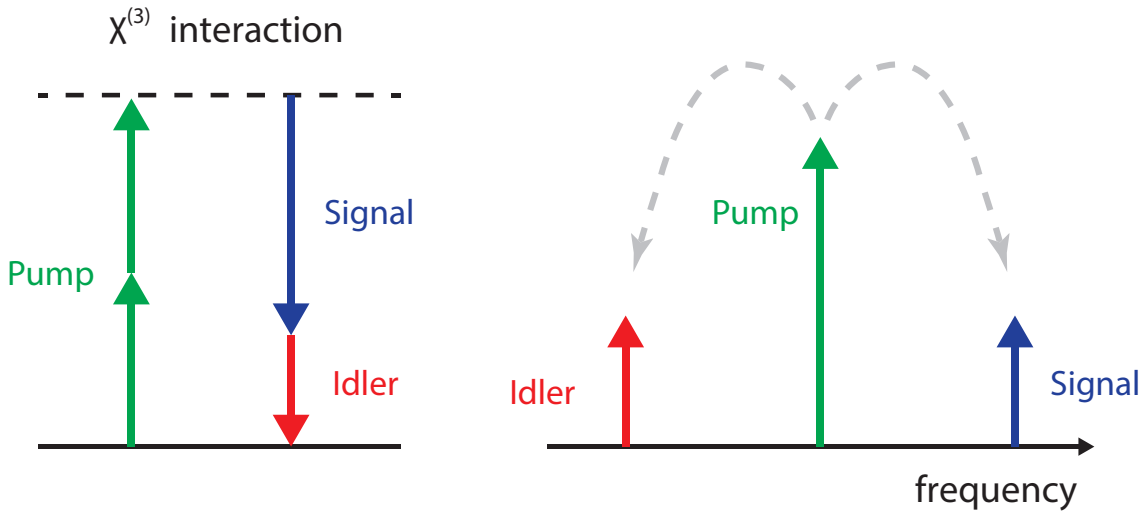

Figure 1.1: The scheme of degenerate four wave mixing process

1.1.1 Four wave mixing

FWM is one example of a $\chi^{(3)}$ process. Figure 1.1 shows the scheme for degenerate FWM where two degenerate pump photons (w_p) are annihilated to generate one signal photon (w_s) and one idler photon (w_i) . The amplification of the light at signal/idler frequencies is called parametric gain which can be achieved if both energy conservation and momentum conservation are satisfied. The energy conservation is $2w_p = w_s + w_i$, and momentum conservation requires wave vector matching (phase matching): $2k_p = k_s + k_i$.

$$\begin{aligned} \Delta k &= 2k_p - k_s - k_i \\ &= -2 \sum_{n=2,4,\ldots} \frac{\beta_n}{n!} \Omega^n - 2\gamma P. \end{aligned} \tag{1.2}$$

where γ is the nonlinear parameter, Ω is the sideband detuning ($|w_p - w_s|$), P is the pump power and β_n corresponds to the n$^{\text{th}}$-order dispersion coefficients of

the Taylor expansion of the propagation constant.

Typically Ω is small, so all the higher order dispersion terms $\sum_{n=4,6...} \frac{\beta_n}{n!}\Omega^n$ is negligible compared to $\frac{\beta_2}{2}\Omega^2$. In order to achieve the phase-matching condition ($\Delta k = 0$), anomalous GVD ($\beta_2 < 0$) is required for the degenerate FWM process.

1.1.2 Dispersion engineering

Dispersion engineering is a powerful technique in silicon photonics. The effective refractive index is very sensitive to small changes in the waveguide dimensions due to the tight confinement of light. Therefore, it is possible to engineer the waveguide dispersion to compensate/modify the intrinsic material dispersion by simply changing the cross-section of the waveguide. Figure 1.2 plots the GVD of oxide-cladded Si and Si_3N_4 waveguide with 3 different cross-sections. Dispersion engineering allows for achieving anomalous GVD at a wide range of operating wavelength from the visible to mid-IR regime even when the GVD of bulk material is strongly normal. It offers great flexibility of pump wavelengths for which parametric oscillations could happen.

1.1.3 Microresonator-based frequency comb

An optical frequency comb (OFC) [10, 11] is a broad optical spectrum consisting of evenly spaced, spectrally narrow lines. The frequency of each comb line can be written as $f_m = f_{ceo} + m\Delta f$, where f_{ceo} is the carrier-envelope offset frequency and Δf is the comb line spacing (Fig. 1.3). It provides a coherent link between the radio-frequency and optical domains and offers a precise and ac-

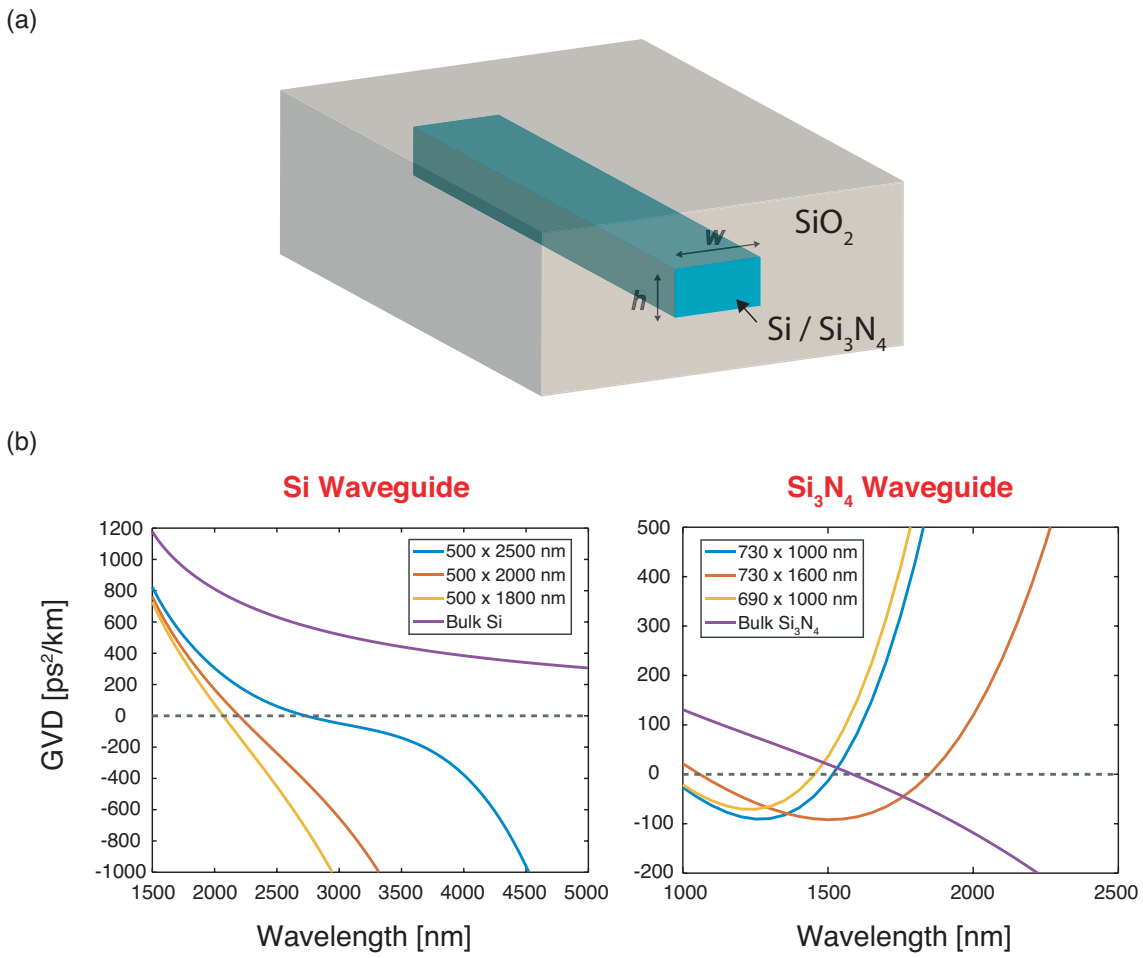

Figure 1.2: (a) Oxide-cladded Si/Si_3N_4 waveguide. The high index contrast between the core (3.5/2) and the cladding (1.5) results in the tight confinement of light in the waveguide. The waveguide dimension is height × width. (b) Dispersion engineering via changing the waveguide dimension.

curate means of counting the optical cycle (10^{-15}s) used as optical clocks. With its broadband spectrum which consists of a large number of precise and controllable frequency components, OFC has enabled a wide range of applications including optical communication, precision metrology, LIDAR, astronomical spectrograph calibration, remote sensing, and low-noise microwave generation. OFC technology has become mature and even commercialized since its discov-

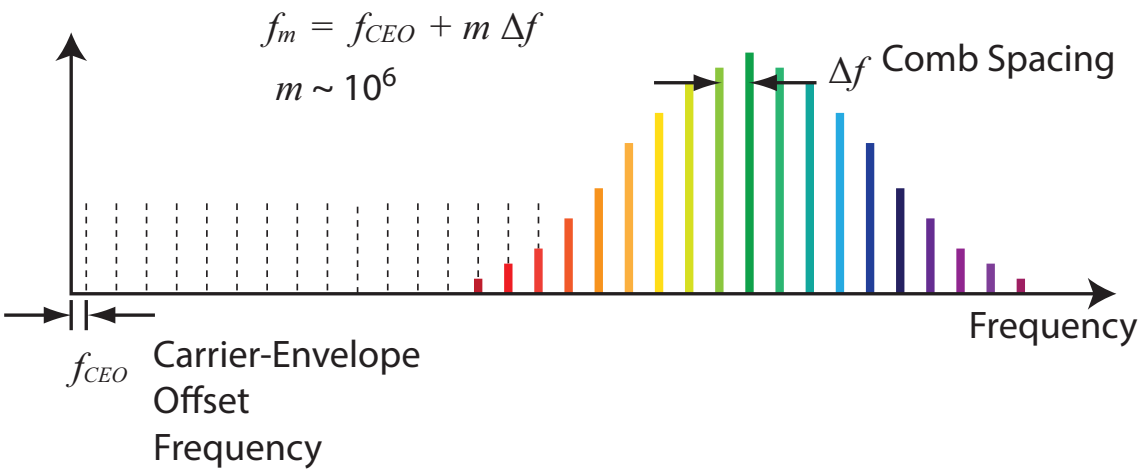

Figure 1.3: Optical frequency comb. The comb-line frequencies can be expressed using $f_m = f_{ceo} + m\Delta f$, where f_{ceo} is the carrier-envelope offset frequency and Δf is the comb line spacing.

ery two decades ago based on modelocked femtosecond lasers (*e.g.* Ti sapphire laser, Er-doped and Yb-doped fiber laser). Such OFC usually has relatively low line spacing (~ MHz range), limited operating wavelength and bandwidth determined by the gain medium, and large footprints.

The past decade has witnessed the emergence of chip-scale OFC sources based on a high-Q microresonator pumped with a continuous-wave (CW) laser (Fig. 1.4). Compared to the conventional OFC technology, microresonators offer full wafer-scale integration and enable octave-spanning OFC's at low optical power level through parametric frequency conversion [12, 13] and dispersion engineering that enables operation over different spectral windows [14]. Such miniature OFC's have been demonstrated in a wide range of microresonator platforms from the visible [15], near-IR [12–14, 16–30], and mid-IR [3, 9, 31, 32]. Recently, applications based on microresonators have been unlocked beyond fundamental laboratory studies, including microwave generation [33], dual-comb spectroscopy [34–37], light detection and ranging [38, 39], optical fre-

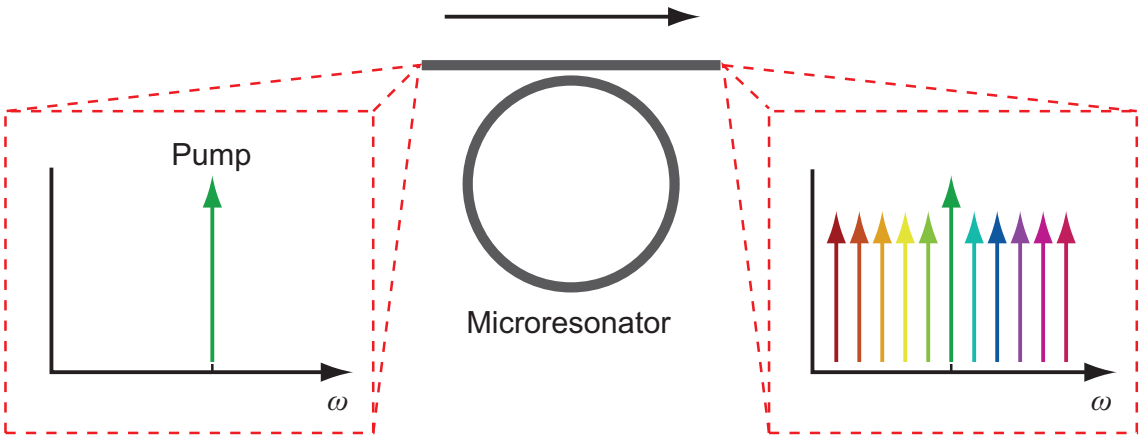

Figure 1.4: Microresonator-based frequency comb is generated through parametric oscillations by detuning a single-frequency pump laser into a cavity resonance.

quency synthesizer [40], terabit coherent communications [41], and astrocomb for exo-planet searches [42, 43].

1.1.4 Modelling: Lugiato-Levefer equation

The dynamics of microresonator-based OFC generation can be modeled with the modified Lugiato-Levefer equation (LLE) [44–49] shown in eq. 1.3. Besides the term of linear round-trip loss α, pump-cavity detuning δ_0, and dispersion β_n, the generation process goes through nontrivial nonlinear interactions, including the effect of free-carrier dispersion (FCD) and absorption (FCA), FWM, self-phase modulation, cross-phase modulation, self-steeping, Raman, and multi-photon absorption.

$$
\begin{aligned}
T_R \frac{\partial E(t,\tau)}{\partial t} = \Bigg[& -\alpha - i\delta_0 + iL \sum_{n\geq 2} \frac{\beta_n}{n!} \left(i \frac{\partial}{\partial \tau} \right)^n - \frac{\sigma L}{2} (1 + i\mu) N_c(t,\tau) \\
& + \left(1 + \frac{i}{\omega_0} \frac{\partial}{\partial \tau} \right) \Bigg(\int_0^\infty i\gamma L R(t') |E(t-t',\tau)|^2 dt' \\
& - \sum_{n=2,3,4} \frac{\beta_{nPA} L}{n A_{eff}^{n-1}} |E(t,\tau)|^{2n} \Bigg) \Bigg] E(t,\tau) + \sqrt{\kappa} E_{in}
\end{aligned}
\tag{1.3}
$$

where T_R is the round-trip time; $E(t,\tau)$ is the field in the microresonator; t, τ correspond to the slow and fast time variables; L is the cavity length; μ and σ are the FCD parameter and FCA cross section; N_c is the FC density; γ is the nonlinear parameter; $R(t)$ is the Raman response; β_{nPA} is the n-photon absorption coefficients; A_{eff} is the effective area of the waveguide mode; κ is the power transmission coefficient of the bus-waveguide-microresonator coupling region; E_{in} is the input field.

The most well-known solution of Eq. 1.3 is called temporal cavity soliton (CS's), which is self-localized pulses of light that can be excited in nonlinear optical resonators. Temporal CS's were first studied experimentally in fibre cavities [50–53] and subsequently reported in optical microresonators [12, 16, 20–22, 32]. Mathematically, temporal CS's are a steady-state localized solution of the LLE [44] which has been extensively used to model driven nonlinear optical resonators [47, 49–51, 54–60]. Figure 1.5 shows a single-soliton modelocking state which corresponds to a single pulse circulating per roundtrip with a sech^2 spectral profile. This state is a coherent, low-noise state where features narrow comb linewidth and phase-locked comb lines and is crucial for comb applications which require high frequency precision, accuracy, and stability. Over the past few years, soliton-modelocking has been achieved in various

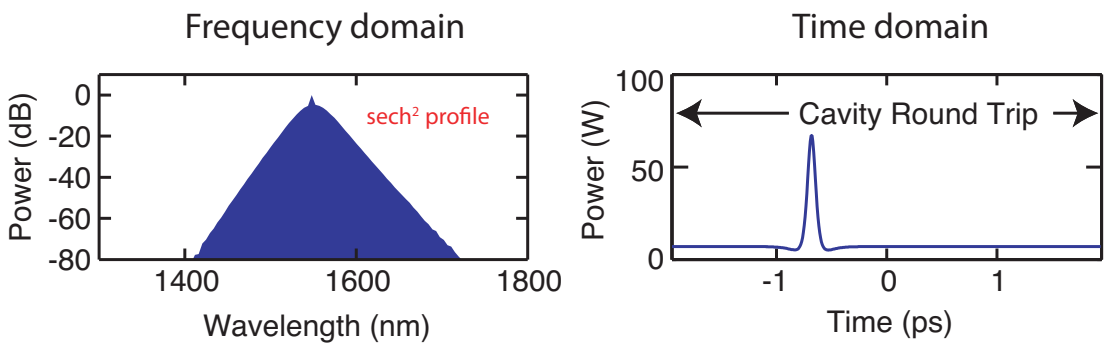

Figure 1.5: The frequency and temporal domain of temporal cavity soliton in a continuous-wave laser-driven nonlinear cavity.

platforms including fluoride, silica, Si_3N_4, and silicon. Achieving the single-soliton state is often challenging and not straight forward. Since the pump is effectively red detuned and the soliton is effectively blue detuned from the resonance, large thermal shift of the cavity resonance has to be overcome to reach the soliton state via pump-power modulation [22] or thermal kick [21]. Several other deterministic way to single-soliton state have recently demonstrated by using phase modulation [61], pulse pump laser [62], and mode-crossing effects [63]. In addition, several interesting platforms which has a $\chi^{(2)}$ nonlinearity, such as $LiNdO_3$, Al_3N_4, and GaP, have shown parametric oscillations [18,28,64], which can combine electrical tuning and switching with OFC source and enable second-harmonic generation and electric-optic comb generation [64]. There has been also a very recent breakthrough in integrating the entire comb source on chip using a semiconductor optical amplifier chip coupled into an 8M Q-factor Si_3N_4 microresonator, which has enabled a battery-powered miniaturized comb source [65].

1.2 Mid-infrared frequency comb

Mid-IR spectral regime is a gold mine for vibrational spectroscopy where molecular absorption is typically 10 to 1,000 times greater than those in the visible or near-IR offering the potential to identify the presence of substances with high sensitivity and selectivity. Development of mid-IR optical sources is primarily motivated by spectroscopic applications. This is a vivid and dynamic field which also includes combination with instrumental techniques such as attenuated total reflectance, microfluidic devices, microscopy, *etc.*, and it addresses a wide range of applications in chemistry, bio-medicine, material science, environmental monitoring, industrial process control, *etc.*.

However, optical sources in the mid-IR are still in full development, along with high-speed photodetector, low-cost detector arrays and other optical components. Compared to tunable lasers, OFC's that spans over a broad spectrum can enable massive and parallel detection of multiple molecular species. However, extension of OFC's into the mid-IR has proven to be challenging. Nonlinear optical processes, such as difference frequency generation [66–69] and optical parametric oscillation [70–73], are often used to convert an OFC from the near-IR to the mid-IR with additional system complexities. Recently, there has been significant progress and development of modelocked lasers in the mid-IR [74,75]. The techniques above often suffer from limited conversion efficiency and bandwidth, complex and large footprints, or the limited operating wavelength determined by the available gain medium.

Microresonator-based OFC has emerged as a promising platform for direct generation of broadband mid-IR light in a much more compact device. Mid-

IR silicon photonics can potentially enable on-chip spectroscopy and sensing with broad bandwidth, low power consumption, massive scalability, and monolithical integration with CMOS electronics. Moreover, it holds great potential, through combining with a quantum cascade laser, to realize a spectroscopy device on a chip that could realize real-time fingerprinting with label-free and high-throughput detection of trace molecules. As such, microresonator-based OFC's represents a novel direction for vibrational spectroscopy, in applications where traditional combs based on *e.g.* mode-locked laser systems are not suited.

1.2.1 Material property and loss mechanism

The first rule of material selection is the material transparency window. Most of the material listed in table 1.2 can transmit light into the mid-IR besides glass (SiO_2). SiO_2 is often used as the standard cladding material for SOI or Si_3N_4 waveguides. Pumping beyond 3 μm in such waveguides suffers significant linear losses due to the optical mode overlapping with the cladding, thus increasing the threshold power. It also limits the overall bandwidth of OFC's beyond 4 μm. An alternative solution to extend the bandwidth beyond 4 μm will be to use different cladding materials, suspended structures, or large cross-section SOI (air-clad on top) to minimize the overlap with the substrate. In addition, the presence of water (or O-H band) during the fabrication process results in additional linear losses that correspond to the water absorption features, such as 1.9 μm and 2.7 μm. High temperature annealing may be needed if pumping nearby. Secondly, the nonlinear loss, such as multi-photon absorption (MPA) and FCA, needs to be taken into account. Si_3N_4 has a bandgap of 5 eV (250 nm), thus MPA is negligible when pumping in the mid-IR (> 2.5 μm). Silicon has

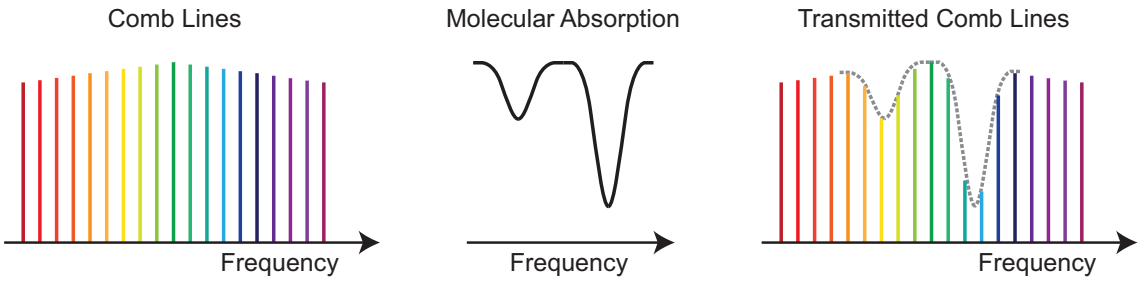

Figure 1.6: Molecule fingerprinting. The comb spectrum is sent through sample molecules. The unique absorption features will be imprinted on the transmission comb spectrum. A large spectral bandwidth will enable identification of multiple molecular species.

a bandgap of 1.1 eV (1.1 μm), suffering from two-photon absorption between 1.1 and 2.2 μm, and three-photon absorption between 2.2 and 3.3 μm [76]. At the same time, free carriers generated by the absorbed photons result in higher losses at longer wavelengths due to intra-band absorption. Thirdly, higher index contrast between the core and the cladding offers more flexibility to engineer the waveguide dispersion. Also, the higher the refractive index, the higher the nonlinearity, and the lower the threshold power. At last, factors *e.g.* fabrication process/quality, the damage threshold, thermal conductivity, and material structure (crystalline or amorphous) should be considered in terms of power budget, operating procedures, and device design.

1.3 Comb spectroscopy

A broadband comb spectroscopy system allows for accurate detection of molecule species in a complex environment [77]. As shown in fig. 1.6, the transmission of the comb spectrum is measured to obtain the molecular absorp-

tion information. A complete system involves an OFC source, the absorption cell, and detection techniques. The basic performance metrics will be operating wavelength regime, spectral bandwidth, frequency resolution, accuracy, acquisition rate, signal-to-nose ratio, and the compactness of the system. One of the challenges of comb spectroscopy is to find an ideal combination of the comb source and the detection technique so that the frequency accuracy and resolution provided by either the OFC or the detection instruments will not be wasted. Developing a spectroscopy technique suitable for the target application requires trade-off among performance metrics. In terms of comb source, important parameters are the comb linewidth, the bandwidth, the line spacing, and the comb line power. Detection techniques include grating-based spectrometer, virtually imaged phase arrays (VIPA), Michelson-based Fourier transform spectrometer (FTIR), and dual-comb spectrometer. A grating-based spectrometer is equipped with a mechanically scanning grating with a photodetector which typically has 0.01 - 5 nm spectral resolution in the near-IR. VIPA spectroscopy has demonstrated a spectral resolution as low as 1 GHz in the visible range but requires a focal plane array of detectors for acquisition. An FTIR measures the Fourier transform of the interferogram by varying the optical delay and uses a single detector and is versatile in spectral coverage. The typical resolution range of an FTIR is 0.1 - 30 GHz where a higher resolution requires a longer mechanical delay arm and thus a larger footprint. A dual-comb spectrometer takes advantages of heterodyning two slightly different OFC's to achieve rapid acquisition rates, overcoming the limitation of a long optical path in an FTIR [78]. Also, absorption material could be in gas, liquid, or solid state phase. Typically the absorption of the liquid/condensed-phase has much broader linewidth (~100 GHz range) than it of the gas-phase (~100 MHz range). For direct comb spec-

troscopy in general, it is advantageous that the comb line spacing is of the same order of magnitude (or slightly smaller) as the desired spectral resolution.

1.4 Organization

This dissertation focuses on the development and applications of microresonator-based frequency combs in the mid-IR regime. Chapter 2 presents the generation of a mid-IR modelocked optical frequency comb in a silicon microresonator. We explore two ways towards soliton modelocking via pump-laser tuning and free-carrier dispersion. Chapter 3 presents part of the rich nonlinear dynamics in soliton microcombs, breather solitons, which exhibits temporally oscillatory behavior. Chapter 4 and 5 introduces two ways of microcomb spectroscopy: dual-comb spectroscopy which enable rapid acquisition of molecule absorption spectrum in the liquid/condensed phase, and tunable modelocked microcomb spectroscopy which boosts the spectral resolution to the comb linewidth suitable for trace gas sensing. Chapter 6 proposes a novel and robust approach for microcomb gas-phase spectroscopy without using an external pump laser. We conclude with a summary in Chapter 7 and point out some exciting future directions based on the mid-IR microresonator-based comb. Appendix explores the influence of Raman scattering on comb generation in crystalline microresonators.

CHAPTER 2

SOLITON MODELOCKED MID-INFRARED FREQUENCY COMBS

2.1 Introduction

Optical frequency comb generation using four-wave mixing (FWM) parametric oscillation in microresonators has attracted significant interest [12, 13, 16, 19, 23, 24, 79–84]. Progress in fabrication techniques for low-loss nonlinear devices has lead to significant development of comb generation in the mid-infrared (mid-IR) regime [3, 4, 6, 9, 31, 85], which is a highly attractive spectral region for applications in molecular spectroscopy and chemical and biological sensing [86]. For example, broadband mid-IR sources, especially from 3 to 4 μm, are useful for breath analysis, since many different species are exhaled, such as carbonyl sulfide, ethane, ethylene and formaldehyde, which are important biomarkers for various diseases. Mid-IR parametric oscillation and frequency comb generation have been demonstrated in silicon nitride (Si_3N_4) [9], silicon [3, 4] microresonators, and crystalline calcium fluoride and magnesium fluoride resonators [31, 85]. Various spectroscopic techniques could be enabled by broadband coherent comb sources, including multi-heterodyne and dual-comb spectroscopy that yield high sensitivity and fast acquisition speeds [87–89].

A critical feature of microresonator-based combs is that they can be modelocked, which results in the comb spacing to be highly uniform across the entire comb. Recently, there have been several demonstrations of such modelocking in the near-infrared regime [12, 16, 20, 22, 90–92]. To achieve modelocking, the microresonators are pumped in the anomalous group-velocity dispersion (GVD) regime, and soliton formation is controlled via pump frequency detun-

ing with respect to the cavity resonance. Several additional tuning methods have been demonstrated, including pump power modulation [12], electro-optic tuning based on the Pockels effect [18], and thermal tuning of the cavity resonance [21], which allow for stable, systematic generation of single-soliton states. Soliton formation techniques not involving pump frequency tuning are particularly attractive, since it would allow for the use of ultra-narrow linewidth frequency-stabilized single-frequency pump sources for comb generation and enable simultaneous generation of frequency combs in multiple rings using a single pump source, which would facilitate applications such as chip-scale dual-comb spectroscopy [93].

In this paper, we present the first demonstration of coherent mid-IR frequency comb generation via soliton modelocking in silicon microresonators. The evolution towards temporal cavity soliton formation and modelocking is numerically simulated including effects of multiphoton absorption (MPA), free-carrier dispersion (FCD), and free-carrier absorption (FCA). Experimentally, the dynamics are carefully characterized by comb transmission and three-photon absorption (3PA)-induced photocurrent measurements. Modelocking is found to be reproducible at different pump wavelengths and in multiple silicon devices and is repeatedly achievable by appropriate tuning of the pump laser frequency. A 40 % power conversion from the pump to the modelocked comb is achieved. Furthermore, we demonstrate full control of the modelocking dynamics through electrical tuning of the free-carrier (FC) lifetime, allowing for fixed-pump-frequency operation. Our results show that the distinct features of silicon, which are high nonlinearity, high thermal conductivity, MPA and the FC-induced effect, can be suitably exploited for modelocked broadband mid-IR frequency comb generation.

2.2 Device design

For comb generation in the mid-IR, we use a silicon microresonator with an integrated PIN diode. We fabricate our devices using an etchless process that uses thermal oxidation instead of reactive-ion etching to form the waveguide core [3, 94]. The microresonator has a free spectral range (FSR) of 127 GHz and is dispersion engineered to have anomalous GVD beyond 3 μm for the fundamental TE mode, which enables comb generation [Fig. 2.1(c)]. We characterize an overcoupled resonance of a silicon microresonator at 3.1 μm wavelength and measure a loaded quality factor of 60,000, corresponding to an intrinsic quality factor of 250,000 [Fig. 2.1(d)]. Silicon suffers from 3PA in the 2.2 to 3.3 μm wavelength regime, and the generated photocarriers can cause significant FCA for long carrier lifetimes. To mitigate this, the silicon microresonators are embedded in an integrated PIN diode to enable extraction of the generated free carriers [95, 96], which is critical for mid-IR frequency comb generation in silicon [3, 97] . When a reverse-bias voltage is applied to the PIN junction, carriers are swept out of the diode depletion region. The electrical contacts for the PIN diode are spaced 4.4 μm apart, with the etchless waveguide in the center.

2.3 Modelocking via Pump Detuning

2.3.1 Numerical Simulations

We carry out numerical simulations on the nonlinear dynamics of comb generation in silicon microresonators using a modified Lugiato-Lefever model

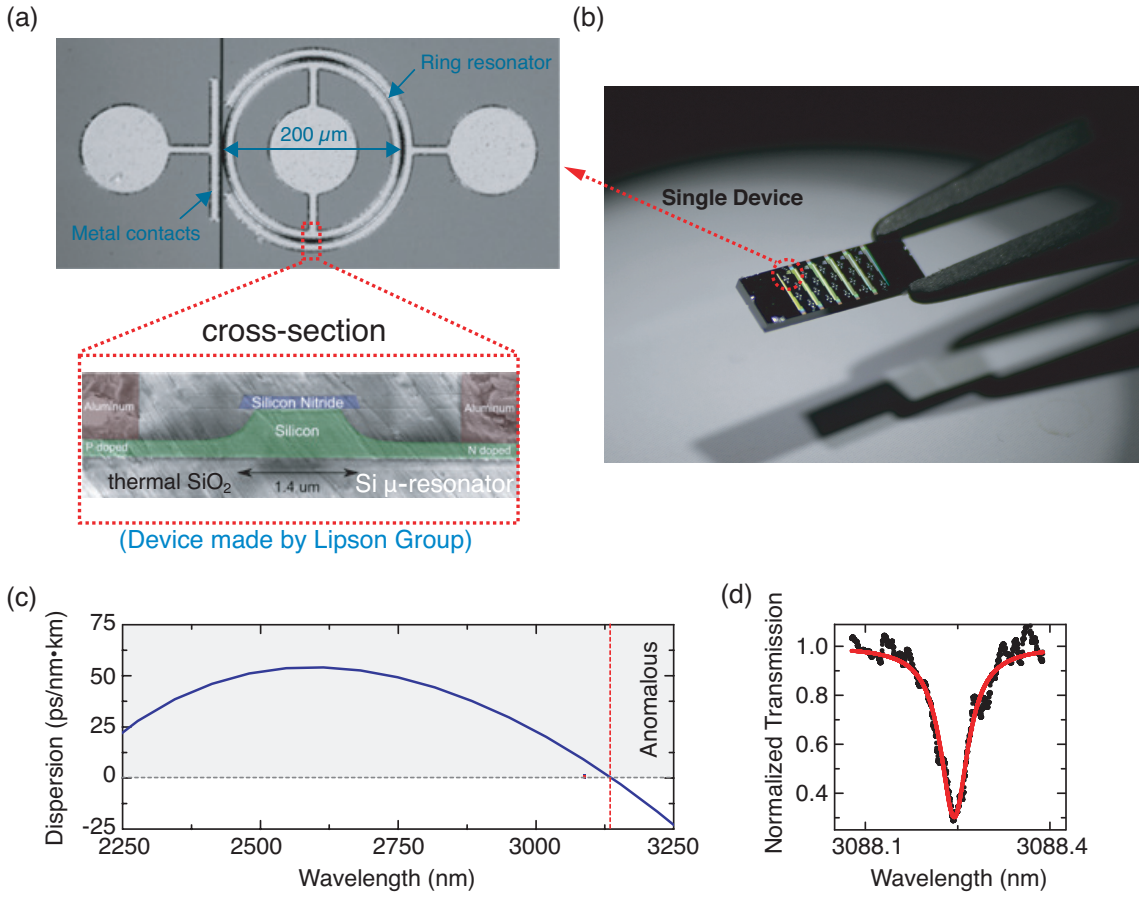

Figure 2.1: (a) Optical microscope image of a ring resonator and metal contacts fabricated using the etchless process (top). False coloured cross-sectional SEM image (bottom) of silicon waveguide, doped regions and metal contacts. (b) The image of the silicon chip (with a carbon-fiber-tip tweezer) which consists of 20 silicon microresonator devices. (c) The simulated dispersion parameter of the etchless waveguide. The zero group-velocity dispersion wavelength is depicted with a dashed red line. (d) We characterize an overcoupled microresonator at 3.1 μm with a loaded quality factor of 60,000. The resonance is confirmed to be overcoupled by using the PIN diode to inject carriers into the resonance, and observing an increase in the resonance extinction. This equates to an intrinsic Q factor of 250,000.

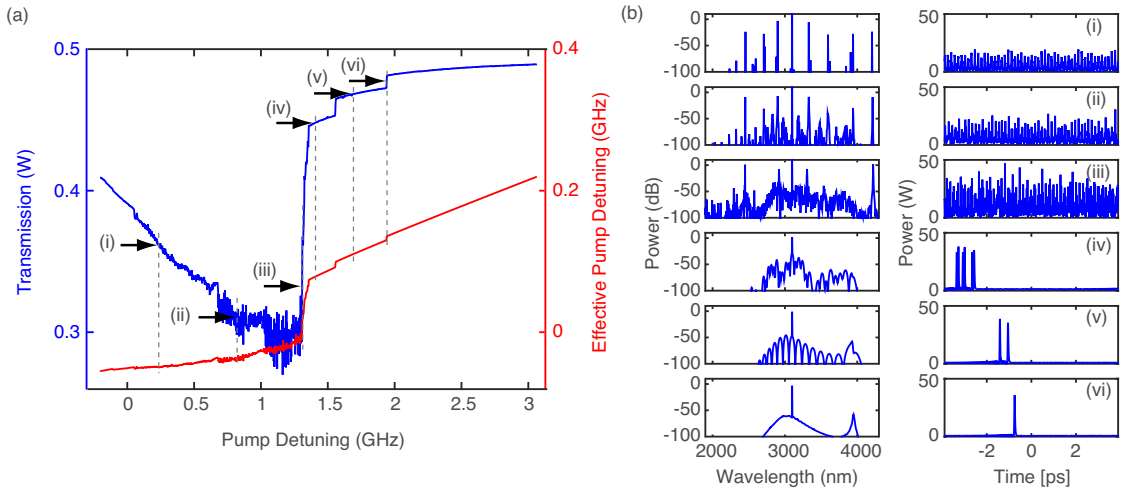

Figure 2.2: Numerical simulation of soliton formation via pump laser detuning in a silicon microresonator. a) Transmission and effective pump-cavity detuning when scanning a pump laser over a cavity resonance. Effective pump-cavity detuning subtracts the resonance shift due to the Kerr effect and free-carrier dispersion from pump detuning. A series of abrupt transmission steps occur in the effective red-detuning regime. b) Optical spectra and intracavity temporal behavior at different positions (i-vi) in the scan. The plots associated with (i-iii) are in the effective blue-detuning regime while plots (iv-vi) are in the effective red-detuning regime. The transition to modelocking and soliton formation occurs between (iii) and (iv), as the pump frequency is tuned across the zero effective pump detuning point. As the laser is tuned, (i) primary sidebands are generated through modulation instability and cascaded FWM, (ii) mini-combs are generated around each primary sideband, (iii) with further intracavity power building up, different sets of mini-combs overlap producing high-noise temporal behavior, (iv) a multiple (6) soliton state occurs with a complex, structured optical spectrum, (v) a 2-soliton state is produced, and (vi) the single soliton state with a smooth optical spectrum is reached. States with a different number of solitons correspond to the transmission steps shown in (a).

[44–49, 97, 98]. Based on the device structure of the silicon microresonator described in [3], the simulated GVD is anomalous (-102 ps^2/km) for a fundamental TE mode at a pump wavelength of 3.1 μm. Higher-order dispersion,

self-steepening, 3PA, and the FC effect (FC lifetime τ_{fc}=100-ps) are included in the model. Figure 2.2(a) shows the optical transmission and the effective pump-cavity detuning as functions of pump detuning from the cold cavity resonance. The effective pump-cavity detuning is calculated by subtracting self-phase modulation, cross-phase modulation and the FC-induced phase shift from the pump detuning from a cold-cavity resonance. For our simulations, we operate in the undercoupled regime. The evolution of the optical spectra and temporal behavior [Fig. 2.2(b)] indicates that the soliton state occurs after a transition from a high-noise state and results in high peak power pulses at red effective pump detunings, which coincides with the transmission steps and is consistent with previous observations in other platforms [16,21,22].

Our simulations indicate that the soliton states are achieved at high optical transmission, corresponding to values close to the off-resonance transmission. This condition is attributed to high pump power and low pump-to-comb conversion efficiency, which is defined as the soliton power divided by the minimum pump power for soliton formation. In practice, this results in a significant change in the intracavity power when the comb undergoes a transition to the soliton state, resulting in a sudden resonance shift due to thermal effects which is not included in this model. This thermal shift can affect the allowable range of pump detunings for stable soliton operation, especially in silicon due to its high thermal conductivity and short heat dissipation time. This issue can be overcome, for a given Q factor and FSR by operating in the over-coupled regime of the resonator with low pump power, which allows for high pump efficiency and minimal change in the intracavity power when transitioning to the soliton state [22]. In addition, operation in the over-coupled regime alleviates the requirements of some complex techniques used in Si_3N_4, MgF_2, and silica mi-

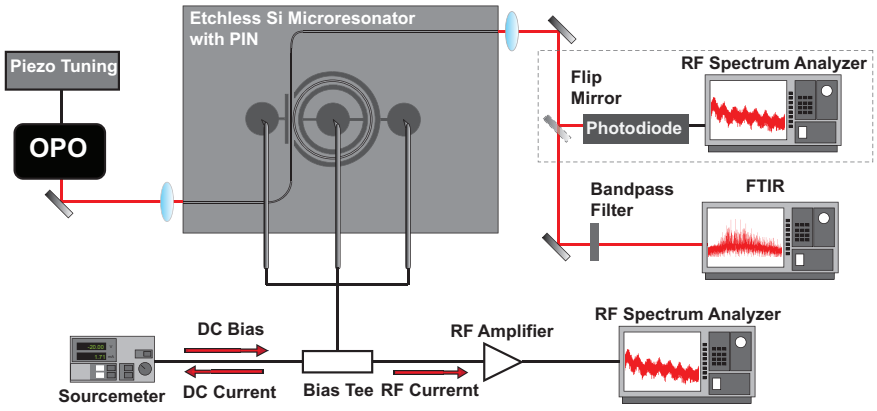

Figure 2.3: Experimental setup for generation and characterization of mid-IR frequency comb in silicon microresonators. We pump a silicon microresonator using a cw optical parametric oscillator (OPO). The output is collected using an FTIR. We monitor the RF noise using a conventional photodiode and a PIN diode.

croresonators to overcome the transient instability of the states, such as two-step protocol [12] or searching for an ideal tuning speed of the pump laser [16].

2.3.2 Experimental Demonstration

The experimental setup is shown in Fig. 2.3, similar to [4], in which we pump the silicon microresonator with a continuous wave (cw) optical parametric oscillator (Argos Model 2400). The optical spectrum and both the DC and RF components of the extracted 3PA-induced current are monitored simultaneously using an FTIR, a Keithley Sourcemeter, and an RF spectrum analyzer, respectively. A unique property of silicon microresonator frequency combs is that the intracavity dynamics can be characterized by the RF modulation in the PIN junction arising directly from 3PA-induced photocurrent [4]. Any RF modulation of the optical field is imprinted on the FC density and thus on the photocurrent.

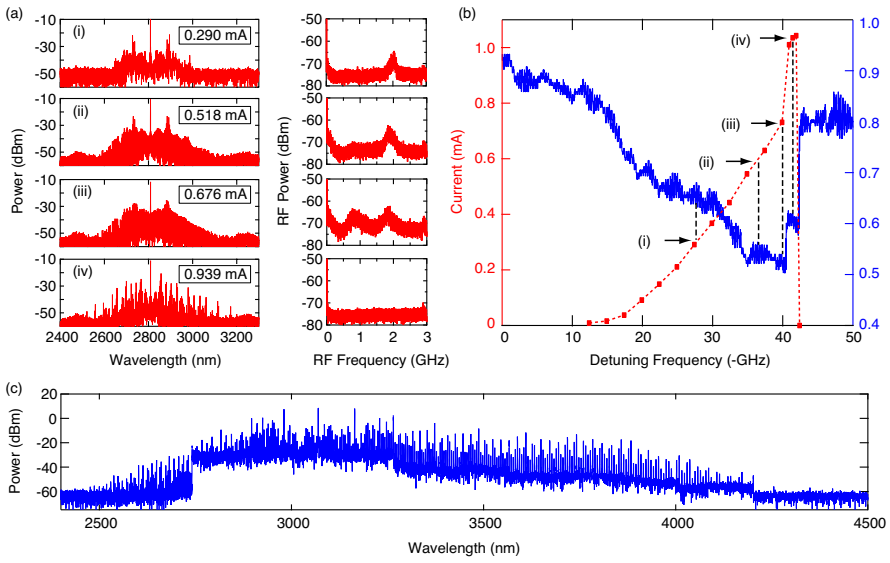

Figure 2.4: The evolution towards modelocking via pump frequency detuning from the cavity resonance. (a) Left: Optical spectrum. Right: RF spectrum of the 3PA-induced current. (b) Transmission (blue solid curve) and 3PA-induced current (red dashed curve) as the pump frequency is scanned. Arrows correspond to four states (i-iv) in (a). (c) Optical spectrum of soliton mid-IR frequency comb pumped at 3.07 μm.

Therefore, we are able to examine the comb dynamics using the PIN diode, similar to using a conventional photodiode. The design of this PIN-based detector achieves a high bandwidth as compared with conventional photodiodes due to the short FC lifetime. For example, τ_{fc}=12 ps is achievable when at a reverse-bias voltage of -15 V, which yields a bandwidth of 13 GHz for this PIN-based detector.

The measured loaded Q factor of the silicon microresonator is 245,000 at 2.8 μm. The device is overcoupled at 2.8 μm, which we verify by measuring a reduced extinction factor when a reverse-bias voltage is applied on the PIN junction and observing a decreased nonlinear loss due to FCA inside the cavity. We generate frequency combs by tuning the cw pump laser at 2.8 μm into resonance

at a reverse-bias voltage of -20 V. The measured threshold power for parametric oscillation is 8 mW, which is consistent with the predicted value based on the Q factor [99], and the off-resonance pump power in the bus waveguide for soliton modelocking is 35 mW. The comb generation dynamics as the pump power is increased are shown in Fig. 2.4(a). In Fig. 2.4(a)(i)-(iii), the pump power builds up inside the microresonator, resulting in an increase in DC current. During this process, primary sidebands are formed through modulation instability and cascaded FWM. With further power buildup, mini-comb formation occurs near each of the primary sidebands and results in a loss of spectral coherence creating multiple broad RF beat notes and high RF amplitude noise [Fig. 2.4(a)(i-iii)]. Finally, the frequency comb state abruptly transitions to a low-noise state with a more structured optical spectrum [Fig. 2.4(a)(iv)]. More importantly, the transition coincides with an abrupt increase in the DC current from 0.676 mA to 0.939 mA, which is a strong indication of pulse formation inside the cavity, since the 3PA-induced current is proportional to the cube of temporal peak power. In addition, we slowly scan the pump frequency at a 0.1 Hz rate across the resonance while monitoring the transmission using an amplified PbSe detector, as shown in Fig. 2.4(b). The transmission shows a clear step, which deviates from the expected triangular resonance shape, due to the large Kerr shift induced by intracavity soliton formation [16] and is well predicted by our simulations (Fig. 2.2). Moreover, the position of the transmission step corresponds to the abrupt change in current. The fact that the current increases despite the decrease in intracavity average power, is another strong indication of soliton formation.

As discussed previously for other platforms [12, 16], the excitation of stable soliton states is often complicated by the thermal nonlinearity of the resonator. Silicon has a large thermal-optic effect in the mid-IR and a large thermal diffu-

sivity (10 times larger than Si_3N_4), which makes the thermal instability in the microresonator more detrimental than in other platforms. Despite the thermal effect, the final multi-soliton state can be reached with a slow scanning speed and can be repeatedly achieved by manually tuning the pump laser. This is attributed to operating in the overcoupled regime with a relatively low pump power, where soliton formation can still be achieved due to the large nonlinearity of silicon. Further optimization of the parameters to reduce the transient thermal instability may allow for the observation of multiple soliton steps. In our case, the number of observable steps is limited by the response of the lock-in detection and the scanning speed of the pump laser.

Next, we obtain a modelocked mid-IR frequency comb with near-octave spanning spectrum spanning 2.4 - 4.3 μm by pumping at 3.07 μm with 80 mW in the bus waveguide [Fig. 2.4(c)]. In the frequency domain, the comb spans from 70 THz to 121 THz, which corresponds to more than 400 modes evenly spaced by 127 GHz. The high wavelength side of the frequency comb is capped at 4.3 μm, which is due to the intrinsic loss in the silica cladding and air absorption (primarily due to CO_2). A higher pump power to achieve soliton formation is required, largely due to the slightly lower Q factor at 3.07 μm. Unlike previously measured soliton spectra, we observe a significantly depleted pump mode, which we attribute to operating in the highly overcoupled microresonator. The output comb power excluding the pump mode is 32 mW and comprises 80% of the total output power of 40 mW, which indicates a 40% pump-to-comb efficiency. To our knowledge, it represents the broadest modelocked frequency comb demonstrated in microresonators.

2.4 Modelocking via Electrical Tuning

Using pump laser detuning to achieve, control, and stabilize solitons is limiting since tunable lasers typically suffer from frequency jitter, mode hopping, and limited tuning speed. Therefore, in order to enable an ultralow noise frequency comb with long-term stability, an alternative tuning method combined with a fixed frequency pump laser is beneficial. For example, it will allow for interfacing with quantum cascaded lasers (QCL), which would be a significant step towards fully integrated operation and for achieving comb generation in multiple microresonators with a single pump. Thermal tuning of a cavity resonance with an integrated heater has recently been achieved [100], and Joshi, *et al.* [21] have demonstrated modelocking with this technique. Our approach here is to achieve a modelocked mid-IR frequency comb in silicon by controlling the FC lifetime. This novel approach takes advantage of the negative FCD coefficient and introduces a blue-shifted cavity resonance during comb generation. In our devices, the FC lifetime can be controlled by changing the applied reverse-bias voltage on the PIN junction, which has been previously reported in [96] showing a tuning capability from 3 ns to 12.2 ps for reverse-bias values ranging from 0 to -15 V in a similar PIN junction structure. In addition, since the FC lifetime determines the bandwidth of this tuning method, the tuning speed can be much faster than with thermal tuning.

2.4.1 Numerical Simulation

We use the modified Lugiato-Lefever model using our silicon device parameters to numerically simulate FC lifetime tuning for modelocking. The 3PA coefficient

is 2×10^{-27} m^3/W^2, and FCA cross section and FCD parameter are 5.88×10^{-21} m^2 and 3.75, respectively, as defined in [97]. The range of FC lifetimes used in our model is within the experimental capability based on the range of applicable reverse-bias voltages. In our simulations, since FC's due to 3PA plays a role above a certain intracavity pump power, the frequency combs are first generated via regular linear pump frequency detuning at τ_{fc}=100 ps [Fig. 2.5(i)], which is followed by an increase in FC lifetime to 300 ps while pump detuning is kept fixed [Fig. 2.5(ii)]. This results in a change in pump detuning from effective blue-detuned to red-detuned, along with the evidence of multiple soliton formation. Further increases in FC lifetime from 300 ps to 500 ps, 1 ns and eventually 2 ns reduces the number of solitons in the cavity [Fig. 2.5(iii-v)], and the single soliton state with a smooth optical spectrum is achieved at τ_{fc}=2.5 ns [Fig. 2.5(vi)]. In addition, our simulations indicate that soliton formation can be achieved at larger pump detuning values for τ_{fc}=100 ps, which is equivalent to the conventional method of pump laser detuning and is due to the fact that such electrical tuning introduces an additional nonlinear cavity detuning via FCD. Also, since FCD relies on the 3PA process, it depends on the dynamical behavior of intracavity power and changes the FCA-induced nonlinear cavity loss at the same time.

2.4.2 Experimental Demonstration

We first investigate the transmission across a cavity resonance by scanning the pump laser frequency for different reverse-bias voltages of -35 V, -20 V, -14 V, and -7 V, as shown in Fig. 2.6(a). We see the cavity resonance blue-shifts with decreasing voltage, indicating that we are in the regime where FCD dominates

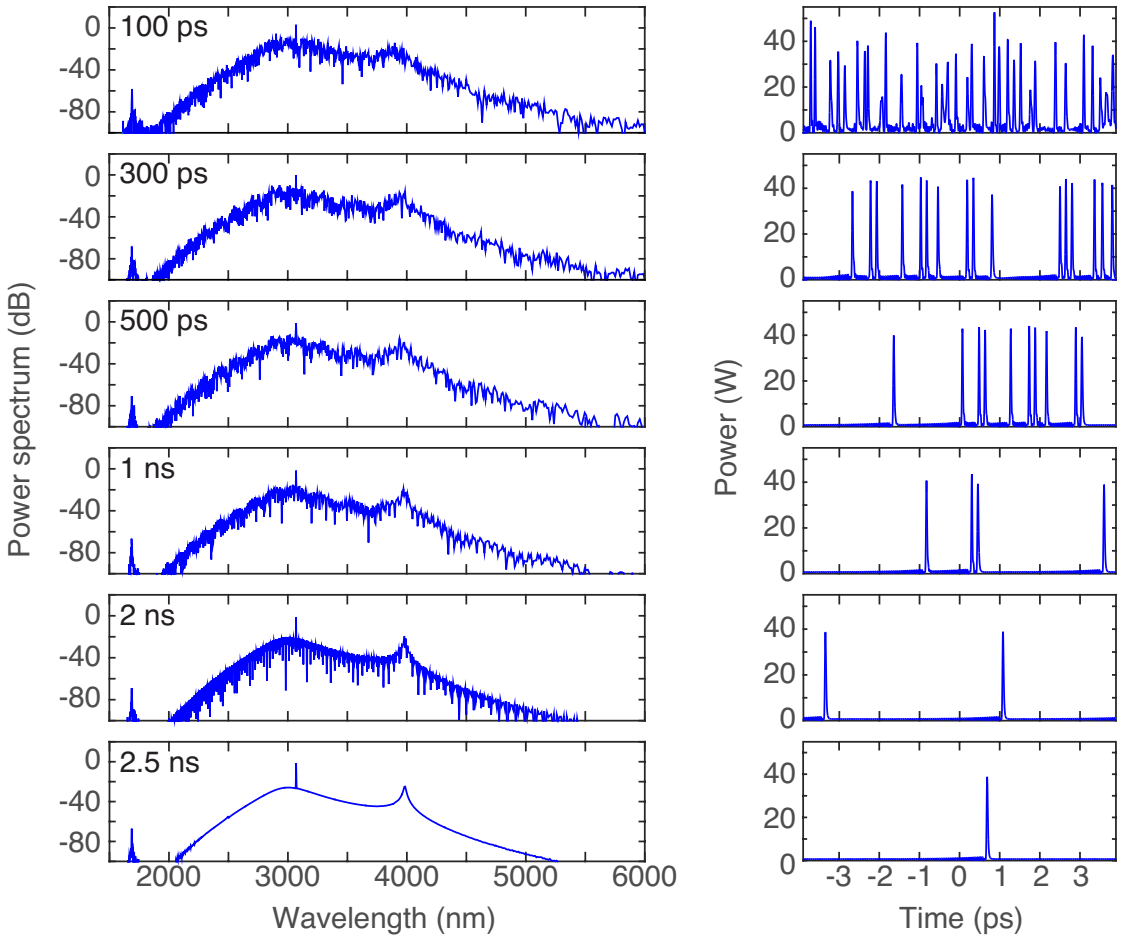

Figure 2.5: Numerical simulations of soliton formation via free-carrier (FC) lifetime tuning in a silicon microresonator. Starting with a high-noise state frequency comb, the evolution of the optical spectra (left) and temporal behavior (right) is shown by increasing the FC lifetime from 100 ps to 2.5 ns. The full time axis represents one round trip of the microresonator.

and that, more importantly, tuning the reverse-bias voltage changes the pump detuning from the cavity resonance. Characteristic soliton steps are observed within this voltage range, but not below -6 V due to increased FCA. To achieve modelocking, we follow the tuning direction, as shown in Fig. 2.6(a), from -20 V to -7 V which corresponds to increasing the FC lifetime. Starting from a high-noise state at -20 V, the frequency comb is modelocked at -7 V, corresponding to

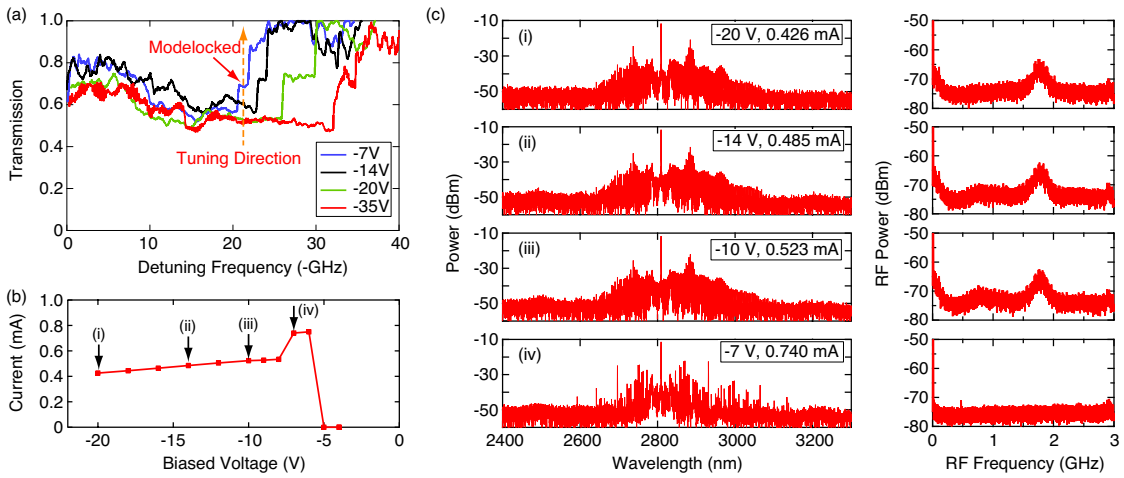

Figure 2.6: Electrical tuning of FC lifetime towards modelocking. (a) Optical transmission while scanning the pump frequency over one cavity resonance at different reverse-bias voltages. Orange arrow indicates the voltage tuning path to achieve soliton modelocking, corresponding to the generation dynamics in (c). (b) 3PA-induced current following the tuning path in (a). (c) Comb generation dynamics via electrical tuning. Right: optical spectrum; left: RF spectrum. (i-iv) correspond to various reverse-bias values indicated in (b).

the position of the soliton step in the transmission. This transition also coincides with an abrupt increase of the 3PA-induced current even at a decreased reverse-bias voltage, which is indicative of intracavity pulse formation [Fig. 2.6(b)]. The corresponding evolution with both optical and RF spectra are recorded in Fig. 2.6(c). The final multi-soliton state occurs with a modulated optical spectrum and low RF amplitude noise. There exists multiple voltage tuning paths to achieve modelocking. For example, seen from Fig. 2.6(a), if the initial reverse-bias voltage is -35 V, the final reverse-bias voltage for modelocking can range from -6 V (the minimum reverse-bias voltage at which modelocking still exists) up to -35 V, depending on the initial pump detuning.

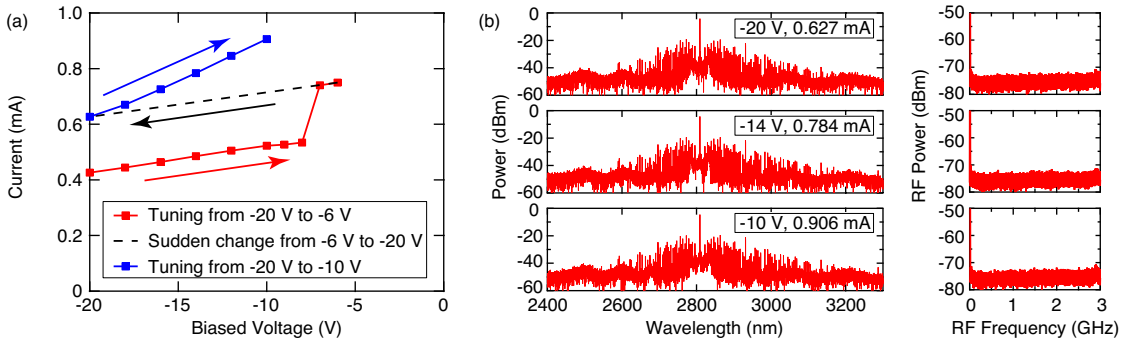

Figure 2.7: Electrical measurement and control of the soliton state. (a) DC component of 3PA-induced current measured with a specific reverse-bias voltage tuning path. (b) Optical spectra and RF noise spectra of the soliton state at three reverse-bias voltages corresponding to the blue arrow in (a).

2.4.3 Stability of Soliton States

Once soliton formation is achieved, we explore the robustness of the soliton state by varying the reverse-bias voltage. Once a particular soliton state is reached, the range over which the reverse-bias voltage can be decreased corresponds to the detuning range of the given soliton step, which, in our case, is from -7 V to -6 V. However, soliton states can be quite robust to increases in the reverse-bias voltage. In our experiment, we abruptly increase the reverse-bias voltage from -6 V to -20 V, and observe that the structured optical spectra, the low noise RF signal, and high DC current are all maintained (Fig. 2.7), indicating that the soliton state is preserved. Increasing the reverse-bias voltage is equivalent to reducing the effective red-detuning of the pump, which corresponds to lower soliton peak powers [16] and causes the 3PA-induced DC current to decrease from 0.74 mA to 0.627 mA. As the reverse-bias voltage is gradually decreased from -20 V to -10 V, we observe an increase in current due to the same reasoning [Fig. 2.7(b)]. More interestingly, we observe a hysteresis effect in the

measured current, indicating that different cavity detunings are possible even for the same reverse-bias voltage. This is due to the strong dependence of FC density on dynamical intracavity power, which also makes it distinct from the thermal tuning technique.

Another feature of electrical tuning is that the DC current is directly linked to the soliton peak power. Since the soliton peak power is determined by the pump cavity detuning and the resonator properties, we can potentially frequency stabilize the pump cavity detuning by stabilizing the DC current to a fixed value using the reverse-bias voltage. The response time of electrical tuning can be very fast due to the short FC lifetime and could be four orders of magnitude smaller than thermal tuning response time in Si_3N_4 [101].

2.5 Summary

In summary, we demonstrate a modelocked silicon microresonator-based frequency comb with near-octave spanning bandwidth and low pump power requirement. We achieve a high pump-to-comb conversion efficiency where the output comb power excluding the pump mode is 40% of the total input pump power in the bus waveguide. Modelocking can be achieved without complex laser tuning techniques to overcome transient thermal instability. The electrical measurement and control of FC's in a silicon chip significantly simplifies the system design for the generation of a highly coherent and stable mid-IR frequency comb. The PIN structure enables monitoring the intracavity dynamics and tuning of the FC lifetime to produce soliton modelocking and to control and stabilize the soliton state with high bandwidth. Our approach removes the

constraints of pump frequency tuning and provides a path towards a fully integrated mid-IR comb source via combining silicon microresonators with mid-IR QCL's and chip scale dual-comb spectroscopy.

CHAPTER 3

BREATHER SOLITON DYNAMICS IN MICRORESONATORS

3.1 Introduction

The generation of temporal cavity solitons in microresonators results in coherent low-noise optical frequency combs which are critical for applications in spectroscopy, astronomy, navigation or telecommunications. Breather solitons also form an important part of many different classes of nonlinear wave systems, manifesting themselves as a localized temporal structure that exhibits oscillatory behavior. To date, the dynamics of breather solitons in microresonators remains largely unexplored, and its experimental characterization is challenging. Here, we demonstrate the excitation of breather solitons in two different microresonator platforms based on silicon nitride and on silicon. We investigate the dependence of the breathing frequency on pump detuning and observe the transition from period-1 to period-2 oscillation. Our study constitutes a significant contribution to understanding the soliton dynamics within the larger context of nonlinear science.

Temporal cavity solitons (CS's) are self-localized pulses of light that can be excited in nonlinear optical resonators [12, 16, 22, 46, 50, 54, 102, 103] and have recently attracted significant research interest in the context of microresonator-based frequency comb generation [3, 4, 12, 13, 16, 19, 20, 22, 23, 46, 81, 103–106]. In contrast, a breather soliton is a nonlinear wave in which energy is localized in space but oscillates in time, or vice versa [51, 55–59, 106], and is found in various subfields of natural science, such as solid-state physics, fluid dynamics, plasma physics, chemistry, molecular biology, and nonlinear optics [107]. Breather soli-

tons have been recently reported in an optical fibre cavity [51].

Here, we present a theoretical and experimental study of breather CS's [51, 55–57] excited in microresonators. This work provides experimental observation and characterization of such dynamic instabilities in optical microresonators [51, 56–59, 106], which constitute a significant contribution toward understanding the universal dynamics of frequency combs based on driven passive resonators and is relevant to a large variety of physical systems for both fundamental and applied interests. We demonstrate the universal nature of such breather solitons in two different material platforms, silicon nitride (Si_3N_4) [13, 20, 81, 104] and silicon (Si) [3, 4]. Our results establish a direct link between the breathing frequency and the pump-cavity detuning which is used to excite temporal CS's in microresonators.

3.2 Numerical simulation of breather solitons

The LLE allows for modeling of rich cavity dynamics, including a variety of instabilities and in particular, predicts the existence of persistent breathing CS's in optical resonators pumped by a continuous-wave (cw) laser [51, 56, 108, 109].

The LLE is expressed as

$$t_R \frac{\partial E(t,\tau)}{\partial t} = \left[-\alpha - i\delta_0 + i\gamma L|E|^2 + iL \sum_{k\geq 2} \frac{\beta_k}{k!} \left(i\frac{\partial}{\partial \tau} \right)^k \right] E(t,\tau) + \sqrt{\theta} E_{in} \qquad (3.1)$$

Here $E(t,\tau)$ is the slowly varying intracavity field envelope, t is the slow evolution time on the order of the cavity roundtrip time t_R, while τ is a fast time related to the group velocity of light inside the resonator. α is a fraction

corresponding to half the total percentage power loss per roundtrip, and L is the cavity length. γ is the nonlinear parameter, and β_k is the kth order dispersion coefficient. Finally, θ is the input coupling coefficient, E_{in} is the pump field strength, and δ_0 is the phase detuning of the pump with respect to the nearest cavity resonance.

To ensure broader applicability of our study, we employ the following dimensionless form of the LLE [50]

$$t_R \frac{\partial F(t,\tau)}{\partial t} = \left[-1 - i\Delta_0 + i|F|^2 + i \sum_{k\geq 2} d_k \left(i \frac{\partial}{\partial \tau} \right)^k \right] F(t,\tau) + S \tag{3.2}$$

Here we have used the normalization convention $t \rightarrow \alpha \frac{t}{t_R}$, $\tau \rightarrow \tau \sqrt{\frac{2\alpha}{|\beta_2| L}}$, $F = E\sqrt{\frac{\gamma L}{\alpha}}$, $S = E_{in}\sqrt{\frac{\gamma L \theta}{\alpha^3}}$, $\Delta = \frac{\delta_0}{\alpha}$, with the additional expression for the normalized dispersion coefficients $d_k = \frac{\beta_k L}{\alpha(k!)} (\frac{2\alpha}{|\beta_2| L})^{k/2}$, such that the 2nd order dispersion coefficient d_2 represents the sign of the group-velocity dispersion (d_2 = -1 in our case). The optical frequency f and RF frequency used in Fig. 1 & 4 correspond to the dimensionless fast time τ and slow time t, respectively, and hence are also dimensionless. Note that S (equivalently, $X = |S|^2$) and Δ are the normalized pump field strength (pump power) and detuning, respectively, and are the only control parameters of the current system under consideration, thus simplifying our investigation. For specificity, however, we use parameters similar to our 200 GHz free-spectral-range (FSR) Si_3N_4 resonator with 950×1500 nm cross-section, i.e. $t_R = \text{FSR}^{-1} = 5$ ps, $\alpha = 0.0018$, $\theta = 0.0005$, $\gamma = 0.9$ $\text{W}^{-1}\text{m}^{-1}$, L = 0.63 mm, β_2 = -202 $\text{ps}^2\text{km}^{-1}$, $\beta_3 = 0.034$ $\text{ps}^3\text{km}^{-1}$, $\beta_4 = 7.7 \times 10^{-4}$ $\text{ps}^4\text{km}^{-1}$, and $|E_{in}|^2$ = 170 mW. Depending on the simulation, we vary δ_0 from -0.00522 rad to 0.0216 rad. These parameters correspond to $|S|^2 = X = 8.7$ and Δ = -2.9 to 12, d_2

= -1, d_3 = 0.003, and d_4 = 9 x 10^{-6}. Although we include higher-order (3rd and 4th) dispersion coefficients for completeness, their effects are negligible and do not invalidate the applicability of the past theoretical studies to our case.

In Fig. 3.1(a) and (b), we simulate the temporal evolution of a breathing CS and its peak power evolution, respectively, in a microresonator using a normalized version of the LLE (for all details on numerical simulation, see Methods). Here we fix the dimensionless pump power X = 8.7 and the cavity detuning Δ = 4.5 and use the approximate analytic solution [54] of a CS as the initial seed. It can be seen in Fig. 3.1(a) that as the CS evolves from bottom to top, it undergoes a periodic oscillation in time, which is accompanied by the associated breathing of the CS spectral envelope with the same period [57]. Furthermore, we present the evolution of the optical spectrum and the cavity transmission in Fig. 3.1(c) and (d), respectively, as Δ is ramped up from -2.9 to 12, this time seeding the simulation with a noise corresponding to one photon per frequency mode. Such a detuning ramp is consistent with the typical experimental technique where the pump laser frequency is tuned across the resonance starting from the effectively blue-detuned regime (with respect to the thermally-shifted hot resonance) [16, 53]. We observe that the intracavity field initially develops into a low-noise primary comb state (State 1), destabilizes to an unstable modulation instability (MI) state (State 2), and eventually settles into the soliton state (State 4). This transition into the soliton state coincides with the pump frequency crossing the effective zero detuning and is accompanied by an abrupt change in the cavity transmission [16] as demonstrated in Fig. 3.1(d). More importantly, the breather soliton state (State 3) is identified by observing a periodic oscillation in time similar to Fig. 3.1(a) and (b), and is located in the region of detunings between the unstable MI state and the stable CS regime, which is

consistent with previous theoretical studies [51, 56–59].

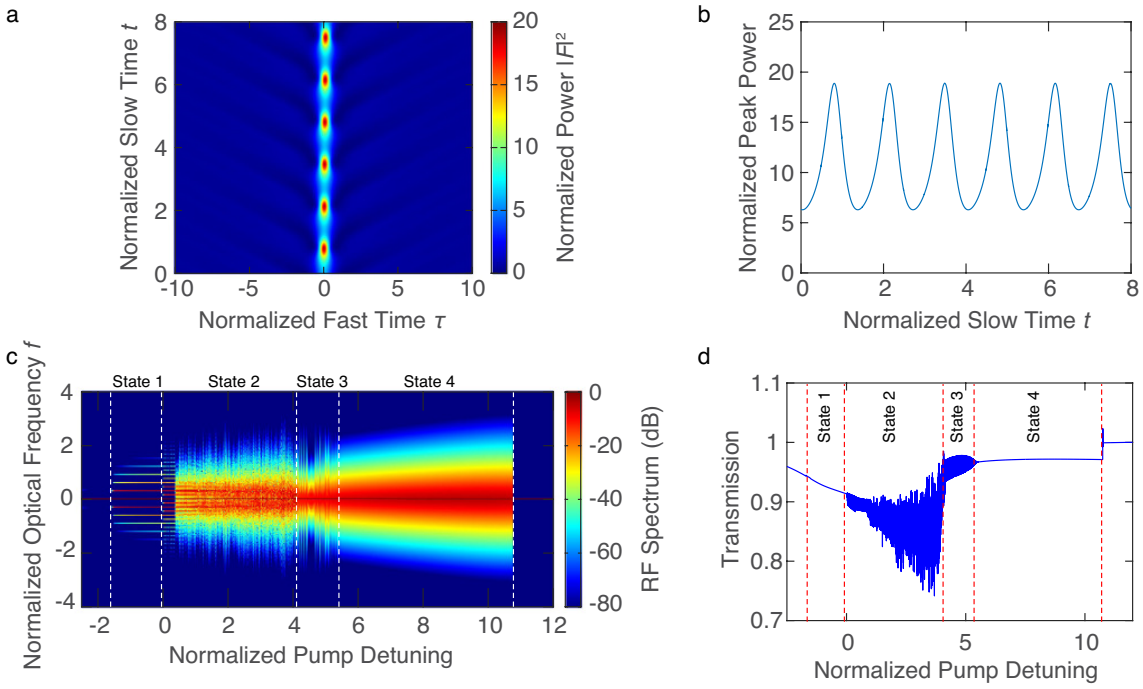

Figure 3.1: Numerical simulation of breather solitons. (a) The temporal evolution of a breathing temporal cavity soliton (CS). The period of the breathing cycle is 1.34 normalized slow time units. (b) The corresponding temporal evolution of the CS peak power. (c) Simulated density plot of instantaneous optical spectra as a function of the normalized absolute pump detuning Δ (from -2.9 to 12) and (d) the corresponding resonator transmission. The vertical dashed lines in (c) and (d) indicate the four different regions which correspond to (i) the primary comb state, (ii) unstable MI state, (iii) breather soliton state, and (iv) stable soliton state. All the values are dimensionless.

3.3 Experimental observation of breather solitonss

In our experiment, we observe breather solitons in Si_3N_4 microresonators in the telecommunication wavelength range and in Si microresonators in the mid-

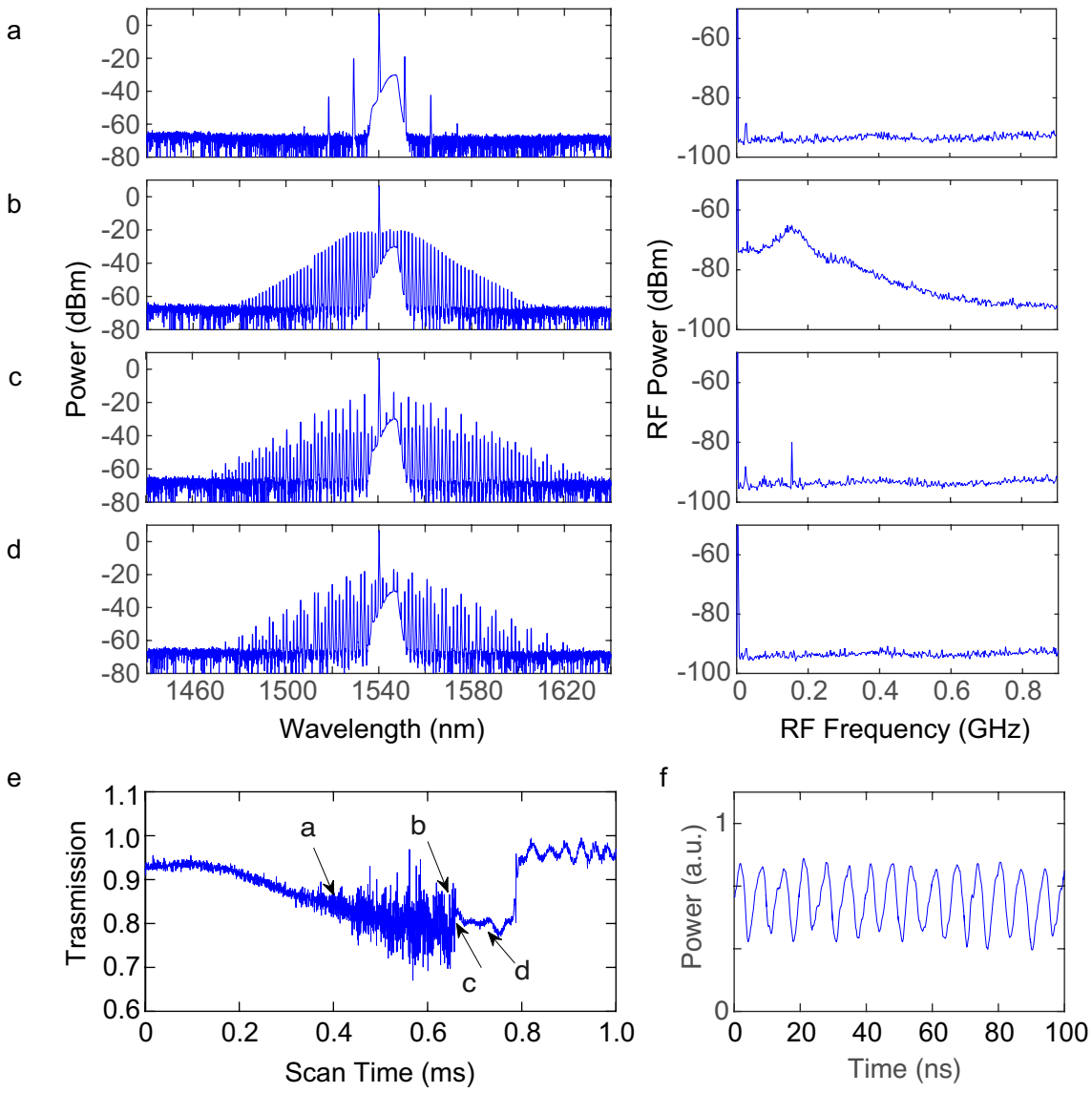

Figure 3.2: Observation of breather solitons in Si_3N_4 microresonators. (a) – (d) Optical and RF spectral evolutions where the state (c) shows breather solitons in Si_3N_4. (e) The pump power transmission as the laser frequency is scanned across the resonance. The scanning window corresponds to an absolute pump detuning range of 17 GHz. The arrows correspond to the four regions (a)–(d). The transmission step is indicative of soliton formation. (f) The recorded time trace of the comb output power at the breather soliton state (c).

infrared (mid-IR) range. In a Si_3N_4 microresonator, the spectral evolution towards soliton formation in both the optical and RF domains is plotted in Fig. 3.2(a-d), as the pump laser is tuned into resonance. These four pairs of plots, from top to bottom, correspond to the generation of primary comb lines, unstable MI state, breather solitons, and stable solitons, as demonstrated numerically in Fig. 3.1. Soliton formation is confirmed by low RF noise [Fig. 3.2(d)] and the abrupt cavity transmission step [Fig. 3.2(c) & (d)] in Fig. 3.2(e). The time evolution of the comb output power for the breather soliton state is recorded in Fig. 3.2(f), which shows the temporal oscillatory behaviour with a time period of 6.3 ns, which corresponds to four times the cavity photon lifetime and the RF beat note of 155 MHz in Fig. 3.2(c). We attribute this sharp RF beat note to the occurrence of breather solitons, as will be further demonstrated in the next Section. Note that while such an RF peak has been observed previously in MgF_2 resonators4 and Si_3N_4 microresonators [13], it was not linked to the presence of breather solitons.

In our Si microresonators, we monitor and analyze different states of the generated frequency combs by measuring the three-photon-absorption- (3PA-) induced photocurrent extracted from the integrated PIN junction, which is an effective way to probe the temporal behavior inside a cavity [4]. Figures 3.3(a)-(d) show the evolution of the generated optical and RF spectra as the pump laser is tuned into resonance in the same direction as in Si_3N_4 microresonators. Initially, from Fig. 3.3(a) to Fig. 3.3(b), the DC component of the 3PA-induced current gradually increases due to intracavity power build-up. These spectra correspond to the unstable MI regime in which multiple independent mini-combs grow from the primary sidebands and spectrally overlap with each other leading to strong and broad RF beat notes [81]. Next, we observe a transition to

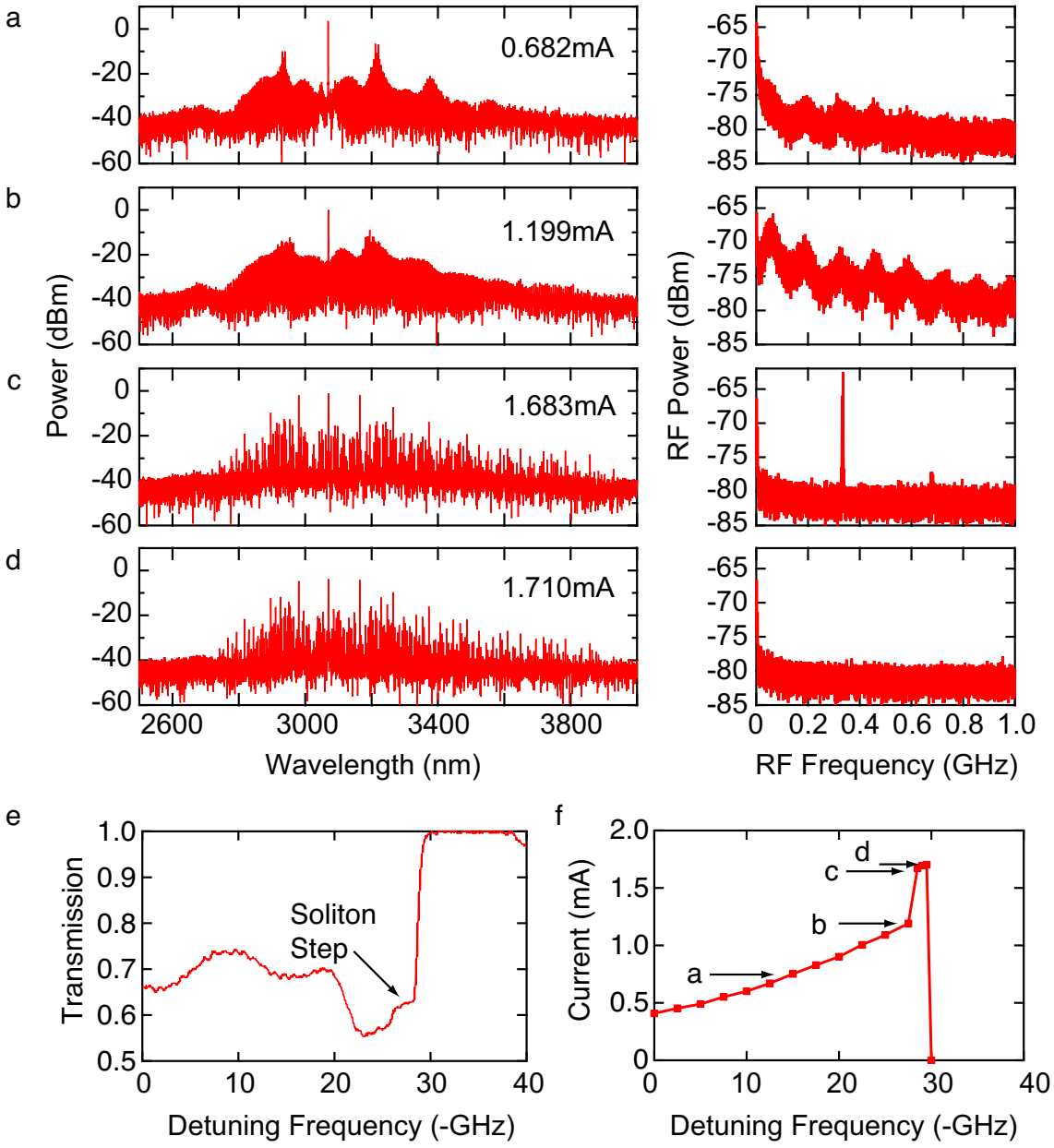

Figure 3.3: Observation of breather solitons in Si microresonators. (a) – (d) Optical and RF spectral evolution where the state (c) shows breather solitons in Si. Optical spectrum in (d) spans 0.8 of an octave (from 2.4 to 4.3 μm). No other significant features are observed in the RF spectra beyond 1 GHz up to 12 GHz. (e) The pump power transmission in Si as the laser frequency is scanned across the resonance. (f) Three-photon-absorption-induced current measured by scanning the pump detuning. Arrows correspond to four states (a) to (d), which are (a, b) unstable modulation instability states, (c) breather soliton and (d) stable soliton states.

a state [Fig. 3.3(c)] with a more structured optical spectrum and an abrupt increase in the measured DC current from 1.199 mA to 1.683 mA. The corresponding RF spectrum shows a sharp peak at 336 MHz with a low noise background. Tuning the pump frequency further leads to a low-noise RF spectrum without any peaks [Fig. 3.3(d)]. The variation in the DC current with pump detuning is shown in Fig. 3.3(f). The sudden increase in the DC current from Fig. 3.3(b) to Fig. 3.3(c) indicates the formation of solitons with a high peak power. We further confirm this by observing the concurrence between the abrupt current increase and a cavity transmission step [12, 16] in Fig. 3.3(e). Thus, the state with the observed sharp RF peak [Fig. 3.3(c)] corresponds to a breather soliton state that exists beyond the unstable MI state but before the stable soliton state, which is consistent with our Si_3N_4 results, and agrees with our simulations and past theoretical studies [51, 56]. Here, the soliton breathes at a rate of 336 MHz, which corresponds to a period of 372 cavity roundtrips and 10 times the cavity photon lifetime. The narrow-linewidth RF beat note corresponding to the breather soliton state can be distinguished from the sharp RF beat notes observed at the onset of the unstable MI state [81] since each one occurs at a different stage of comb evolution. The two states have drastically different temporal behavior (*e.g.* temporally localized pulse formation in the breather soliton state but not in the unstable MI state), which is easily detected by our technique here by measuring the 3PA-induced photocurrent.

The excitation of breather solitons in both platforms requires a certain range of pump power. For example, we observe an evolution towards a stable soliton state without a breather soliton state at a relatively low pump power and more complex dynamics at a higher pump power. In addition, it can be achieved by tuning the pump frequency into resonance without changing the pump power

[109].

3.4 Characterization of breather soliton dynamics

Another important aspect of breather soliton dynamics is that during the transition into the breather soliton state, the broad RF beat note corresponding to the unstable MI state becomes significantly narrower while maintaining the same centre frequency, as shown in Fig. 3.2(b) & (c). Such evolution is also observed in some Si microresonators for which the higher order harmonics of the 3PA-induced current noise do not obscure this feature. This sudden narrowing of the RF beat note is also well predicted by our numerical simulations of the RF spectra of the comb transmission at different comb states corresponding to Fig. 3.1(c) and (d). Our modeling indicates that the breathing CS manifests itself through low-frequency (relative to the comb spacing) modulation sidebands in the RF domain [106], as shown in Fig. 3.4 (green curve) at the pump detuning corresponding to State 3 in Fig. 3.1(c). In addition, the simulated RF spectra at two other pump detunings [State 2 & 4 in Fig. 3.1(c)] are plotted in Fig. 4 for comparison. It can be seen that at the detuning Δ = 3.9, [State 2; blue curve] the system is initially in an unstable MI state characterized by a broad primary noise peak. In the time and spectral domains, the intracavity field fluctuates significantly from one roundtrip to another, analogous to spatiotemporal chaos originally discussed in the context of plasma physics [108]. In contrast, as the detuning is increased past a threshold value, the RF noise peak abruptly sharpens while maintaining its central frequency [State 3: Δ = 4.5; green curve]. Note that the simulated breathing period is 2.7 times the cavity photon lifetime. For comparison, on the same plot, we also show the loaded Lorentzian resonance

curve of the resonator under consideration on the same axes (right axis; red curve). The sharpening of the RF beat note can be mathematically explained as follows. Just before the system crosses the boundary from the unstable MI regime to the breather state, the eigenmode associated with the breather state corresponds to the complex eigenvalue with the largest positive real part (i.e. the most unstable). As the system enters the breather state, this eigenmode dominates the cavity dynamics while other unstable modes become stable and dampen out over time. As a result, the beat note frequencies of the two distinct states are expected to coincide. The sideband eventually drops to a negligible level with an increased detuning [State 4: $\Delta = 8$; black curve] which signifies the stabilization of the temporal CS, where the pulse reaches a time-stationary state.

Next, we investigate the factors which influence the breathing frequency. We find that the breathing frequency can be continuously tuned by changing the effective pump-cavity laser detuning. By tuning the pump to shorter wavelength while the soliton state is maintained, the effective pump detuning decreases, and we observe a linear increase in oscillation frequency as well as a decrease in modulation depth in both platforms. In other words, the breathing frequency decreases linearly with an increasing effective pump-cavity detuning as shown in Fig. 3.5 for Si microresonators. For comparison, we run a series of numerical simulations based on the normalized LLE and present the detuning dependence of the breathing frequency for 3 different pump power levels: just above the breather threshold, slightly below the period-2 oscillation threshold, and within the period-2 oscillation regime. For each pump power, we start from the lower detuning boundary of the breather regime, seed the simulation with an approximate analytic solution2 of the stable temporal cavity soliton (CS) and numerically propagate the intracavity field over 10 normalized time units (20

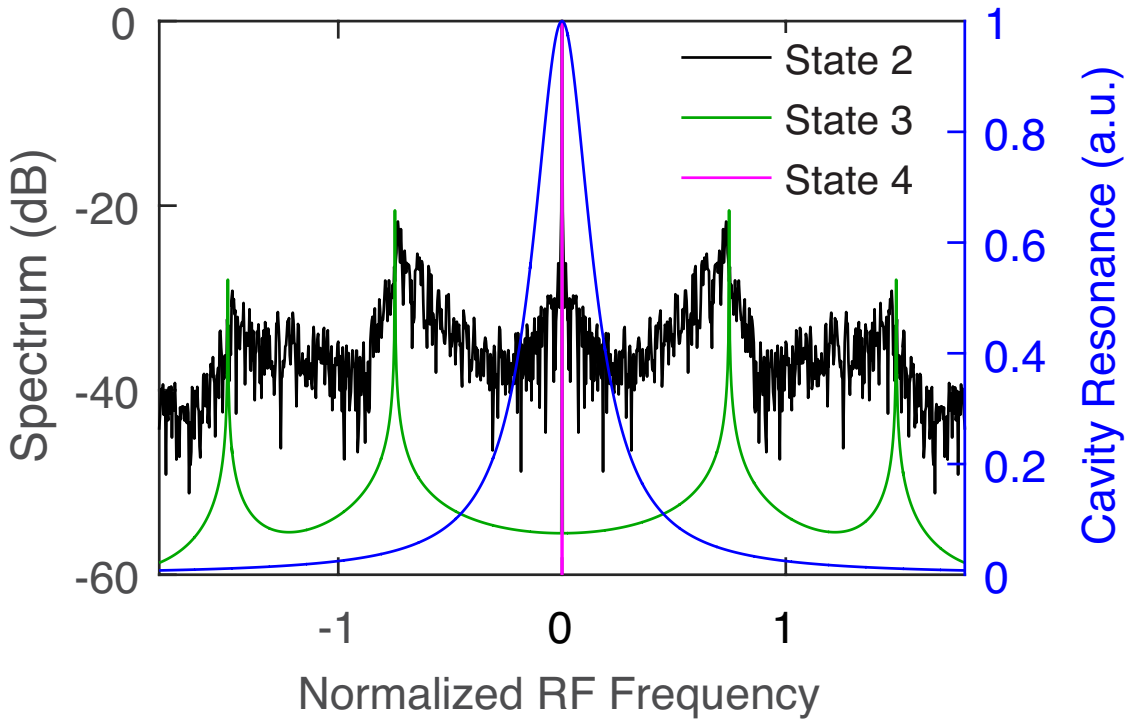

Figure 3.4: Numerical simulations of RF spectra at selected detunings corresponding to Fig. 1(c). Specific detuning values are $\Delta = 3.9$ (State 2), $\Delta = 4.5$ (State 3), and $\Delta = 8$ (State 4). For comparison, the plot also shows the loaded Lorentzian resonance curve (red curve; right axis). Note that the RF frequency corresponds to the normalized slow time in Fig. 3.1(a) and (b) and is dimensionless.

cavity photon lifetimes). Then we regularly sample the roundtrip-averaged intracavity power over the subsequent 190 time units (380 cavity photon lifetimes) in order to obtain the RF spectrum. The breather frequency can be extracted from the resulting RF spectrum. We repeat this process for each detuning as the detuning is slowly ramped up with a step size of 0.2.

The results are summarized in Fig. 3.6. Overall, as consistent with the past theoretical studies, the breather regime shifts to higher detunings with an increasing pump power. Several other trends can also be seen. As the detuning

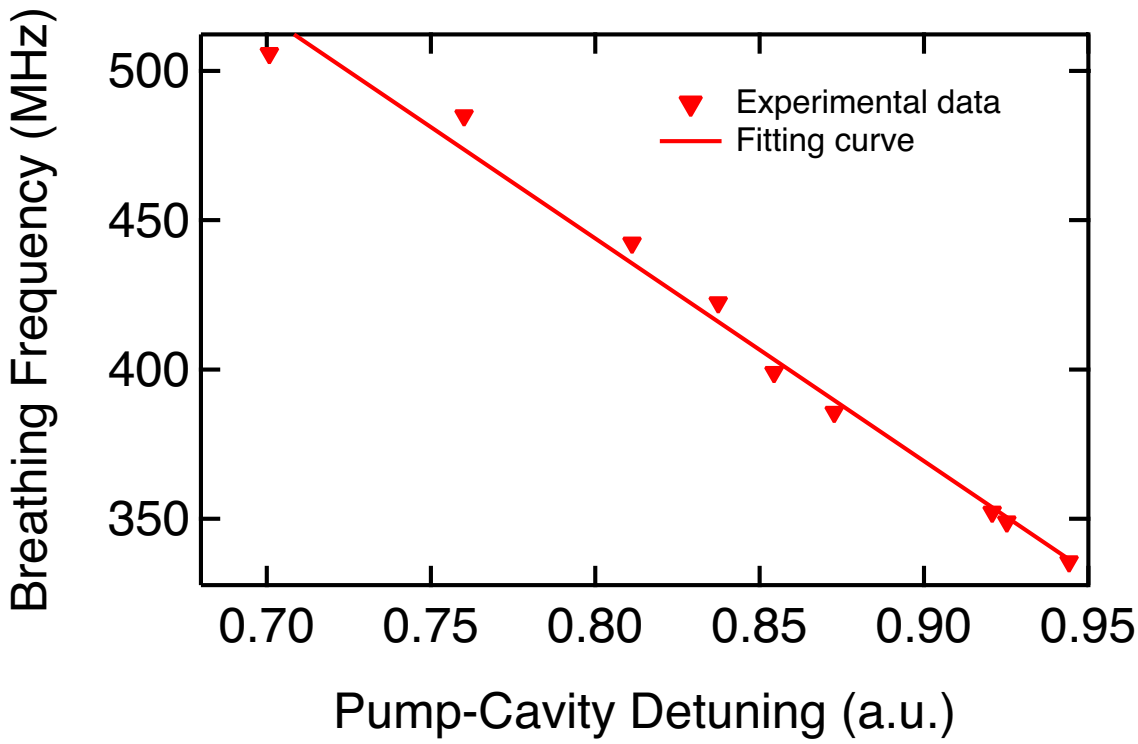

Figure 3.5: The breathing frequency dependence on the effective pump-cavity detuning in the Si microresonator. The effective pump-cavity detuning is extracted from the three-photon-absorption-induced photocurrent based on the relationship with the soliton peak power and thus in arbitrary unit (*a.u.*). The same trend is also observed in a Si_3N_4 microresonator.

increases, the breathing frequency initially does not change significantly (low power; green triangles), or even decrease linearly (higher powers; red squares and blue circles). Toward the higher detuning, the trend reverses and can be approximated by a straight line with a positive slope for each power. Our experiments are conducted by tuning the pump frequency in the increasing direction of Δ across the transition point from the unstable modulation instability to the breather states, and agree qualitatively with the trend observed at the lower detuning range. However, the positive linear trend toward the higher detuning range has not been observed in our experiment despite the fact that it occurs

over a larger detuning range. This may hint that we are operating at relatively high pump powers. In addition, our numerical simulations reveal that in the higher detuning range, a linear increase in the breathing frequency is expected with increasing detuning. However, this trend is not currently observed in our experiments and is under further investigation.

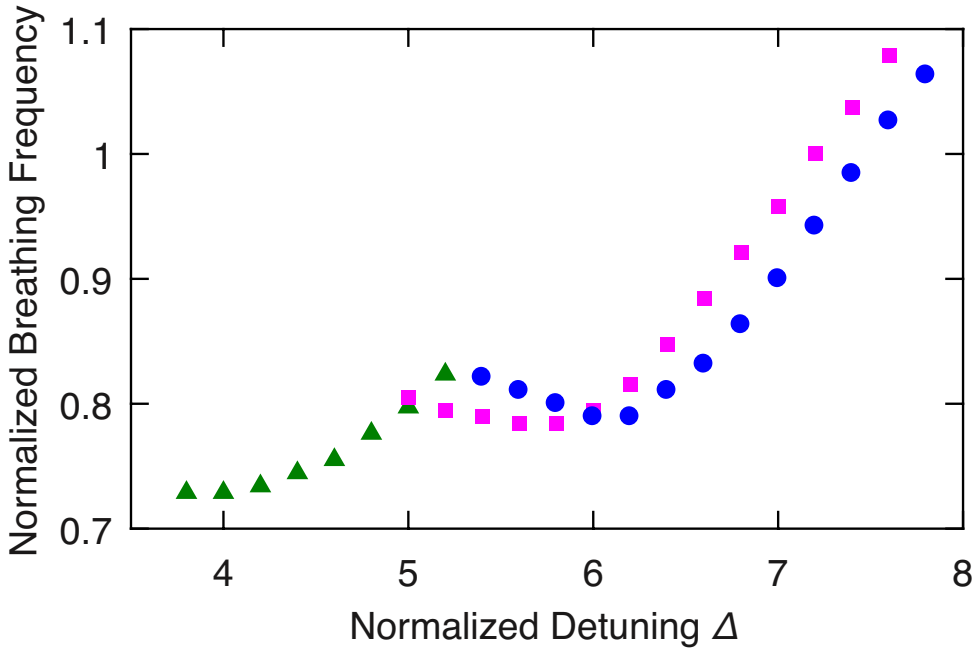

Figure 3.6: Simulation of the breathing frequency as a function of the normalized detuning (Δ) for 3 different pump power levels: just above the breather threshold (green triangles), slightly below the period-2 oscillation threshold (red squares), and within the period-2 oscillation regime (blue circles). Breathing frequency is normalized with respect to 0.5 * photon lifetime^{-1}. Detuning is normalized with respect to the cavity roundtrip loss.

Microresonators allow access to larger detuning values in the cw regime (cf. quasi-cw synchronous pumping [109]) due to their high finesse. At higher values of the detuning and pump power, more complicated dynamical regimes can be found in the LLE, such as period-2 oscillations, period-N oscillations, and temporal chaos [51, 109]. In the Si_3N_4 microresonator, using a higher pump

power than that in Fig. 3.2, we observe a transition from the period-1 oscillation to the period-2 oscillation [Fig. 3.7(a) –(b)], and the field finally stabilizes into stable CS's [Fig. 3.7(c)] as the pump detuning is increased. Unlike the theoretical prediction of Ref. [51], we do not observe the system returning to the period-1 breather state beyond the period-2 regime. A possible explanation is that the thermal effect acts as an additional source of instability that hinders our observation of the expected behaviour, especially across the boundaries of different regimes. Nevertheless, this is the first time an oscillatory temporal CS with higher periodicity has been observed experimentally.

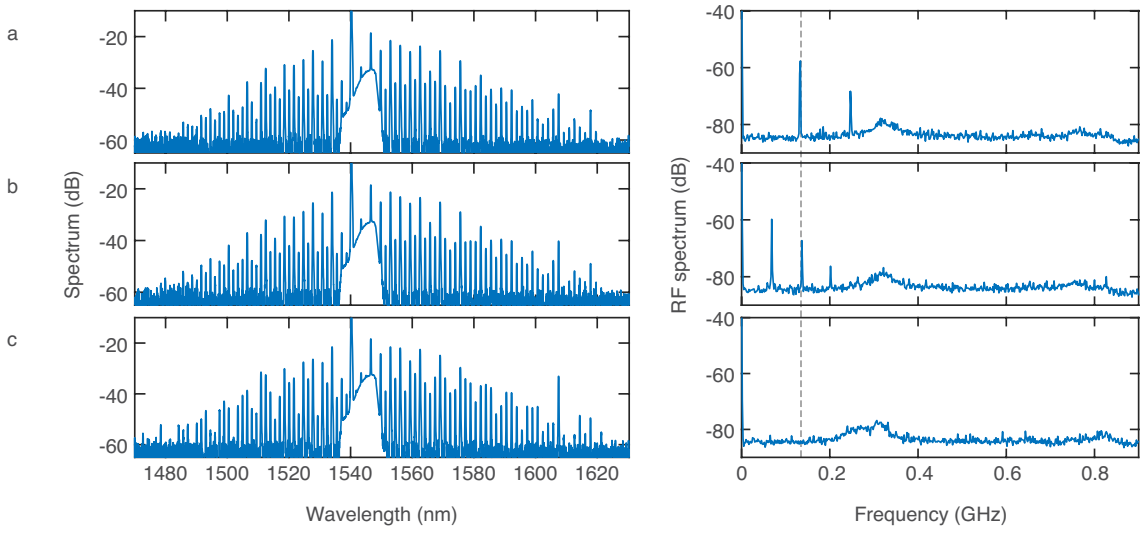

Figure 3.7: Temporal cavity soliton of higher oscillatory periodicity in a Si_3N_4 microresonator. At a higher pump power, as the pump detuning increases, the period-1 oscillation (a) transitions to a period-2 oscillation (b), and the cavity soliton finally stabilizes (c). The dashed line indicates that the first RF beat note in state (a) aligns with the second RF beat note in state (b) at the transition point.

3.5 Conclusions

We show the universality of the dynamics of the breather CS formation in microresonators, attributing the formation of narrow low-frequency RF modulation sidebands in the modelocked CS regime to time-oscillating behaviour of CS's. The universal nature of breather soliton formation is indicated by our observation in two distinct platforms that have different material characteristics, device geometries and operating conditions. Our results present experimental confirmation of the pioneering theoretical studies of a breather soliton solution in a cw-pumped high-finesse microresonator and provide experimental techniques for their observation, which agrees well with our numerical results. Our work also indicates that the breathing frequency is dependent on the pump-cavity conditions, and reveals that microresonators can be an ideal test bed for fundamental theories of nonlinear wave dynamics that are relevant to a large variety of physical systems.

CHAPTER 4

MID-INFRARED DUAL-COMB SPECTROSCOPY

4.1 Introduction

Dual-comb spectroscopy (DCS) [35,37,66,78,86,88,93,110–122] is a non-intrusive absorption spectroscopy technique that measures the time-domain interference between two frequency combs of slightly different line spacing. This allows the absorption spectrum to be converted from the optical to the radio-frequency (RF) domain which can be detected rapidly using a single detector. This is particularly critical in the mid-infrared (mid-IR) domain in which sensitive, fast detector arrays remain elusive. The potential of DCS is clear for gas-phase studies in the near-infrared spectral region where DCS shows higher measurement speed, resolution and accuracy than state-of-the-art Michelson-based Fourier transform spectrometers [78]. In recent years, microresonator-based frequency combs have emerged as an attractive compact and broadband source emitting equidistant phase-coherent lines with a large line spacing using a single continuous-wave (CW) pump laser [3, 4, 9, 16, 20, 21, 31, 32, 35, 37, 79]. Microresonator-comb systems could be attractive for spectroscopy in the mid-IR, where sources remain under development [66, 93, 110, 111, 114, 115, 117, 118, 121, 122]. In the mid-IR region, the absorption strengths of molecular transitions are typically 10 to 1,000 times greater than those in the visible or near-IR, offering the potential to identify the presence of substances with extremely high sensitivity and selectivity. As pointed out by Ideguchi, T. *et al.* [112], frequency combs of large line spacing (about 100 GHz) and very broad span (approaching an octave or even broader) are required for efficient dual-comb spectroscopy

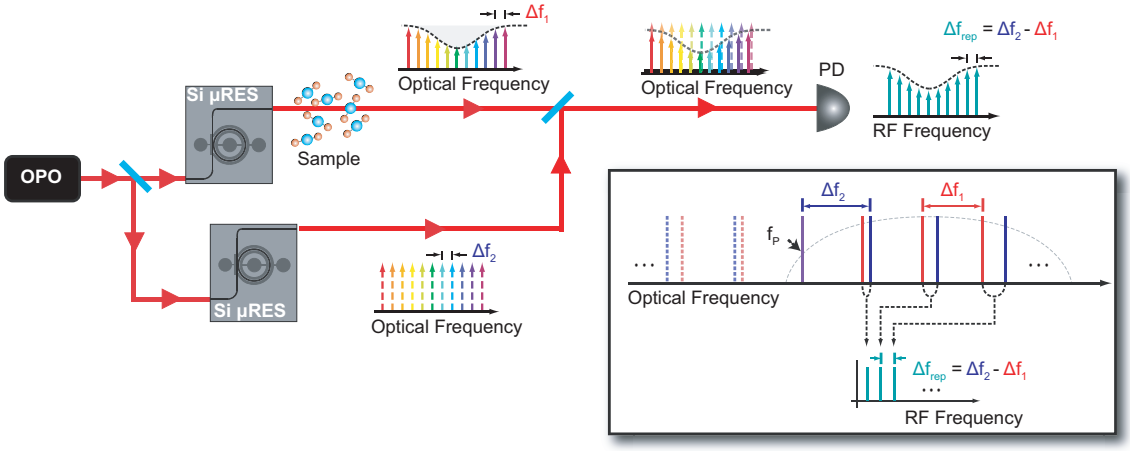

Figure 4.1: Schematic for dual-comb absorption spectroscopy. Experimental setup for our dual-comb source. A continuous-wave optical parametric oscillator pumps two separate silicon microresonators, which generate two modelocked combs. The output is combined and sent to a photodiode for RF characterization. Inset: Schematic for single-pump operation and mapping from optical to RF domain. Δf_1 and Δf_2 are the repetition frequencies of two optical frequency combs. $\Delta f_{rep} = \Delta f_2 - \Delta f_1$ is the difference in repetition frequencies. PD, photodiode; Si µRES, silicon microresonator; OPO, optical parametric oscillator.

in the liquid or solid-state phases. As such, microresonator-combs represent unique tools for exploring the potential of new approaches to vibrational spectroscopy, in applications where traditional combs based *e.g.* on modelocked laser systems are not suited. Recently, Suh, *et al.* [35], demonstrated a dual-comb in the telecommunication region covering 60-nm (6-THz) bandwidth in silica whispering-gallery devices. However, the silica platform cannot be translated into the mid-IR due to inherently high material losses, and the system relies on the use of two separate pump lasers.

In this work, we present a CMOS-compatible silicon-based, chip-scale mid-IR dual-comb spectrometer that meets the requirements for vibrational DCS and mid-IR molecular fingerprinting in the condensed phase. Two mutually coher-

ent modelocked frequency combs are generated using a single CW laser spanning from 2.6 μm to 4.1 μm. Thermal control and free-carrier injection allow for independent modelocking of each comb and for tuning of the dual-comb parameters. The large line spacing of the combs (127 GHz) and its precise tuning over tens of MHz, which are unique features of chip-scale comb generators, are exploited for a proof-of-principle experiment of vibrational absorption DCS of acetone. This work represents a critical advance for chip-based linear DCS for liquid/condensed matter phase studies, which would find a wide range of applications in chemistry, bio-medicine, material science, and industrial process control. With further development, it holds promise for real-time and time-resolved spectral acquisition on nanosecond time scales.

4.2 Results

4.2.1 Generation of the dual-comb source

The experimental setup is shown in Fig. 4.1. We use two silicon microresonators that have 100-μm radii and are dispersion engineered to have anomalous group-velocity dispersion beyond 3 μm for the fundamental TE mode, similar to Griffith, *et al*. [4]. A CW optical parametric oscillator (100-kHz linewidth) emitting at 3 μm simultaneously pumps two microresonators with slightly different line spacings. The two generated combs are combined at a beamsplitter and sent to a photodetector (bandwidth of 250 MHz) connected to an RF spectrum analyzer. Integrated PIN diodes, located around the resonators, are operated at a reverse-bias voltage of -15 V to sweep out the free carriers (FC) generated from

three-photon absorption (3PA) [3]. We generate a modelocked mid-IR frequency comb in both microresonators simultaneously by tuning the pump laser into the cavity resonances. A thermoelectric cooler (TEC) is used to control the temperature of each silicon device independently in order to compensate the initial frequency difference between the two pump resonances, and for coarse tuning of the difference in repetition frequencies between the two combs Δf_{rep} to lie within our detector bandwidth. Future implementations could allow for fully integrated microheaters [21], which would achieve even more precise control of the line spacing of each of the microresonators while drawing little power. The mutual coherence between the two combs is established by sharing the same pump laser and from the inherent modelocking mechanism of microresonator-based combs. The RF beatnotes of the dual-comb output appear at frequencies $f_N = N * \Delta f_{rep}$, where N is an integer. Figure 4.1 (inset) shows the mapping of the optical spectrum to the RF dual-comb spectrum where the shorter and longer wavelength sides of the pump are mapped to the same RF domain, which means appropriate long-pass/short-pass filters are needed to access either side of the optical spectrum relative to the pump frequency. Shifting the pump frequency of one of the microresonators, *e.g.*, with an acousto-optic modulator, would avoid such aliasing, as already demonstrated with electro-optic-modulator-based dual-comb spectroscopy [116, 119–121].

Figure 4.2a shows the generated spectrum of one of the combs measured by a Michelson-based Fourier transform infrared spectrometer (M-FT). The spectrum consists of 305 comb lines with a spacing f_{rep} = 127 GHz and spans 2.6 – 4.1 μm, which is the region of the fundamental CH, NH and OH stretching modes in molecules. The pump powers for each microresonator are 80 and 50 mW, and the pump-to-comb conversion efficiencies are each > 30 %. The power

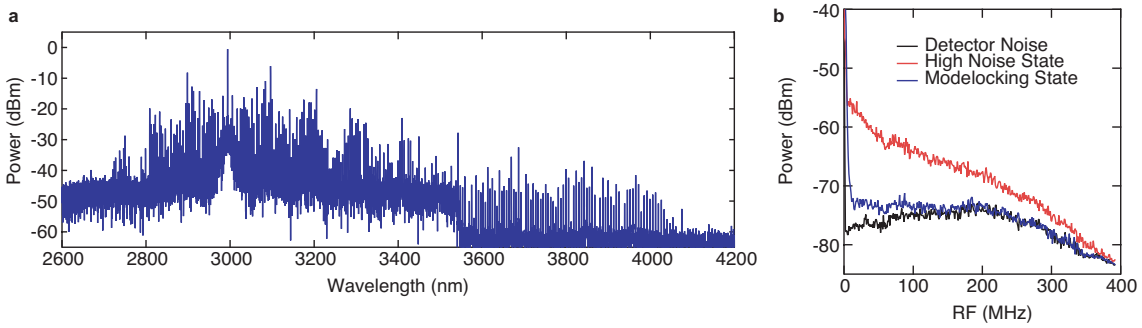

Figure 4.2: Silicon microresonator-based dual-comb source. (a) A spectrum of one of the generated combs measured using a Michelson-based Fourier transform infrared spectrometer (M-FT). The spectral range is from 2.6 μm to 4.1 μm. The resolution is 7 GHz (0.25 cm^{-1}). (b) RF-noise characterization of the generated comb. The plot shows the reduction in RF amplitude noise corresponding to modelocking.

of each comb line varies from 2.5 μW to 2 mW in the range of 2.8 – 3.2 μm and the power variation is due to the modulation in the optical spectrum from multiple solitons generated within one cavity roundtrip [21,32]. Since the cavity linewidth (105 Q-factor) is broader than the detector bandwidth, the sharp comb linewidth when in the modelocked state is crucial for resolving the RF beatnotes of the two combs. The transition to the modelocked state is determined by the observation of a step in the optical transmission [16], an abrupt increase in the 3PA-induced FC current [32], and the transition to a low RF noise state as shown in Fig. 4.2b [20].

While the M-FT spectra of the two individual and combined modelocked frequency combs are shown in Fig. 4.3a, the RF dual-comb spectrum is plotted in Fig. **??**b where the intensity profile agrees well with the product of the amplitudes of the electric fields of two optical frequency combs within the detection range. The achieved difference between the line spacings Δf_{rep} is 12.8 MHz, corresponding to a frequency compression factor from the optical to RF domain of

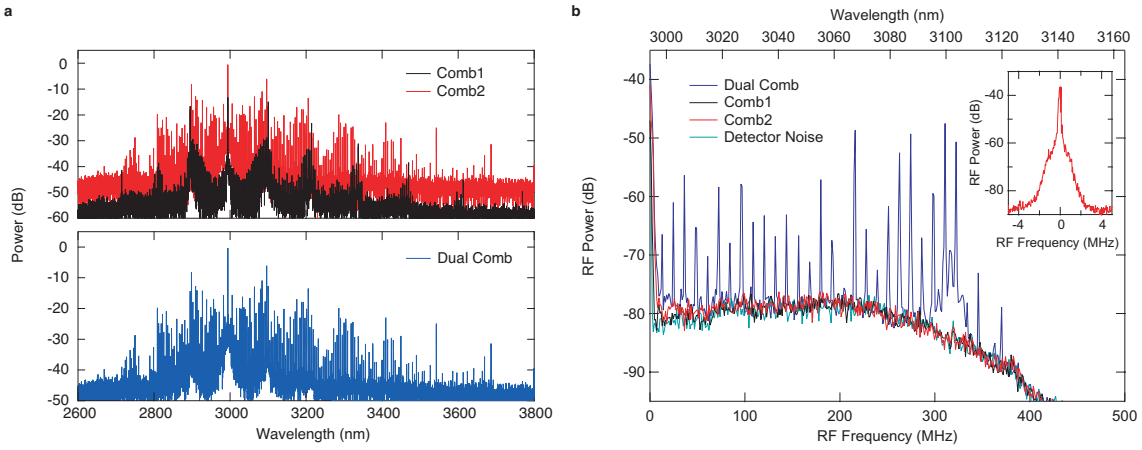

Figure 4.3: Characterization of dual-comb source. (a) Top: M-FT spectra for each modelocked comb. Bottom: Combined M-FT spectrum. (b) RF spectrum from the dual-comb interferometer. Plot shows RF spectra for dual-comb (blue), each separate modelocked comb (black and red), and detector noise background (dark cyan). Inset: Characterization of the 25th RF beatnote in (b).

$f_{rep}/\Delta f_{rep}$ (~10,000). The minimum time required to resolve the RF comb lines is $1/\Delta f_{rep}$ (~78 ns), indicating the potential for a rapid single-shot measurement. The measured linewidth of the 25th RF comb line [Fig. 4.3b inset] is < 100 kHz at a RF resolution bandwidth of 40 kHz, which corresponds to a mutual coherence time between the two combs of >10 μs. The frequency jittering of the optical frequency combs is dominated by the pump laser [21]. Therefore, the coherence between the two generated combs is drastically improved because the effect of the pump noise is expected to be significantly minimized by sharing the same pump with the two microresonators.

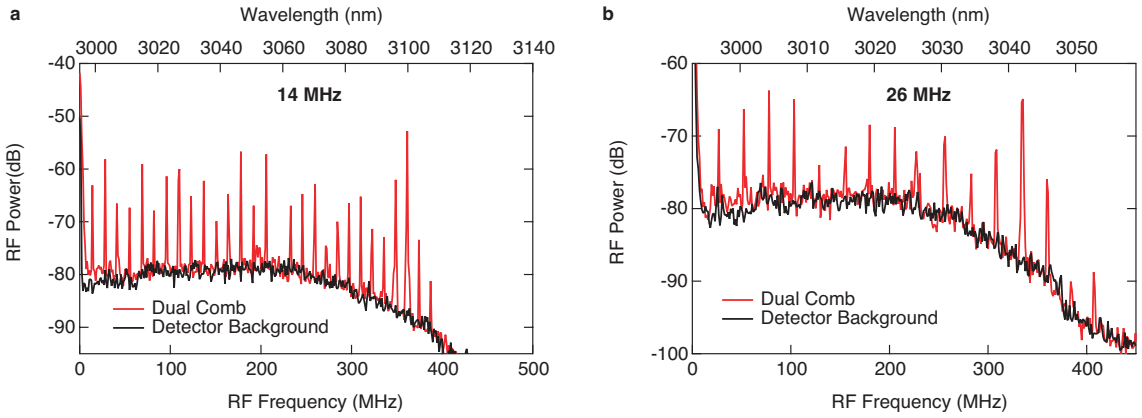

Figure 4.4: Repetition rate tuning of the dual-comb source. The frequency spacing of the dual-comb source is dictated by the spacing of each of the modelocked combs. The plot shows a 14 MHz spacing (left) and a 26 MHz spacing. The spacing is tuned by adjusting the TECs to change the resonance position of the microresonators.

4.2.2 Tunability of the dual-comb source

While the spectral window of 2.6 – 4.1 μm (73 – 115 THz) can be mapped into an RF window of 2.5 GHz with Δf_{rep} = 12.8 MHz, our measurement spectral range is currently 3 - 3.12 μm, which is largely limited by our detector bandwidth of 250 MHz. Our detection range can be extended to cover the entire spectral window by using a faster detector or by controlling the repetition rate of the two combs to achieve a smaller Δf_{rep} (*e.g.*, 1 MHz). Coarse tuning of the Δf_{rep} can be achieved by thermally tuning the resonances of one microresonator by one or more (free spectral ranges (FSR's). In our case, we found that the Δf_{rep} is changed by ~ 126 MHz by moving to the next resonance in one of the microresonators, which is about 1/1000 of the FSR. Additionally, we achieve fine tuning of the repetition rate of our dual-comb system (Δf_{rep}) shown in Fig. 4.4. We observe that Δf_{rep} can be finely tuned by >10 MHz by simply changing the pump-cavity detuning while maintaining modelocking in both microres-

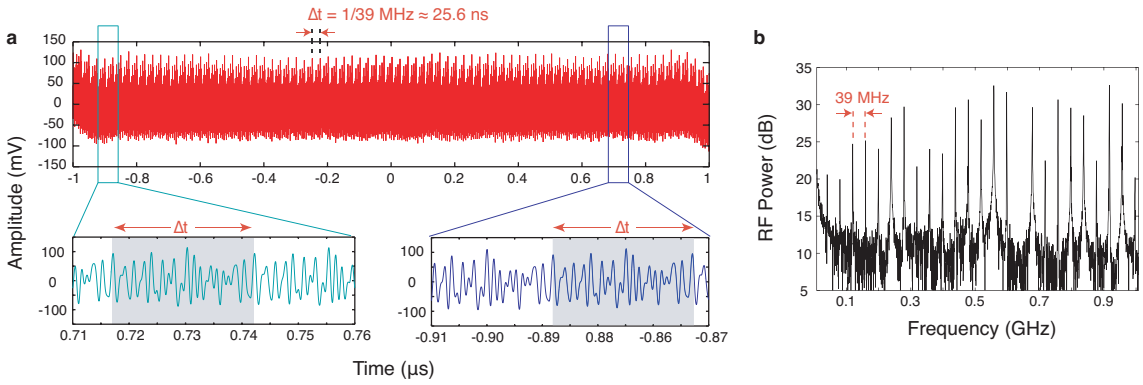

Figure 4.5: Experimental interferogram and spectrum. (a) Time-domain interferogram over a measurement time of 2 μs. The waveform repeats with a period of 25.6 ns, which is the inverse of the difference in comb line spacing (39 MHz). The waveform of one period is shaded and demonstrates good reproducibility. The multiple bursts within one period indicate that multiple solitons are generated in each microresonator within one cavity roundtrip. (b) Fourier-transformed spectrum of the time-domain interferogram in (a), on a logarithmic scale with 24 resolved lines and an average signal-to-noise ratio of 13.8 dB (≈ 24). Modulation in the spectrum is also due to both comb operating in multiple soliton regime. The missing RF beat note at 0.64 GHz is due to the absence of a comb line, which is attributed to a mode crossing effect within the microresonator.

onators. Moreover, Δf_{rep} is dependent on both the FC dispersion effect and on the thermo-optic effect. By individually controlling the reverse-bias-voltage applied on the PIN junctions, the line spacings of the microresonators can be finely controlled independently such that smaller Δf_{rep} (~ 1 MHz) can be achieved in the near future. This tuning technique of the RF line spacing (Δf_{rep}) provides flexibility in achieving an optimal refresh rate of the measurement over a desirable spectral range and in further compressing the needed RF window.

4.2.3 Time-domain interferogram

For our spectroscopy experiments, the spectra are obtained by taking the Fourier transform of the time-domain interference signal, which is measured using a photodetector and a fast real-time oscilloscope with a sampling rate of 80 Gbps. The difference in the line spacing between the two 127-GHz combs is tuned to be 39 MHz. A time-domain interferogram with a measurement time of 2 μs is shown in Fig. 4.5a which displays a periodic waveform that repeats every 25.6 ns, which corresponds to the inverse of the difference in RF comb line spacing. The waveform shows good reproducibility and has multiple peaks within one period due to the interference of multiple solitons generated in both microresonators within a cavity roundtrip. The Fourier-transform of the interferogram reveals a RF spectrum (Fig. 4.5b) where 24 comb lines are resolved with a line spacing of 39 MHz. The observed comb linewidth is 0.5 MHz, limited by the recording time of 2 μs. We define the signal-to-noise ratio (SNR) based on the intensity of the comb line divided by the standard deviation of the noise baseline between two comb lines. We observe an RF beat note at 0.64 GHz with a SNR lower than the noise floor due to the absence of an optical comb line, which is attributed to mode-crossing effects in the microresonator. This point is excluded for our calculation. The average SNR is about 24, and the variation of the SNR over the comb teeth is due to multiple soliton formation. The average SNR per unit of time exceeds 1.6×10^4 $s^{-1/2}$, and its product with the number of spectral elements exceeds 10^6 $s^{-1/2}$, which is comparable to the previously reported value of 10^6 $s^{-1/2}$ for a mid-IR dual comb measurement [111].

4.2.4 Proof-of-principle spectroscopy measurement

We illustrate the potential of our dual-comb spectrometer for broadband vibrational spectroscopy of liquid samples with a proof-of-principle absorption measurement. We insert a 100-μm thick cuvette filled with neat acetone in the combined arm of the dual-comb interferometer. The sample of acetone is chosen due to its absorption feature centered around 2925 nm. Here, we utilize two different bandpass filters to access each side of the optical spectrum with respect to the pump wavelength. The absorption spectra for each side of the pump are measured with an acquisition time of 2 μs using two faster photodetectors of 1-GHz bandwidth, corresponding to a spectral window of 2900 – 3100 nm. The dual-comb absorbance and transmittance spectra are shown in Fig. 4.6 at a spectral resolution of 127-GHz (4.2-cm^{-1}) resolution, which is extracted from fitting the M-FT data. The transmittance is calculated as the ratio between the spectrum with and without the cuvette using balanced detection. The absorbance is the logarithm of the transmittance. We compare the results to the absorption spectrum we measured using a Fourier transform spectrometer (Bruker Vertex 70) equipped with a globar, a CaF_2 beam-splitter and a InSb detector. The instrumental resolution is 0.5 cm^{-1} (16 GHz), which is much narrower than the spectral bands of the liquid molecular sample. The two spectra are in reasonable agreement. However, we observe a large deviation in our absorption measurement close to the pump (shaded region in Fig. 4.6a), which could be due to low SNR of corresponding beat notes and imperfect spectral response of the bandpass filters. The standard deviation of the measured transmittance is 4.1% as shown in Fig. 4.6b, which is primarily limited by the average SNR in the dual-comb spectrum. The short temporal separation between individual solitons in a multiple soliton state could also contribute to deviations in the absorption mea-

surement due to the free induction time of the molecules. Additional deviations may arise from the cross-talk of the two bandpass filters and averaging over multiple acquisitions can reduce the root-mean-square deviation but at a cost of a longer acquisition time.

4.3 Discussion

Our dual-comb spectrometer using silicon-microresonator-based frequency combs will readily achieve spans from 2600 to 4100 nm by reduction of the difference in repetition frequencies. A difference Δf_{rep} = 3.3 MHz would map the 305 comb lines within the 1-GHz bandwidth of our fastest detector. Spectra of 42-THz bandwidth at 127-GHz resolution will then be acquired at a refresh time of 0.3 μs. For comparison, the fastest M-FT interferometer [123] measures interferograms at a resolution of 270 GHz (9 cm^{-1}) with a refresh rate of 80 kHz (refresh time: 13 μs). Moreover, our refresh rate is fundamentally limited by the Nyquist limit to 200 MHz. As losses in the silicon nanowaveguides continue to decrease, we expect that microresonators with smaller FSR's will be achievable which will allow for higher spectral resolution. Real-time averaging with field-programmable gate arrays may boost the sensitivity to weak absorptions of trace molecules. With future developments to our CMOS-compatible platform, such as implementation of quantum cascade lasers as pump sources, broader spans and access to other ranges of the molecular fingerprint region can also be envisioned. With continued progress to instrumentation such as mid-IR detectors and digitizers, we believe this system will evolve into a spectroscopy laboratory on a chip for real-time vibrational sensing on the nanosecond time scale.

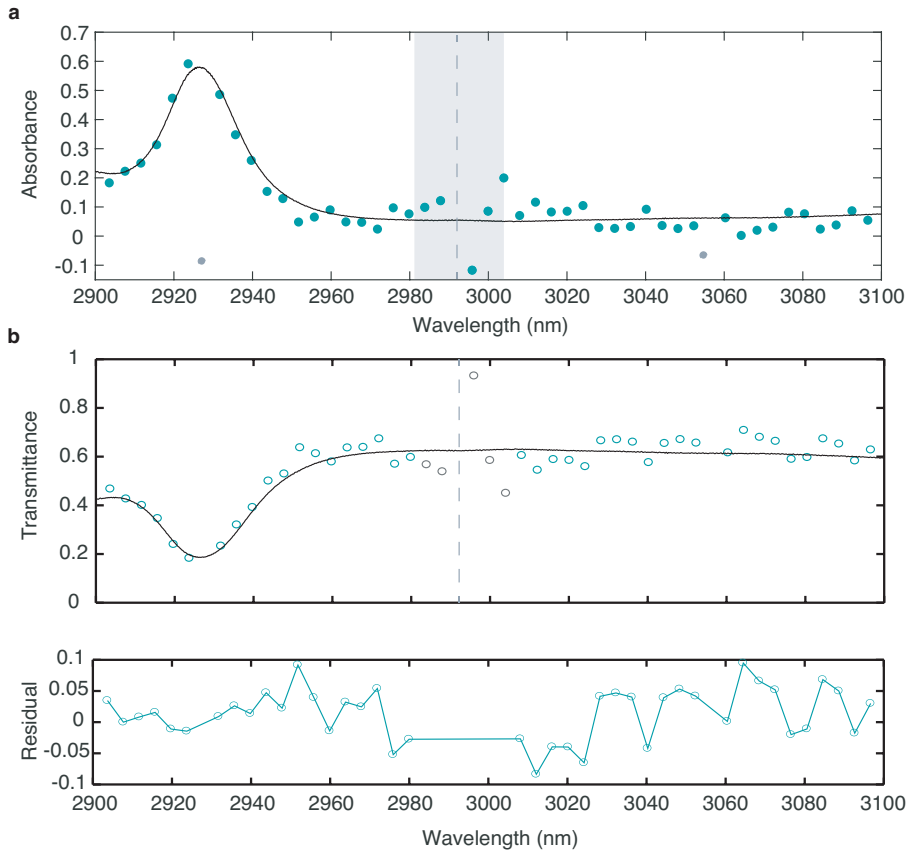

Figure 4.6: Absorption spectroscopy over a short measurement time. Two different bandpass filters are used to access the two sides of the dual-comb spectrum that are symmetric with respect to the pump wavelength of 2992 nm. The measurement time is 2 µs for each side of the dual-comb spectrum. The transmittance is calculated as the ratio between the spectrum with the cuvette and the spectrum without the cuvette. (a) The absorbance is the logarithm of the transmittance. The results are compared to the absorption measurement using a M-FT spectrometer equipped with a globar. The shaded region near the pump frequency (dashed line) shows large variations, which we attribute to the low SNR of the corresponding RF beat notes (< 10 dB) and the imperfect spectral response of the two bandpass filters. Two points (grey) at 2927 and 3055 nm are due to missing RF beat notes shown in Fig. 4.5b and therefore not plotted in the transmittance curve (b). (b) Transmittance and its residual. Five points in grey are not used for the residual. The standard deviation of the residual is 4.1%, which is largely limited by the averaged SNR of 24 in the dual-comb spectrum.

CHAPTER 5

HIGH-RESOLUTION GAS-PHASE SPECTROSCOPY

5.1 Introduction

Mid-infrared (Mid-IR) frequency combs [86] can enable broadband gas-phase spectroscopy [77, 124] with unprecedented measurement capabilities and new applications in medical diagnostics, astrochemistry, atmospheric monitoring, remote sensing and industrial process control. Compared to tunable lasers, such broadband combs enable an accurate measurement of a large number of molecular absorption lines and species simultaneously in a complex environment [125]. The most widely used OFC is generated by a modelocked femtosecond laser [10, 126] and has been previously utilized for high-resolution spectroscopy [127, 128]. In order to resolve narrow absorption features, spectrometers with high instrumental resolution are often required to resolve individual comb lines of a low repetition rate OFC. Comb-resolved molecular spectroscopy has been achieved using modelocked lasers in dual-comb systems [111,121,129,130], high-resolution Fourier transform spectrometers (FTIR) [131], VIPA-based spectrographs [128], Venier spectroscopy [132–134] and fiber comb spectrometers [135]. Tuning the frequencies of the OFC and interleaving the spectra has been first demonstrated to further improve the spectral resolution by [136] and then applied to Doppler-free Fourier transform spectroscopy [137]. The possibility of surpassing the resolution of FTIR and VIPA technique has been demonstrated by scanning the repetition rate of the OFC [128, 131, 138]. In the mid-IR, where laser sources and high quality photodetectors (or arrays) remain in development, significant challenges exist for developing newer mid-IR

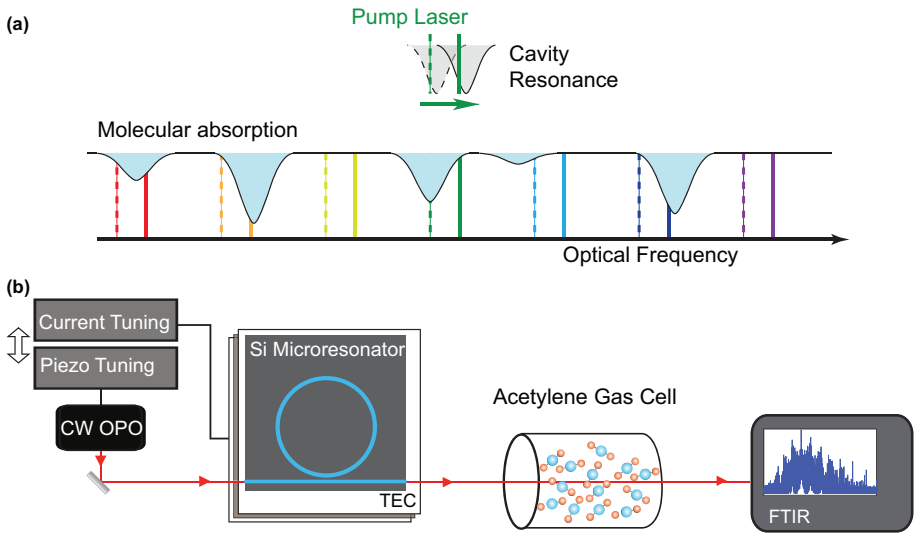

Figure 5.1: (a) Scheme for scanning comb spectroscopy. (b) Experimental setup for microresonator-based scanning comb spectroscopy. CW OPO: continuous-wave optical parametric oscillator, FTIR: Fourier transform infrared spectrometer.

OFC-based spectrometers with higher sensitivity and higher resolution in more compact systems.

Recently, mid-IR OFC's using quantum cascade lasers (QCL) [115, 139] and microresonators [34] have shown great promise as a new generation of highly compact spectrometers. Over the past decade, microresonator-based OFC's [3, 13, 17, 18, 21, 24, 31, 32, 34, 35, 37, 82, 100, 140] have attracted tremendous interests since the platform enables highly compact devices and powerful dispersion engineering which allows for broad optical bandwidths with moderate pump consumption [14]. Several demonstrations of direct-comb spectroscopy have been reported in the near-IR in silica [35], silicon nitride [36, 37] and fluoride microresonators [31] and recently achieved in the mid-IR region using silicon microresonators [3]. However, OFC's in such miniature devices inherently have large repetition rates typically from 10 to 1000 GHz, which precludes their use for high-spectral-resolution molecular spectroscopy.

Here we report the first demonstration of a microresonator-based scanning OFC spectrometer suitable for gas-phase spectroscopy. We demonstrate mode-hop-free tuning of the frequency of a modelocked mid-IR frequency comb in a silicon microreresonator over 0.53 cm^{-1} (16 GHz) via simultaneous tuning of temperature and pump laser frequency. The modelocked comb spans 2520 – 4125 cm^{-1} (2.425 – 3.970 μm) with a comb line spacing of 4.23 cm^{-1} (127 GHz). The absorption spectrum of acetylene in the gas phase is measured in the υ_3 and $\upsilon_2 + (\upsilon_4 + \upsilon_5)^0_+$ bands at a frequency sampling step of 80 MHz despite using a low-resolution FTIR (15 GHz). This technique overcomes the resolution limitation induced by the ultra-small physical size of the integrated device and the instrumental lineshape of the FTIR.

5.2 Experimental results

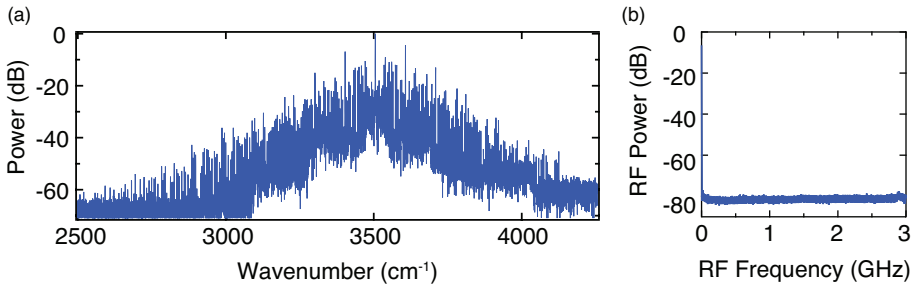

Figure 5.2: (a) The optical spectrum of a modelocked mid-IR frequency comb in a silicon microresonator. The full spectrum is collected using multiple bandpass filters before the FTIR. The modulated spectrum is indicative of a multiple-soliton state. (b) The radio-frequency spectrum of the extracted free-carrier current indicates generation of a low-noise frequency comb.

Our approach is shown schematically in Fig. 5.1a. In a microresonator, the pump line is one mode of the OFC and has a fixed phase relationship with the

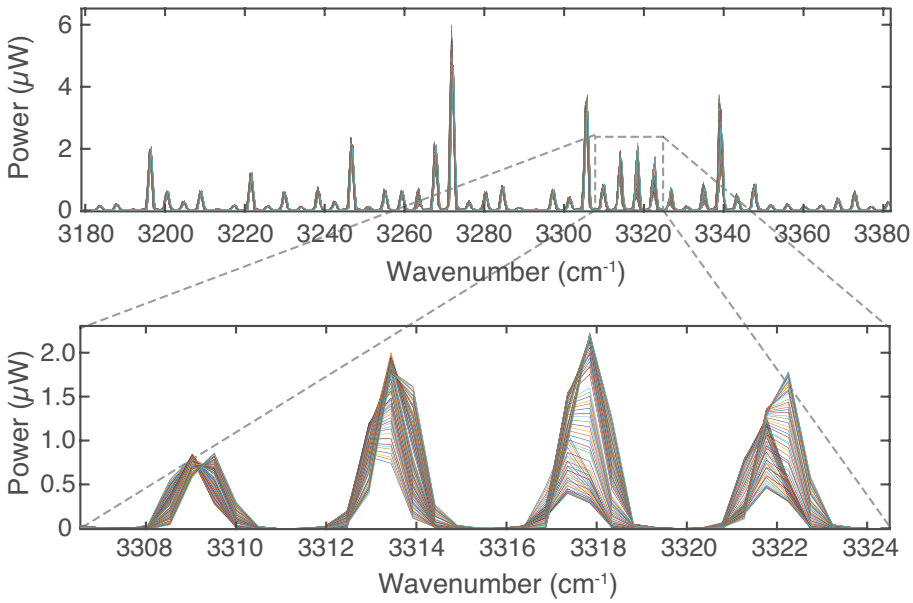

Figure 5.3: FTIR spectra of acetylene absorption measurement. The OFC spectra is recorded at each 80 MHz of the pump shift with a low resolution of 15 GHz in the acetylene fingerprinting region (zoom-in: from 3185 to 3378 cm^{-1}). The variation of the comb line power is largely attributed to the multiple soliton generation within the microresonator. The total measurement time is about 3 mins. Bottom: The zoom-in plot shows the 2^{nd}, 3^{rd}, and 4^{th} comb lines that overlap with the absorption features of the R(13), R(15) and R(17) lines of the $\upsilon_2 + (\upsilon_4 + \upsilon_5)^0_+$ band, respectively.

rest of the generated comb lines. By joint frequency tuning of both the pump laser and its corresponding cavity resonance by one comb line spacing, the OFC can be scanned to cover any spectral point within the comb bandwidth without any gaps. In our case, the pump laser frequency is tuned via piezo control and the cavity resonance is controlled via the thermo-optic effect [13, 17, 18, 21, 100]. The setup is shown in Fig. 5.1b. A high-Q silicon microresonator with a 100-μm radius is dispersion engineered to have anomalous group-velocity dispersion beyond 3 μm for the fundamental TE mode, similar to Yu, *et al.* [32]. The microresonator is pumped by a free-running continuous-wave (CW) OPO at 3508

cm^{-1} (2.850 μm) (Argos Model 2400, <100-kHz linewidth at an integration time of 30 ms). The free carriers (FC) generated from three-photon absorption (3PA) are extracted with an integrated PIN junction and used to monitor the intracavity dynamics [32]. A thermoelectric cooler (TEC) is used to control the temperature of the silicon device with an estimated thermal response time of <0.1s. The output spectrum is measured using a commercial FTIR. As the CW pump laser is swept across the effective zero pump-cavity detuning, soliton modelocking is achieved as indicated by observation of the soliton steps [16], which results in an OFC with narrow lines and low noise. In our experiment, a modelocked mid-IR OFC is generated at a pump power of 45 mW, and the spectrum consists of 378 comb lines with a line spacing f_r = 4.23 cm^{-1} and spanning 2520 – 4125 cm^{-1} as shown in Fig. 5.2. The DC component of the 3PA-induced-FC current is used to monitor the intracavity power and is especially sensitive to the soliton peak power and soliton numbers [32]. At the transition to modelocking, we observed a FC current jump from 0.8 mA to 1.2 mA indicative of soliton formation. We then manually tune simultaneously both the pump frequency and the TEC current, which tunes the cavity resonance. During the tuning process, the DC component of the FC current is kept at 1.245 mA ± 0.001 mA in order to maintain the modelocked state with the same soliton number and peak power. In our case, a multiple-soliton state is generated which results in the variation of the power of the comb lines. The mode-hop-free tuning range of the frequency of the OFC is 0.53 cm^{-1} which is 12.5% of f_r. It corresponds to a 100-mA change in the TEC current, which is about a temperature change of 25 °C . Ideally, a tuning range of one free-spectral-range (FSR) will enable continuous coverage over the entire spectral range. Currently, our tuning range is limited by the pump power variations over the larger bandwidth.

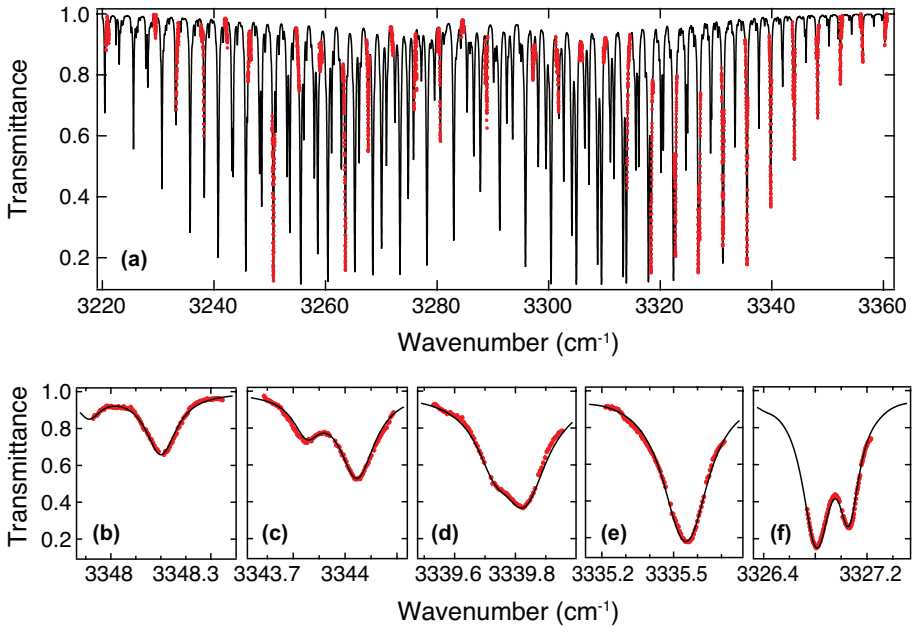

Figure 5.4: (a) Measured transmittance spectrum (red circles) of the υ_3 and $\upsilon_2 + (\upsilon_4 + \upsilon_5)^0_+$ bands of acetylene is shown and compared to the computed transmittance profile (solid black line) using the HITRAN database. The transmittance is calculated as the ratio of the spectral powers with and without the gas cell. Transmittance (zoom-in) of five measured absorption features that correspond to (b) the R(23) line of the υ_3 band, (c) the R(27) line of the $\upsilon_2 + (\upsilon_4 + \upsilon_5)^0_+$ band (left) and the R(21) line of the υ_3 band (right), (d) the R(25) line of the $\upsilon_2 + (\upsilon_4 + \upsilon_5)^0_+$ band (left) and the R(19) line of the υ_3 band (right), (e) the R(17) line of the υ_3 band and the R(23) line of the $\upsilon_2 + (\upsilon_4 + \upsilon_5)^0_+$ band, (f) the R(13) line of the υ_3 band (left) and the R(19) line of the $\upsilon_2 + (\upsilon_4 + \upsilon_5)^0_+$ band (right).

We apply the scanning comb for an absorption measurement of the υ_3 and $\upsilon_2 + (\upsilon_4 + \upsilon_5)^0_+$ bands of acetylene in the gas-phase. The output is recorded with an FTIR after a 2-cm-long single-pass cell, which is filled with 40 Torr of acetylene and 415 Torr of nitrogen. Using this method, scanning OFC spectroscopy can break the resolution limitation of the microresonator-based comb line spacing. The instrumental line-shape of the FTIR is negligible due to a large comb line spacing. In our case, the FTIR is operated with a low resolution of 15 GHz,

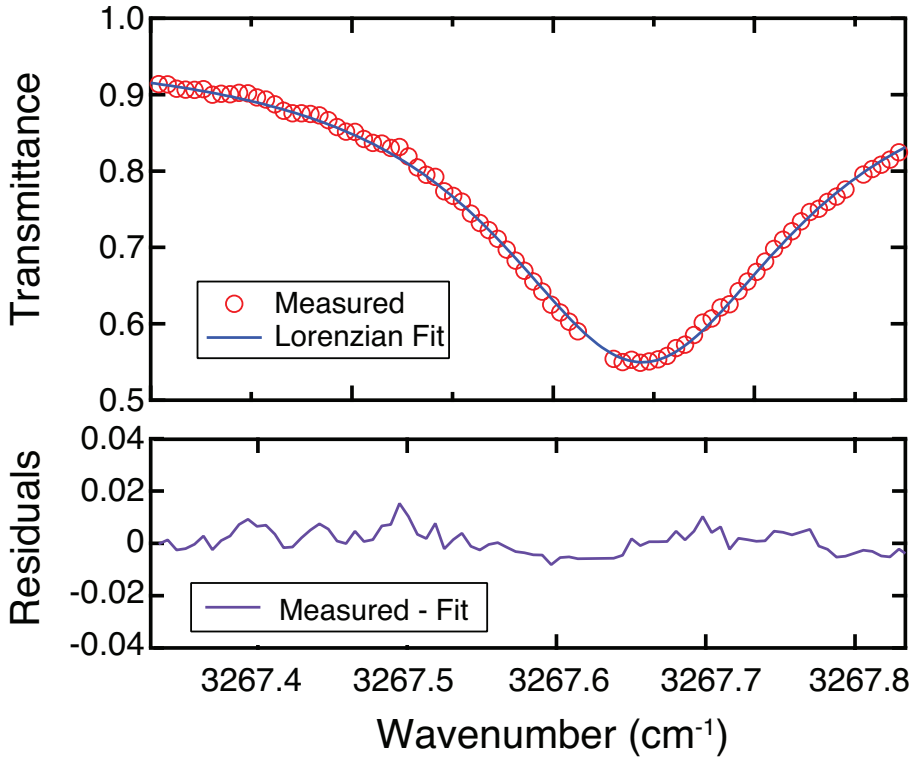

Figure 5.5: A Lorentzian profile (blue) fits the experimental measurement (red dots) of the P(6) line of the $\upsilon_2 + (\upsilon_4 + \upsilon_5)^0_+$ band. A full-width at half maximum of 0.21 cm^{-1} is measured centered at 3267.65 cm^{-1}. The standard deviation of the residuals (purple) is 4×10^{-3}.

which enables fast acquisition. By monitoring the beat-note between the pump laser and a femtosecond laser (Oria^{TM} IR OPO), the pump frequency is tuned at 80-MHz steps. Figure 5.3a shows the recorded FTIR spectra. A bandpass filter with a center frequency of 3077 cm^{-1} (3.250 μm) and a bandwidth of 470 cm^{-1} (0.5 μm) is used before the FTIR. The spectra of selected four comb lines are shown in Fig. 5.3b. The measurement time of each spectrum is approximately 1 second, and the total measurement time is roughly 3 minutes. The frequency accuracy of the measurement is limited by the long-term stability of the pump laser, which is estimated to be < 2 MHz over 1 second and < 10 MHz over 3 minutes. Since the comb spacing is dependent on the chip temperature, the fre-

quency shift of the pump mode is slightly different from that of the rest of the comb lines. Assuming the pump frequency $f_p = f_{ceo} + mf_r$, the index change as the pump is tuned by δf_p is $\delta n = -\frac{m*c}{L(f_p)^2} * \delta f_p$ where c and L are the speed of light in vacuum and the cavity length, respectively. The change in the repetition rate can be expressed as $\delta f_r = -\frac{L(f_r)^2}{c} * \delta n = m\frac{f_r}{f_p}^2 * \delta f_p$; thus, $\delta f_r = \delta f_p/m$. For the comb line ($n = N$), $\delta f_{n=N} = (1 + \frac{N}{m})\delta f_p$, where the pump mode correspond to $n = 0$ and the higher frequency comb mode has $n > 0$. In our case, $m = 825$ and f_r changes from 127.23 GHz to 127.25 GHz over the 16-GHz tuning range of the pump. Each comb line undergoes a different frequency shift, which equals to the product of its scaling factor and the pump shift. It must be taken into account for the frequency calibration through the scanning process. Figure 5.4 shows the calculated transmittance of acetylene in the υ_3 and $\upsilon_2 + (\upsilon_4 + \upsilon_5)^0_+$ bands. Figure 5.4b shows that our transmittance measurement successfully captures different absorption lineshapes. The transmittance plot is compared to the computed transmittance profile using the HITRAN database with Lorentzian lineshapes based on the condition of the gas cell. Figure 5.5a plots the absorption of P(6) line of the $\upsilon_2 + (\upsilon_4 + \upsilon_5)^0_+$ band fitted with a Lorentzian profile. The full-width-half-maximum (FWHM) linewidth is measured to be 0.213 cm^{-1} (6.4 GHz) centered at 3267.65 cm^{-1}. The fit residuals are shown in Fig. 5.5b and have a standard deviation of 4×10^{-3}. The signal-to-noise ratio (SNR) of the comb line is 23 dB measured by the FTIR, which limits the sensitivity of the measurement. The extracted line intensity is 6.87×10^{-20} cm/molecule. From the HITRAN data, the line intensity is 6.61×10^{-20} cm/molecule and the FWHM is 0.197 cm^{-1} (5.9 GHz) based on the self-broadening and nitrogen-broadening effect. Therefore, the deviation of the line intensity is 4% and of the FWHM is 8%. The deviations can be attributed to the beat-note jitter between the CW pump laser and the fem-

tosecond laser system (both free running) at each sampling point. Stabilization of both the pump laser and the reference laser would improve the precision of the sampling step. The frequency accuracy could be further improved through use of a stabilized OFC [24, 82, 140], for example, by self-referencing [140] or by locking to an atomic transition [24, 82]. The SNR of the system could be further improved by averaging over multiple optical spectra, using the FTIR at a higher sensitivity mode and reduction of the pump power noise. As a proof-of-principle demonstration, the scanning technique allows for finer frequency measurements as compared to the typical microresonator-based comb-line spacing.

In summary, we demonstrate a promising approach for a high-spectral-resolution spectroscopy using a scanning microresonator-based OFC with a comb line spacing of over 100 GHz. Rapid thermal tuning of the cavity resonance via an integrated heater (sub-ms level) [21] with a fully automatic scanning procedure would significantly improve the scanning rate. Integrating the heaters on such silicon microresonators with PIN structures could be challenging and has not been demonstrated yet. A flatter pump power would allow for a complete scan over one FSR to access the entire optical spectral range. A silicon microresonator with a larger radius will benefit from the current scanning range. In the mid-IR, commercial QCL's have shown a broadband tuning flexibility over 60 cm^{-1} (1.8 THz) and the potential to pump the microresonators. Recently there has been progress on integration of QCL's on a silicon platform [141]. We believe that with continued development of QCL's, our technique would provide a compact spectrometer in the mid-IR with high sensitivity and high resolution for on-chip gas-phase spectroscopy.

CHAPTER 6

DUAL-CAVITY-BASED COMB SPECTROSCOPY

6.1 Introduction

A major application of chip-scale OFC's is as a broadband optical source for massively parallel measurements of diverse molecules (Fig. 6.1). While fiber-based combs are a mature technology, the fine comb line spacing (100 MHz) requires a high-resolution spectrometer to directly resolve individual lines. In contrast, microresonator-base OFC's have a much larger spacing (from a few GHz to 1 THz) which enables comb-resolved detection using only a coarse-resolution spectrometer. This offers a significantly faster acquisition rate and potential for combining with an on-chip spectrometer [142]. While comb spacings of 2-10 GHz have been demonstrated [22, 35, 143], most microresonator platforms have inherently large comb line spacings which makes them unsuitable for most gas-phase spectroscopy that requires MHz-level resolution [77]. In addition, precise control of both the pump laser frequency and the cavity resonance is needed for comb generation, modelocking, and stabilization [16,17,144].

In this paper, we address both challenges using a fiber-microresonator dual-cavity scheme and a spectrometer with a coarse spectral resolution of 60 GHz. In our dual-cavity scanning comb (DCSC), the CW pump laser is replaced by a gain medium in a cavity that contains the Si_3N_4 microresonator [145–147]. We scan the entire comb spectrum over one free spectral range (FSR, 195 GHz) by simply tuning the microresonator cavity resonance via an integrated heater, which removes the complexity of synchronization of pump laser tuning and

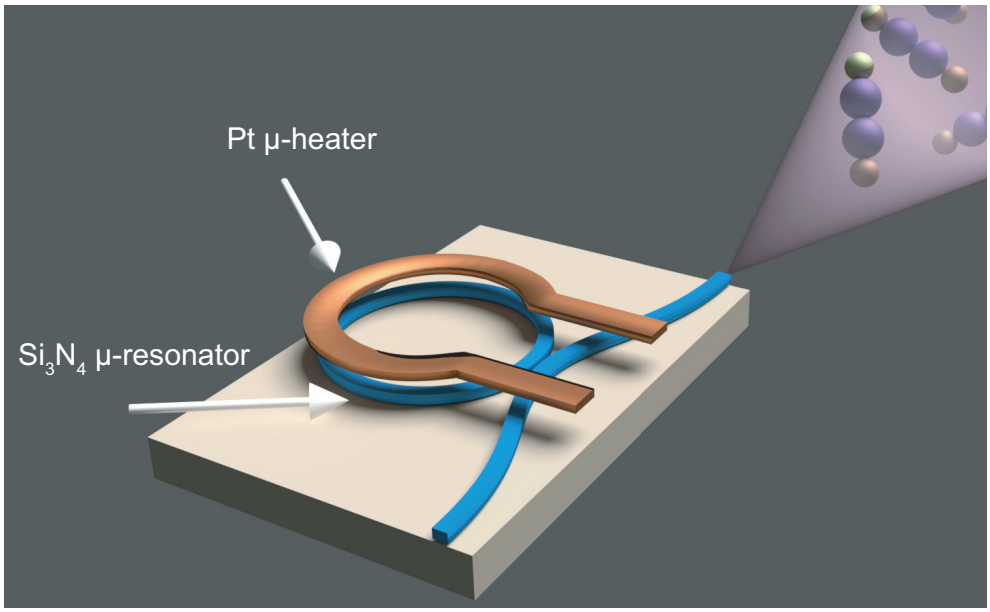

Figure 6.1: Microresonator-based molecular spectroscopy. A Si_3N_4 microresonator (with bus waveguide) is drawn with an integrated heater on top. The waveguides are cladded with silicon dioxide of 2.5 μm thickness (not shown), above which the integrated heater is fabricated.

cavity tuning [100,144]. Interleaving all the spectra [128,131,136,138] as the microresonator is tuned improves the spectral resolution to < 250 MHz. We show that this system can be used for relatively high-spectral-resolution absorption measurements of acetylene gas at 400 Torr and 6 Torr. Such DCSC offers the potential for a turn-key, on-chip broadband spectrometer with fast acquisition speed suitable for trace gas sensing.

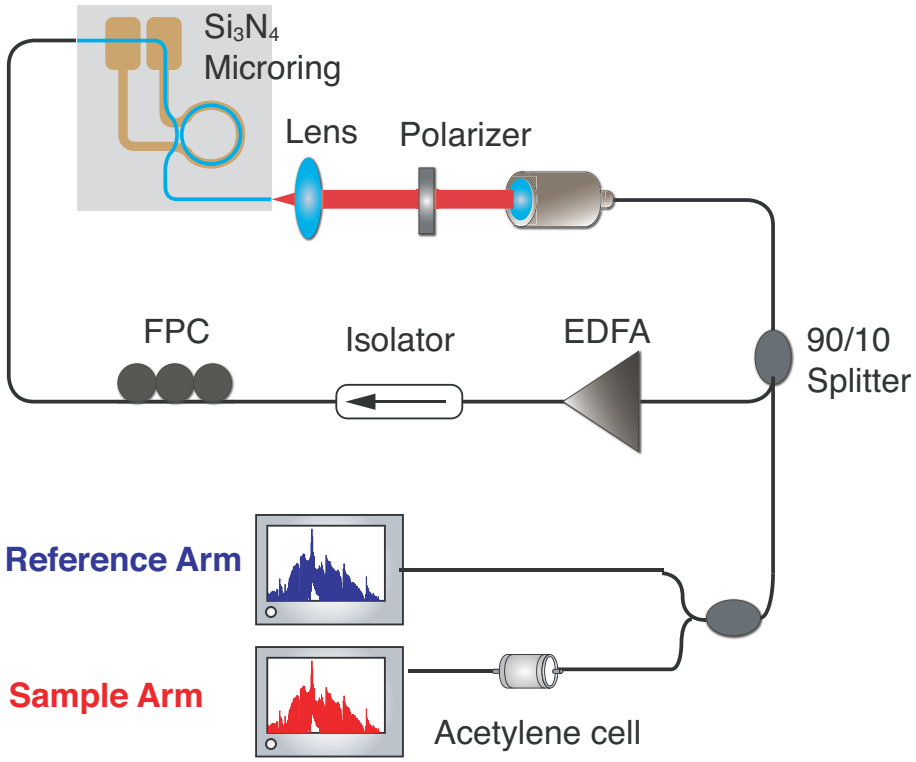

Figure 6.2: Experimental setup for dual-cavity scanning comb. The first cavity (in gray region) is the Si_3N_4 microresonator for optical parametric oscillation. The second cavity is the external loop formed by the bus waveguide, polarization components, EDFA and an optical isolator. 10% of the power in the external cavity is coupled out via a 90/10 coupler. We use two optical spectrum analyzers, one for measuring the acetylene absorption spectrum and the other for calibration. FPC: fiber polarization controller, EDFA: erbium-doped fiber amplifier.

6.2 Results and discussion

6.2.1 Experimental setup

Our experimental setup is shown in Fig. 6.2. We use an oxide-cladded Si_3N_4 microresonator with a radius of 120 μm and a loaded Q of 1 million as the Kerr comb platform. The microresonator is engineered to have anomalous group-

velocity-dispersion for the fundamental transverse electric modes with a cross section of 730×2200 nm. An integrated platinum resistive heater [21,100] is fabricated on top of the oxide cladding to locally change the temperature near the microresonator with a resistance of 260 Ω (Fig. 6.1). The bus waveguide forms part of the external cavity and couples to the Si_3N_4 microresonator, similar to the scheme reported by Johnson *et. al.* [145]. The external cavity also includes an erbium-doped fiber amplifier (EDFA), polarization components, and an optical isolator. The generated optical spectrum is measured with an optical spectrum analyzer (OSA) after a 90/10 coupler. By setting the polarization to quasi-TE and increasing the EDFA gain, an OFC spectrum spanning 1450 - 1700 nm is achieved [Fig. 6.3(a)] at an EDFA power of 200 mW. The optical power in the bus waveguide is 40 mW due to a 7-dB coupling loss into the chip. Due to the large Purcell factor of the microresonator, the EDFA preferentially amplifies the oscillating modes that lie within a microresonator resonance, and the resulting lasing mode serves as the pump for the parametric oscillation in the microresonator [145]. In contrast to the conventional CW pump laser, comb generation is self-starting once the EDFA reaches the threshold power, without the need to sweep the laser into resonance [16]. Moreover, it does not suffer from the disruption of comb generation due to the drifts of the relative pump-cavity detuning. Most importantly, this dual-cavity configuration is ideal for tuning the comb spectrum since only the position of the microresonator resonance needs to be tuned and the ”pump” mode follows accordingly.

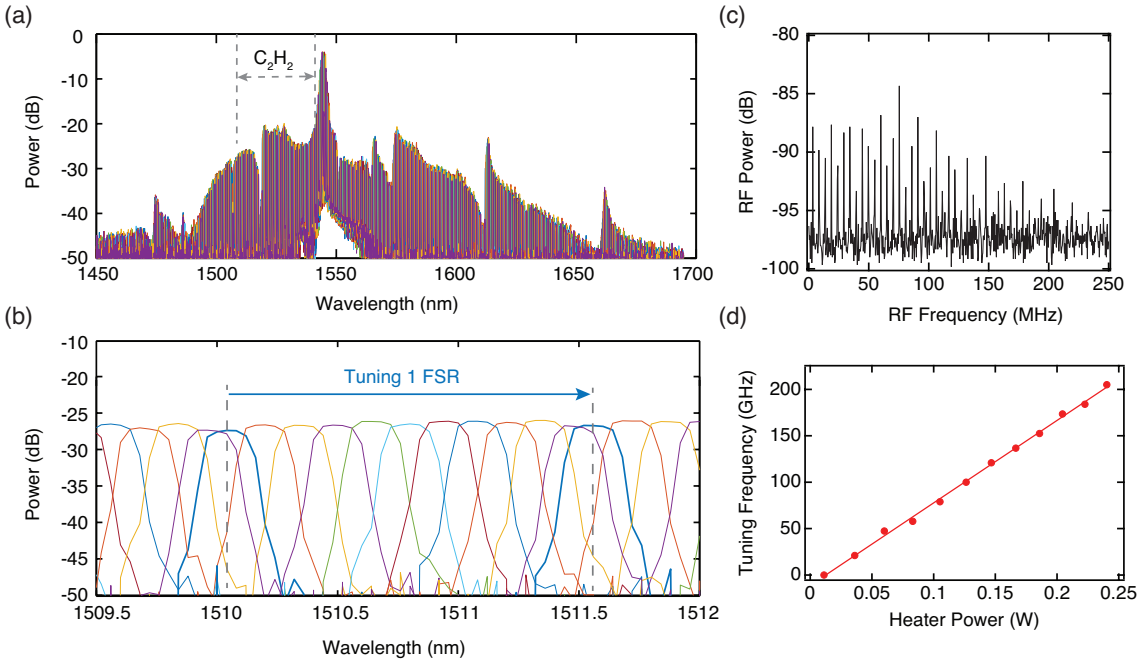

Figure 6.3: Characterization of the comb tuning. (a) The recorded frequency comb spectra at different heater voltages. The spectrum spans from 1450 to 1700 nm at an EDFA output power of 200 mW. Multiple mode crossings cause the spectral dips and affect the bandwidth. The absorption of acetylene resides between the grey dashed lines which spans about 40 nm. (b) Zoom-in spectra of (a), which shows the comb line is tuned over one full free spectral range of 195 GHz. (c) The radio-frequency spectrum of the comb. The line spacing is 5.2 MHz, which corresponds to an external cavity length of 39.5 meters. The detector bandwidth is 10 GHz. (d) The tuning frequency as a function of heater power consumption. The efficiency is 0.9 GHz/mW.

6.2.2 Characterization

In our experiment, we control the voltage (power) of the integrated heater to shift the cavity resonance via the thermal-optic effect once we generate the comb. The relationship between the heater power and the tuning frequency is characterized by a high resolution OSA (1.25 GHz) and is used for programming the scanning process. The frequency accuracy is also limited by the calibration

of the initial spectrum. We tune the entire comb spectrum over one full FSR (195 GHz) via tuning the integrated heater, and the process is fully driven by a computer algorithm. The heater voltage is initially set at 3V to offset the cavity temperature. Figure 6.3(a) shows 11 different optical spectra over the scanning range at an OSA resolution of 25 GHz. The zoom-in spectra [Fig. 6.3(b)] shows a smooth power flatness of one comb line over the entire scanning range. The appearance of several spectral dips in Fig. 6.3(a) result from the localized dispersion perturbation due to mode crossings [148], which causes low signal to noise ratio (SNR) of the comb lines nearby. In the radio-frequency spectrum of the output [Fig. 6.3(c)], the beat notes separated by 5.2 MHz correspond to the external fiber cavity length of 39.5 meters and the 250-MHz bandwidth corresponds to the microresonator linewidth. This also indicates the OFC is not operating in a modelocked state and has a spectral coherence up to theon resonance linewidth of the microresonator (250 MHz), which is the fundamental limit of the spectral resolution of our system for spectroscopy. However, the resolution could be improved to several MHz level using a Si_3N_4 microresonator with a much higher Q recently reported by Xuan *et. al.* [8] and Ji *et. al.* [7]. Using a low gain EDFA to reduce the fiber cavity length could also improve the coherence of the OFC [146]. Lastly, the heater efficiency is characterized to be 0.9 GHz/mW, as shown in Fig. 6.1(e), corresponding to about 2.2 mW/°C. Thus, we require only 220 mW of electrical power to shift the comb by 195 GHz (one full FSR), which corresponds to a temperature change of 100 °C. The power consumption is orders of magnitude lower than that of a fiber-based comb.

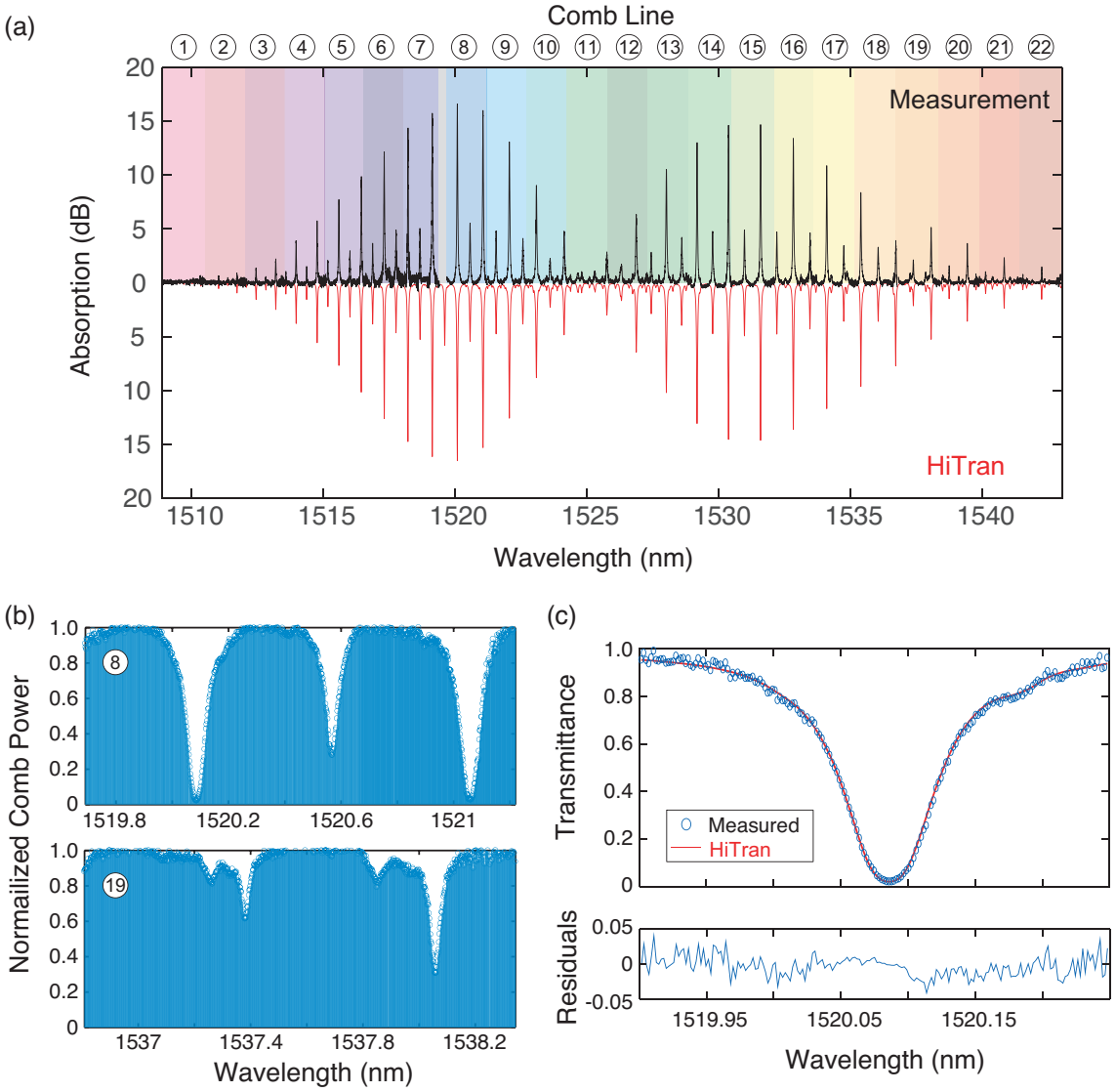

Figure 6.4: Spectral measurements of acetylene. The gas cell is 400-Torr pure acetylene with a length of 5.5 cm. (a) The absorption spectrum is calculated by interleaving 800 spectra at 250 MHz [black curve]. 22 comb lines of the entire optical spectrum is overlapped with molecular absorption. The 1-FSR tuning range of each comb line are shaded in different colors. The grey area (no data points) is due to a missing comb line. The HiTran data is calculated using the gas cell condition and plotted for comparsion [inverted red curve]. (b) The comb line transmission measured by the 8th and 19th comb lines according to (a). (c) The measured transmittance of the R(9e) line of the $\upsilon_1 + \upsilon_3$ band as compared to HiTran. The standard deviation of the residuals is 1.4×10^{-2}.

6.3 Spectroscopy

As a proof-of-principle, we utilize the DCSC for measuring the absorption spectrum of the P and R branches of gas-phase acetylene in the $\upsilon_1 + \upsilon_3$ band, which spans over part of the comb spectrum (1508 - 1543 nm) in the near-IR. As shown in Fig. 6.2, we split the output into the reference and sample arms, each of which is sent to an OSA with a low resolution of 60 GHz. The reference arm is used for calibration of the spectrum. We use a 5.5-cm-long acetylene cell at 400 Torr in the sample arm. The scanning process is programmed to be 250 MHz per step. We acquire 800 spectra with a speed of 0.5 s per acquisition, which is limited by the slow readout time from the OSA. The absorption is calculated based on the spectral measurement in the reference and sample arms. Figure 6.4(a) shows the measured absorption spectrum of acetylene [black curve], which is recorded by interleaving 800 spectra taken with 250-MHz steps. The repetition rate change with the temperature is taken into account to improve the frequency accuracy [144]. We compare the measured spectrum to that [inverted red curve] based on the HiTran database, which is in good agreement. A total of 22 (labelled) out of 150 comb lines is used for the absorption measurement in the P and R branches, each of which is shaded in different colors in the Fig. 6.4(a). The small grey area between 7th comb line and 8th comb line is due to a missing comb line, which is attributed to a mode crossing effect, therefore the 7th comb line is tuned slightly more to cover its area. Figure 6.4(b) shows the measured transmission of the 8th and 19th comb lines that are each tuned over one FSR range. Several absorption features with different depth and width are clearly captured. Figure 6.4(c) shows one measurement of the R(9e) line of the $\upsilon_1 + \upsilon_3$ band as compared to HiTran. A standard deviation of the residual is 1.4×10^{-2},

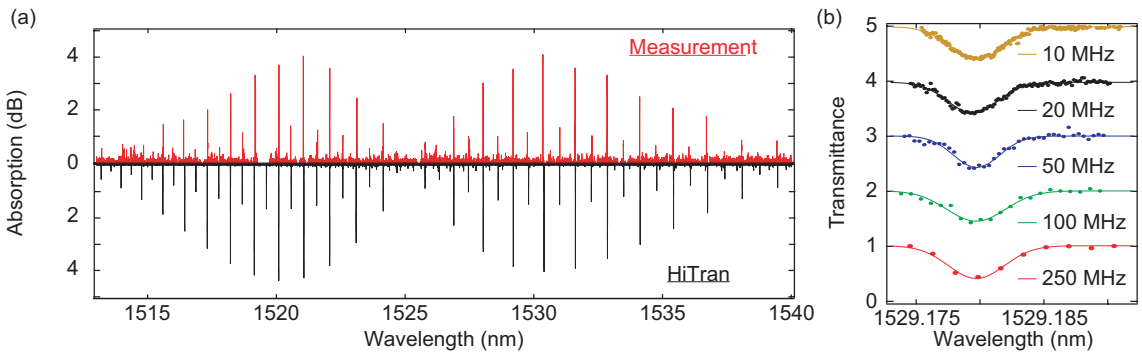

Figure 6.5: Measurement of a low-pressure cell of acetylene at 6 Torr. The effective cell length is 11 cm. (a) Absorption spectrum by interleaving 800 spectra at a 250-MHz step, similar to fig. 6.4(a). (b) Transmittance of the P(7e) line measured at different scanning steps of 10, 20, 50, 100 and 250 MHz.

which is largely limited by the SNR of the corresponding comb line. A drop port device for outputting the OFC spectrum should improve the coupling efficiency and the SNR's.

We also apply this technique for measuring an acetylene cell at a lower pressure of 6 Torr with an effective length of 11 cm. Figure 6.5(a) shows the measured absorption spectrum [red curve], and we compare this to a model spectrum [inverted black curve] based on a convolution of the microresonator lineshape and the absorption spectrum from HiTran database, and good agreement is observed. Due to the fact that the comb linewidth is comparable to the absorption linewidth at this pressure, the measured absorption feature becomes weaker which causes some weak absorption peaks to be smeared as seen from Fig. 6.5(a), which could be addressed by using a higher Q-factor microresonator. In addition, the scanning step can be easily tuned in order to optimize for different gas-cell conditions. For example, Fig. 6.5(b) shows the measurement of the P(7e) line of the $\upsilon_1 + \upsilon_3$ band at different scanning steps of 10, 20, 50, 100 and 250 MHz. We measure a 380-MHz half-width-half-maximum width of the

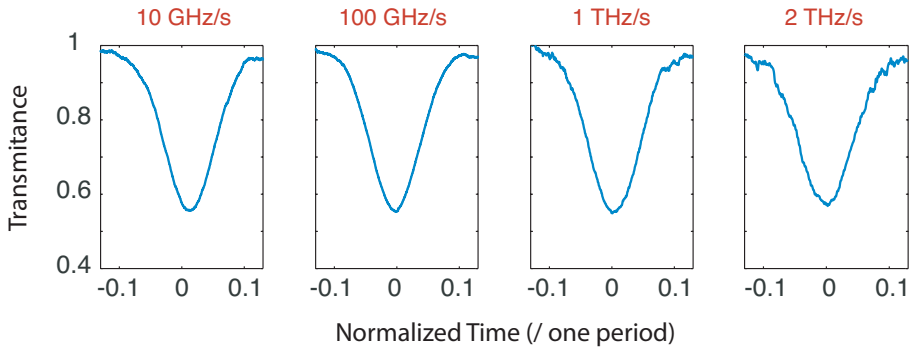

Figure 6.6: Measurement of the P(7e) line at different scanning speeds (single-shot). The corresponding comb line is filtered out using a 1-nm bandpass filter after the acetylene cell and then sent to a fast photodetector. The heater is programmed to sweep a range of 5 GHz at 1 Hz, 10 Hz, 100 Hz, and 200 Hz, which corresponds to a tuning speed of 10 GHz/s, 100 GHz/s, 1 THz/s and 2 THz/s. The absolute timing of recording time traces is random.

absorption line which also agrees well with the HiTran data.

Due to a fast response time of integrated heaters (about 10 μs), the scan can be performed significantly faster than the piezo-tuning speed of CW lasers (> 1 ms). While the acquisition speed is currently limited by the slow readout time of the OSA, by using a low-resolution grating along with an InGaAs camera (< 100 μs per image), the data-acquisition rate can be significantly increased to enable real-time output. As a proof-of-principle, we filtered out the comb line near the P(7e) line using a 1-nm bandpass filter and sent it to a photodetector (Thorlabs PDA10CS, bandwidth 17 MHz). We sweep the frequency by 5 GHz by sending a periodic triangular voltage function to the heater at rates of 1 Hz, 10 Hz, 100 Hz and 200 Hz. The recorded single-shot oscilloscope traces are shown in Fig. 6.6 with time normalized to one period, corresponding to a tuning speed of 10 GHz/s, 100 GHz/s, 1 THz/s and 2 THz/s. At 1 THz/s, the absorption features start to show distortion, which indicates that our scheme can potentially

achieve a total acquisition time of < 2 s to complete the current 200-GHz tuning if combined with a grating and a line camera. While microresonator-based dual-comb spectroscopy [34, 35, 37] can achieve much faster acquisition speed (2 μs [34]), it requires delicate control of two modelocked frequency combs with external pump lasers, and its spectral resolution suffers from the large optical line spacing (10 - 200 GHz) which is more suitable for condensed phase studies. Our DCSC approach offers a much simpler and more robust approach for gas-phase spectroscopy with a reasonably fast acquisition rate.

6.4 Conclusion

In summary, we demonstrate a new approach to gas-phase spectroscopy using microresonator-based OFC technology. We program an integrated heater to tune the comb spectrum over one full FSR in a dual-cavity scheme and measure the molecular fingerprint of acetylene in the $\upsilon_1 + \upsilon_3$ band. Parallel detection of multiple trace gases can benefit from the broadband comb generated from microresonators since only 15% of the spectrum was used here for the acetylene measurements. Integrated heaters offer a high tuning efficiency at low electrical power consumption, a rapid tuning speed, and the capability of full integration with microresonators. Moreover, our DCSC can be extended to the important mid-IR regime, where molecules have fundamental vibrational transitions, by replacing EDFA with a quantum cascade amplifier. Combining with the silicon microresonator [32], a quantum or interband cascade amplifier with a minimum power of 35 mW (at 2.8 μm) or 80 mW (at 3 μm) could potentially be applied for gas sensing in the mid-IR using our configuration. With a higher Q-factor microresonator [7, 8], a chip-scale gain medium [65, 149] and an on-chip spec-

trometer [142], we envision a lab-on-chip system with real-time output and high spectral resolution suitable for gas sensing over a wavelength range far larger than what could be achieved with a tunable laser.

CHAPTER 7

OUTLOOK

This work represents a significant advance to the fields of microresonator combs and mid-infrared spectroscopy. We present the first demonstration of a soliton modelocked frequency comb and dual-comb spectroscopy in the mid-IR regime. It points out new opportunities for microresonator-comb systems towards vibrational spectroscopy in the mid-IR, where sources still remain under development. We believe our work specifically addresses the potential of linear dual-comb spectroscopy for liquid/condensed matter phase studies with potential applications and prospects that are truly interdisciplinary and represents a novel direction for research. In addition, our technique of scanning comb overcomes the resolution limit of integrated photonic devices and opens up new applications of trace gas sensing. With continued progress of quantum cascade laser (QCL) and mid-IR instrumentation such as detectors and digitizers, we envision a spectroscopy laboratory on a chip that could realize real-time fingerprinting with label-free and high-throughput detection of trace molecules. There are several highly impactful directions based on what has been achieved in this thesis.

The first goal is to pump a silicon microresonator using a QCL for realization of an on-chip, compact and octave spanning mid-IR frequency combs which spans over 3 - 6 μm. QCL's utilize intersubband transitions to access the mid-infrared spectral region through engineering of multiple quantum well heterostructure. QCL's offers great mid-IR spectral coverage from 3 - 25 μm, single frequency operation using an external cavity configuration and high power output. There are several main challenges: the silicon microresonator exhibits

significant higher loss due to the oxide cladding absorption beyond 3 μm, and the QCL's still have relatively large spectral linewidth and limited mode-hop-free tunability. A novel design of silicon devices with new cladding materials should be developed along with continued efforts on increasing the Q-factor of microresonators. Additional tuning method of cavity resonance should be utilized to overcome the thermal shift for comb generation, *e.g.* integrated heaters. Moreover, using a quantum cascade amplifier coupled to a microresonator could be an alternative solution. Interband cascade laser and interband cascade amplifier could also serve as possible pump sources.

Another exciting application will be to combine dual-comb technique with microfluidic technology for label-free analyte detection for synthetic biology and chemistry. Microfluidic device as a continuous-flow platform for cell-sorting or chemical synthesis has become popular because it allows for safe and rapid microreactions using picoliter reagent volumes with high selectivity over a small footprint. It produces a large amount of information in real time about reaction kinetics, reaction intermediates, catalytic activities and selection. Integrating the microfludic reactor with an in-line monitoring tool at a kHz or higher sampling rate is necessary for real-time analysis of biomolecules or chemical production. Typically in-line analysis tool is based on Raman and UV/Visible spectroscopy both of which has limited spectral acquisition speed or fluorescence spectroscopy which requires labeling the target molecule group. Therefore, microresonator-based dual-comb spectroscopy, which is a rapid, non-destructive, label-free, and sensitive technique, becomes a promising tool for such applications where real-time data series is desired. Benefit from the large line spacing of microcombs, dual-comb spectroscopy could enable extracting spectral information on sub-μs scale and contribute to microflu-

idic applications such as point-of-care and dial-a-molecule.

APPENDIX A

RAMAN SCATTERING EFFECT

A.1 Coherent mid-IR combs in presence of Raman scattering

We investigate the comb generation dynamics in the silicon microresonator for the case in which the pump wavelength is set to 3.07 μm and the reverse-bias voltage on the PIN structure is set to -12 V. As the pump wavelength is tuned into a cavity resonance, we characterize the optical spectrum and the PIN-based RF spectrum as shown in Fig. A.1(a). As the pump is tuned further [Fig. A.1(a)(i) – A.1(a)(iii)], an abrupt transition in the optical spectrum occurs along with a reduction of the RF amplitude noise [Fig. A.1(a)(iv)]. Additionally, we observe an abrupt increase in DC current from 0.945 to 1.17 mA [Fig. A.1(b)], which is suggestive of modelocking and pulse formation since the 3PA-induced DC current is very sensitive to temporal peak power in the cavity.

Figure A.2 shows the low-noise comb spectrum in the frequency domain. We achieve a nearly-octave-spanning frequency comb spanning 70 – 122 THz, which corresponds to 2460 – 4278 nm in wavelength. Interestingly, the transition to the low-noise state coincides with the emergence of multiple Raman oscillations, implying that the low-noise state is strongly influenced by simulated Raman scattering (SRS), The Raman effect has been previously observed and characterized in silicon nanowaveguides with a Raman frequency shift of 15.6 THz [150, 151] and a narrow linewidth of 105 GHz. Previous theoretical investigations have indicated that comb generation based on the Raman effect is possible with the comb spacing defined by the Raman shift [98]. In our experiment, we observe distinct Stokes and anti-Stokes peaks separated by 15.52

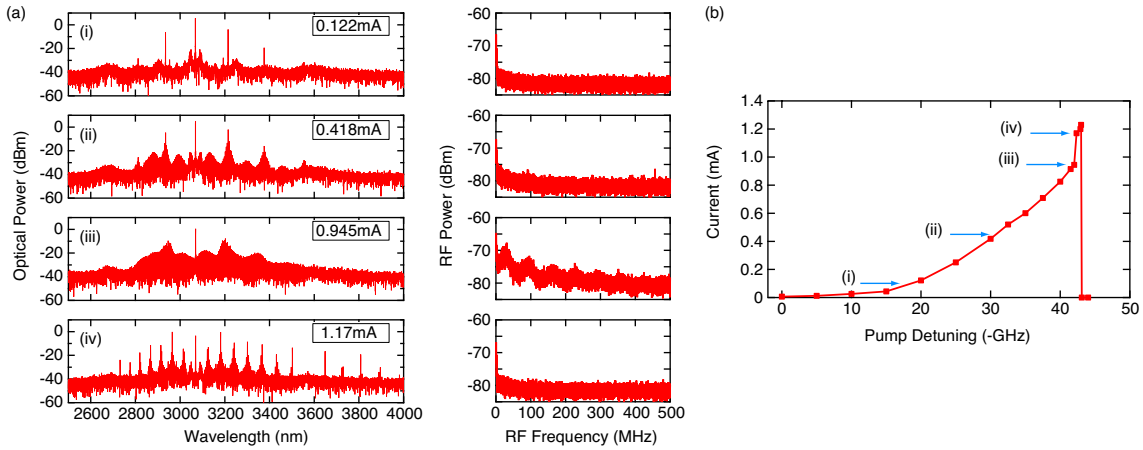

Figure A.1: Comb generation dynamics in a silicon microresonator. (a) Optical and RF spectra for generated comb as pump is red-detuned. (b) Measured DC component of the FC induced photocurrent as a function of pump detuning. We observe an abrupt increase in current as the comb transitions to a low-noise state.

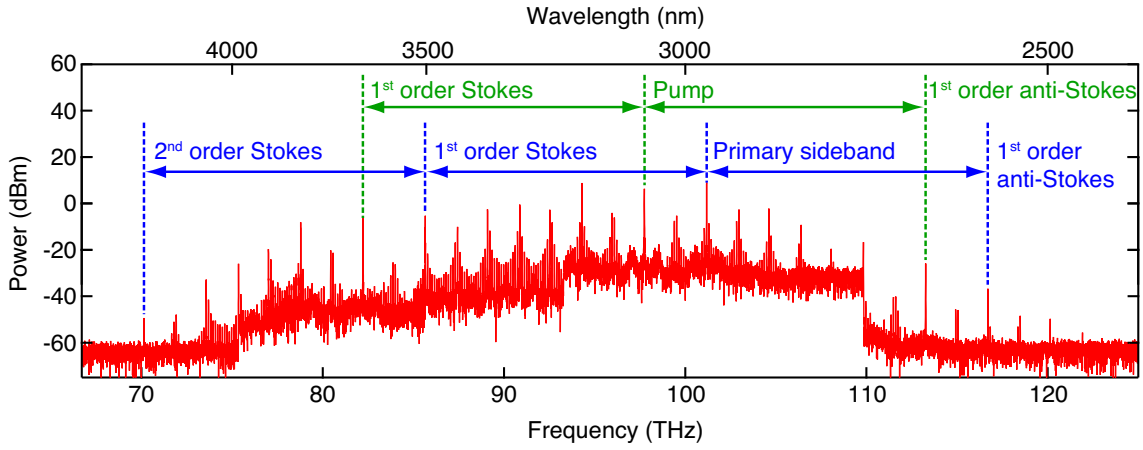

Figure A.2: Optical spectrum of coherent mid-IR comb generation in a silicon microresonator. The generated comb shows interplay between FWM and SRS. The Raman interaction with respect to the pump mode is shown in green. The interaction with respect to the primary sideband is shown in blue.

THz with respect to the pump frequency (indicated with green arrows in Fig. A.2). Furthermore, other strong comb lines are separated by the Raman shift, and we observe cascaded Raman Stokes lines with respect to the primary comb line (indicated with blue arrows in Fig. A.2). Generation of higher-order Raman lines is limited by the high optical losses due to the silica cladding beyond 4.3 μm. Another indication of the SRS process is the significantly depleted pump frequency line with power lower than the primary FWM sideband. The fact that the frequency shift of the observed Raman peaks is lower than the value of 15.6 THz at room temperature could be attributed to: 1) the spectral overlap between the cavity resonance and the Raman gain profile 2) and the decreased Raman shift in silicon with higher temperatures [152], which is due to absorption and 3PA-induced thermal effects in the silicon microresonator. The large FSR of our device (127 GHz), along with the large Raman shift and narrow Raman gain bandwidth, makes the generation of Raman-FWM frequency comb much more sensitive to the pump laser detuning and the pump power. Another feature of this Raman-FWM comb is that, in contrast to Hansson, *et al*. [98], our generated comb shows discrete high power comb lines with a spacing of 1.7 THz, which corresponds to 13 FSR's and 1/9 of the Raman frequency shift. The spacing is defined by the interplay of FWM and SRS when pumping at anomalous GVD. The high power comb lines that emerge in this final state dominates the phase locking and pulse formation. Our results indicate that, in contrast to conventional FWM-induced phase-locked frequency combs, phase-locking in our system occurs as a result of a combination of coherent generation of Stokes and anti-Stokes frequencies from SRS [153], and FWM interactions between the different Stokes and anti-Stokes pairs, enabling broadband coherent frequency comb generation.

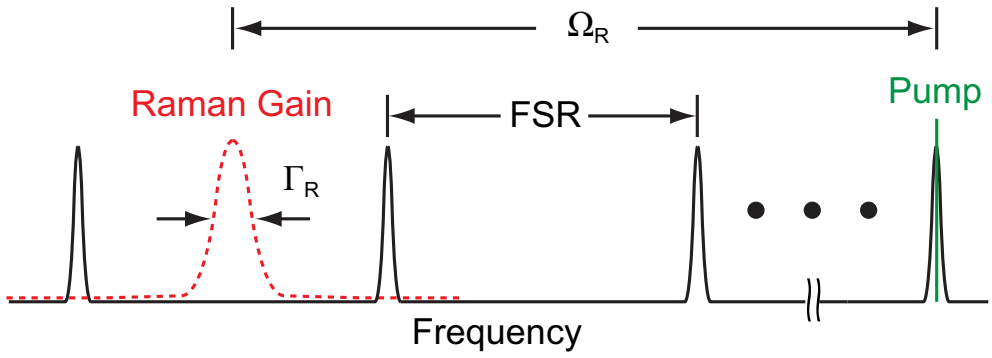

Figure A.3: Scheme for suppression of effective Raman gain in microresonators. The free spectral range is chosen such that when the peak of the Raman gain lies between two adjacent cavity resonances, the nearest Stokes cavity mode is sufficiently far detuned from the gain peak. Ω_R is the Raman frequency shift (*eg.* 40 THz for diamond and 15.6 THz for silicon).

A.2 Competition between Raman and Kerr effects in crystalline microresonators

A.2.1 Introduction

The effects of Raman scattering on parametric oscillation and comb generation have been explored [4, 154–161]. For example, self-frequency shifts have been observed in amorphous materials such as silica and silicon nitride [162, 163], where the presence of a red-shifted Kerr soliton has been attributed to the Raman effect. Furthermore, Raman lasing and Raman-FWM interactions have been observed in crystalline structures such as magnesium fluoride, silicon, diamond, and aluminum nitride [4, 156–158, 160], resulting in non-trivial nonlinear interactions in the microresonator and the disruption of soliton formation.

We theoretically investigate the combined effects of Raman and parametric

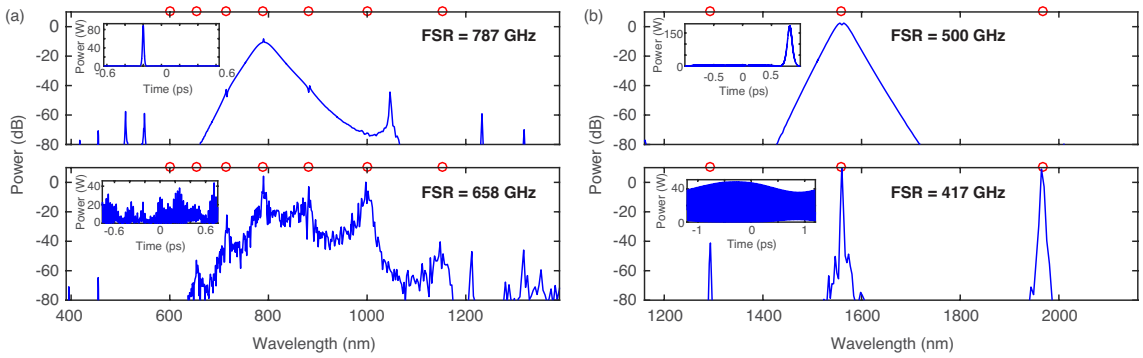

Figure A.4: (a) Simulated spectrum for comb generation in diamond microresonators pumping at 790 nm for FSR's of 787 GHz (top) and 658 GHz (bottom). (b) Simulated spectrum a 1560 nm pump for FSR's of 500 GHz (top) and 417 GHz (bottom). The insets show the corresponding temporal profile. The red circles indicate the Raman frequency shift.

gain on Kerr comb generation in diamond and silicon microresonators. Diamond is an ideal platform for Kerr combs since it has a large Kerr nonlinearity ($n_2 = 1.3 \times 10^{-19}$ m^2/W), enables broadband parametric gain with dispersion engineering of the waveguides, and has a wide optical transparency window covering the UV to the mid-infrared (mid-IR) [45]. It also has a strong Raman gain ($g_R = 26$ cm/GW at 800 nm) with a narrow linewidth ($\Gamma_R/2\pi = 60$ GHz). Silicon is a well established photonics platform and offers promise for frequency comb applications in the mid-IR [3, 32, 34]. It has an even larger nonlinearity than diamond ($n_2 = 3 \times 10^{-18}$ m^2/W at 3100 nm) [76] and we estimate a Raman gain $g_R = 3$ cm/GW for a Stokes field at 3700 nm [164, 165], with a linewidth $\Gamma_R/2\pi = 105$ GHz. Since the Raman gain is large and inherent in these crystalline materials, it can play an integral part in the nonlinear dynamics in the microresonator. We show that it is possible to minimize the strength of the Raman effect by designing the device geometry. Our analytic and numerical studies show that tuning the free-spectral range (FSR) of the microresonator can be used to achieve a Kerr comb state or a Raman oscillation state. For Kerr comb

generation, the FSR must be chosen such that the peak of the Raman gain is far detuned from any cavity resonance in order to suppress the Raman gain as compared to the parametric gain. This condition posts a maximum limit of the microresonator's dimension (or round-trip path length), especially for diamond microresonators operating in the visible regime where the Raman gain is typically much larger. In addition, we investigate the competing effects near the FSR limit in silicon microresonators. Our analysis offers a novel route to achieving Kerr comb generation in the presence of strong Raman effects and can be generalized to other nonlinear crystalline materials with a narrow Raman gain feature.

First, we analyze competing Raman and Kerr effects in crystalline microresonators. The parametric gain can be expressed as $G_{NL} = g_K PL/A$, where the parametric gain coefficient is $g_K = 4\pi n_2/\lambda$ where λ is the pump wavelength, n_2 is the nonlinear index coefficient, P is the pump power, and A is the effective optical mode area. Similarly, the Raman gain can be written as $G_R = g_R PL/A$. In order to achieve parametric oscillation and Kerr comb formation in a crystalline microresonator, the Raman gain must then be suppressed by more than the ratiog_R/g_K between the two gain coefficients. By assuming that the Raman spectral gain profile can be expressed as a Lorentizan $g_R(\delta) = g_R/(1+4\delta^2/\Gamma_R^2)$ and choosing the FSR such that the peak Raman gain is centered between two cavity modes (see Fig. A.3), the effective gain at the nearest Stokes cavity mode will be suppressed by more than g_R/g_K if $\delta/\Gamma_R > \frac{\sqrt{g_R/g_K}}{2}$. Thus positioning the peak Raman gain between two cavity resonances (Fig. A.3) is critical for pure Kerr comb generation.

A.2.2 Diamond microresonator

In diamond, for a pump wavelength of 800 nm, the Kerr and Raman gain coefficients are $g_K = 0.2$ cm/GW and $g_R = 26$ cm/GW [166]. To achieve pure comb formation, the Raman gain must then be suppressed by more than 130×. This corresponds to $\delta/2\pi = 342$ GHz for diamond, indicating that an FSR > 684 GHz is required. Similarly, we calculate the gain coefficient at telecommunications wavelengths, taking into account the wavelength dependence of both the Kerr and Raman gain [158, 166, 167]. At a pump wavelength of 1560 nm, the gain coefficients are $g_K = 0.1$ cm/GW and $g_R = 6$ cm/GW, which requires an FSR > 464 GHz to suppress Raman gain. The FSR threshold is lower at 1560 nm since the Raman gain coefficient decreases more rapidly with increasing wavelength as compared to the Kerr gain coefficient [166].

We confirm this analysis by performing simulations of the comb generation dynamics using the modified Lugiato-Lefever equation [44–49], including effects of higher-order dispersion, self-steepening, and the Raman effect. Here, we assume he pump and the Stokes fields are co-polarized. The equation can be written as

$$T_R \frac{\partial E(t,\tau)}{\partial t} = \left[-\alpha - i\delta_0 + iL \sum_{n\geq 2} \frac{\beta_n}{n!} \left(i\frac{\partial}{\partial \tau} \right)^n + i\gamma L \left(1 + \frac{i}{\omega_0} \frac{\partial}{\partial \tau} \right) \int_0^\infty R(t') |E(t-t',\tau)|^2 dt' \right] E(t,\tau) + \sqrt{\kappa} E_{in} \tag{A.1}$$

where T_R is the round-trip time, $E(t,\tau)$ is the field in the microresonator, α is the round-trip loss, δ_0 is the pump-cavity detuning, β_n is the nth order dispersion coefficient, γ is the nonlinear parameter, $R(t)$ is the Raman response, κ is the power

transmission coefficient of the bus-waveguide-microresonator coupling region, and E_{in} is the input field. We simulate the dispersion of the waveguide using a finite-element mode solver. The waveguide cross section of the diamond microresonator is 300×400 nm which allows for anomalous GVD at 790 nm. Figure A.4(a) shows the simulated spectra for two different FSR's, 787 GHz and 658 GHz, respectively. The dispersion, propagation loss (0.5 dB/cm), and pump power (300 mW) are the same for the two FSR's. The spacings of the red circles in the spectral plots correspond to the Raman frequency shift. Depending on the FSR, we observe two different final states, corresponding to Kerr comb formation [Fig. A.4(a) top] and Raman oscillation [Fig. A.4(a) top]. Our simulations agree well with the calculated FSR required for pure Kerr comb generation. The larger FSR microresonator allows for suppression of the Raman gain enabling Kerr combs and soliton formation [Fig. A.4(a) inset], whereas the smaller FSR microresonator does not suppress the Raman gain, resulting in Raman oscillation becoming dominant and destabilizing the modelocking process of Kerr frequency combs. We also observe comb lines between the Raman peaks, which we attribute to Raman-assisted FWM. We observe this threshold behavior for Kerr comb formation for other waveguide cross sections provided that the GVD is anomalous and is largely dependent on the microresonator FSR. In addition, we simulate the dynamics for 1560-nm pump using a waveguide cross section of 700×800 nm which allows for anomalous GVD at the pump. Figure A.4(b) shows the simulated spectra for two different FSR's, 500 GHz and 417 GHz, respectively. Our simulations show that, similar to the 790 nm pump case, a Kerr comb is generated for the 500 GHz FSR, but Raman oscillation dominates for 417 GHz, which agrees well with our threshold calculation. Figure A.5 shows experimental results showing the two different regimes below and above the FSR

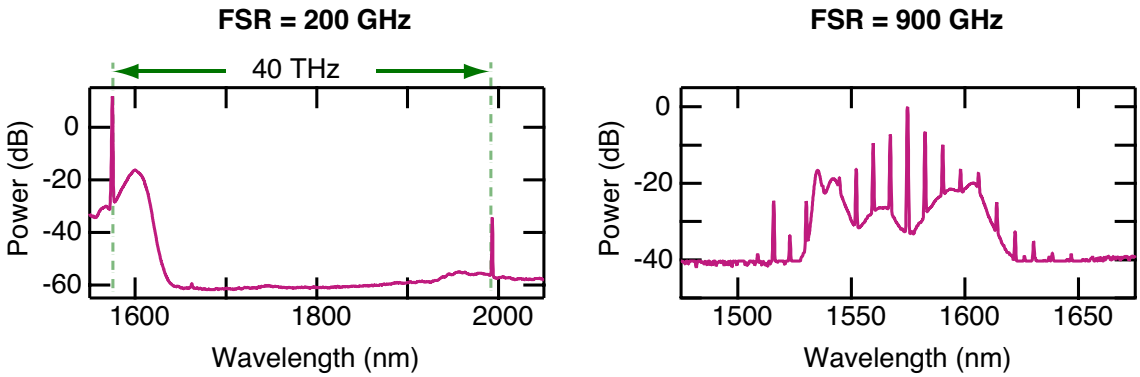

Figure A.5: Experimental spectrum for comb generation in diamond microresonators pumping at 1575 nm for two different FSR's of 200 GHz and 900 GHz.

threshold (200 GHz and 900 GHz) pumping at 1575 nm. The waveguide cross section is 700×800 nm. Raman oscillation is observed 200-GHz FSR, and Kerr comb formation is observed without Raman effects for 900-GHz FSR [23, 158]. We conclude that choosing a large FSR is critical for Raman suppression and generation of a pure Kerr comb, particularly at lower wavelengths near visible where the Raman gain is large. The FSR threshold of 684 GHz at 800 nm corresponds to a microring radius of 26 μm. For such small device dimensions, the contribution from bending losses could increase, leading to lower quality factor devices, and the large FSR can be detrimental to various applications that require smaller comb spacings.

A.2.3 Silicon microresonator

We perform a similar analysis for silicon microresonators operating in the mid-IR. For a 3100 nm pump wavelength, the Kerr and Raman gain coefficients are $g_K = 1.21$ cm/GW and $g_R = 3.05$ cm/GW, respectively. The smaller Raman gain coefficient results in a smaller ratio between the two gain coefficients

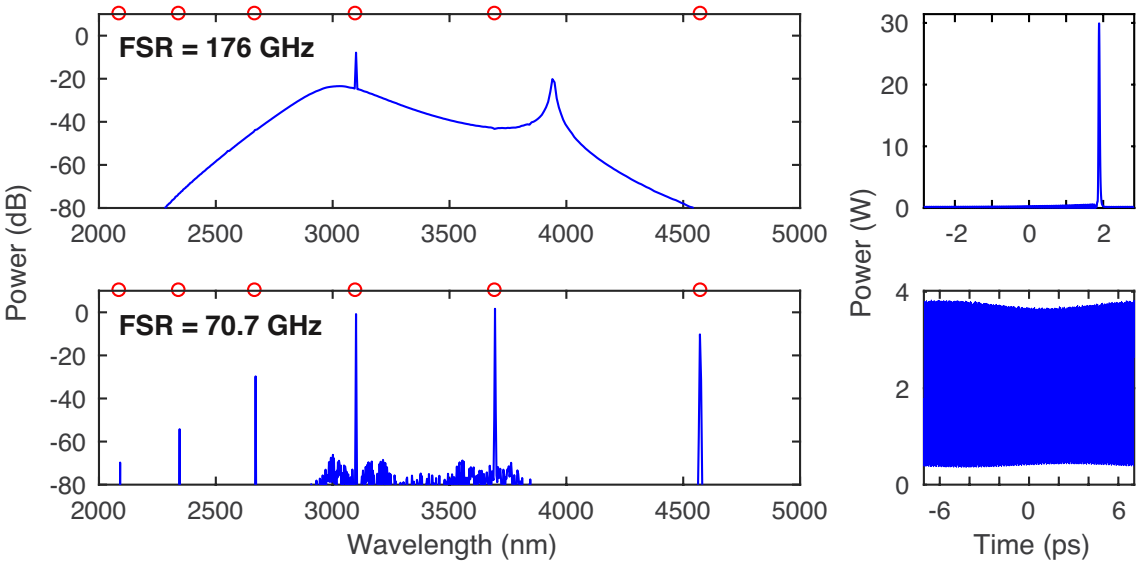

Figure A.6: Simulated spectrum (left) and temporal profile (right) for comb generation in silicon microresonators pumping at 3100 nm for FSR's of 176 GHz (top) and 70.7 GHz (bottom).

g_R/g_K. Thus, the suppression of Raman for pure Kerr comb formation requires an FSR > 167 GHz. We consider an etchless microresonator with a cross section of 500×1400 nm which allows for anomalous GVD at the pump wavelength of 3100 nm. Similar to our diamond analysis, we fix the dispersion, propagation loss (0.5 dB/cm), and pump power (100 mW) for each FSR we investigate. Figure A.6 shows the simulated spectra and corresponding temporal profiles for two different FSR's of 176 GHz and 70.7 GHz. We observe pure Kerr comb formation with minimal Raman effects for the large FSR which again agrees with the threshold calculation. For 70.7 GHz, the Raman effect dominates and we only see Raman oscillation for this pump power. For FSR's between 176 GHz and 70.7 GHz, we observe Raman and Kerr oscillation in the same device for different pump-cavity detunings. We believe this behavior can be explained by the Raman-assisted FWM effect which enables parametric oscillation and Kerr comb formation to occur.

We experimentally investigate comb generation in a silicon microresonator with a waveguide cross section of 500×1400 nm [3, 32] and an FSR of 128 GHz, which is chosen here to allow for the Raman gain peak to lie between two cavity resonances which minimizes the Raman effect. Figure A.6 shows the two different realizations of combs generated in the same microresonator for 80 mW of pump power in the bus waveguide. By choosing a different frequency detuning between the pump and the cavity resonance, we generate a comb state with strong Raman oscillation [Fig. A.7 (a)] and a comb state absent of strong Raman effects [Fig. A.7(b)] in the same microresonator. The strong comb lines in Fig. A.7(a) correspond to $1/9^{\text{th}}$ of the Raman frequency shift. In contrast, the strong comb lines in Fig. A.7(b) do not match with the Raman shift and is a result of multiple-soliton formation [32]. Our experimental results indicate that in the intermediate regime between the FSR's of 70.7 and 176 GHz there exists competition between Raman and Kerr effects resulting in the existence of two different states.

We numerically investigate this intermediate regime in silicon where competition between Raman and Kerr gain occurs. Figure A.8 shows the comb generation dynamics for a 129 GHz FSR silicon microresonator as the pump-cavity detuning is increased. In Fig. A.8(a) we see that, as the pump power builds up, Raman oscillation first occurs. As the detuning is increased, Kerr oscillation occurs as well [Fig. A.8(b)]. Furthermore, we observe non-degenerate FWM driven by the pump and Stokes fields. With further detuning, the Raman lines diminish and multi-soliton formation occurs [Fig. A.8(c)]. Figure A.8(d) shows the final detuning step where single soliton formation occurs and the Raman effect is absent. Thus, with sufficient pump powers, Kerr comb formation is still possible in silicon. In this intermediate regime, the Raman effect diminishes and

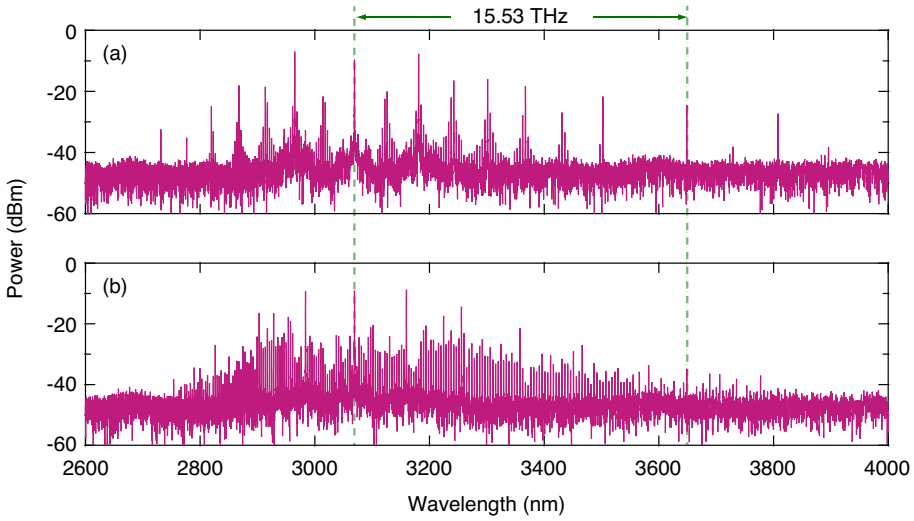

Figure A.7: Experimental spectra for comb generation in a silicon microresonator pumping at 3100 nm (a) with Raman oscillation and (b) without Raman effects. The FSR is 128 GHz, which positions the Raman gain peak between the two cavity resonances of the microresonator.

Kerr oscillation dominates for higher FSR's, and the Raman effect dominates for lower FSR's. This intermediate regime in silicon exists due to the fact that the Raman and Kerr gain are comparable. However, in diamond, this intermediate range is minimal, as the Raman gain is much larger compared to the Kerr gain.

A.2.4 Conclusion

In conclusion, due to the large Raman effect in silicon and diamond, relatively large FSR microresonators are required for mode-locked Kerr comb generation. While silicon offers some flexibility as the Raman and Kerr gain are comparable, the microresonator cavity length must be carefully chosen in diamond due to the high Raman gain, especially at shorter pump wavelengths. Our current investigation considers only one polarization mode for the optical field and does not

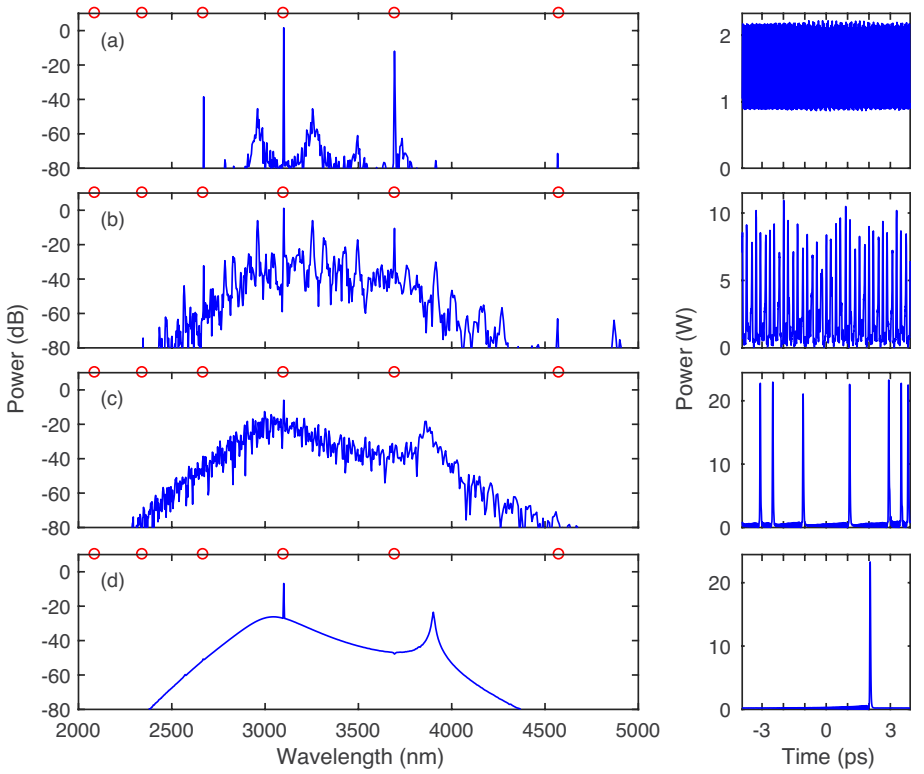

Figure A.8: Simulated spectrum (left) and temporal profile (right) for comb generation in silicon microresonators pumping at 3100 nm for FSR of 129 GHz for pump detunings of (a) -0.9 GHz, (b) 0 GHz, (c) 3.5 GHz, and (d) 4.1 GHz with respect to the cold cavity resonance.

take into account the polarization/crystal-orientation dependence of the Raman process in crystalline materials. For example, in diamond, for certain waveguide propagation directions the Kerr and Raman effects can be segregated into two orthogonal polarizations [167]. Our results indicate that such approaches utilizing the tensorial nature of the Raman process must be employed in order to realize lower FSR combs that are needed for applications such as astronomical spectroscopy and optical clocks.

BIBLIOGRAPHY

[1] B. R. Masters and R. W. Boyd, "Nonlinear Optics, Third Edition," **14**(2), 029,902 (2009).

[2] S. A. Miller, M. Yu, X. Ji, A. G. Griffith, J. Cardenas, A. L. Gaeta, and M. Lipson, "Low-loss silicon platform for broadband mid-infrared photonics," Optica **4**(7), 707–712 (2017).

[3] A. G. Griffith, R. K. W. Lau, J. Cardenas, Y. Okawachi, A. Mohanty, R. Fain, Y. H. D. Lee, M. Yu, C. T. Phare, C. B. Poitras, A. L. Gaeta, and M. Lipson, "Silicon-chip mid-infrared frequency comb generation," Nat. Commun. **6**, 6299 (2015).

[4] A. G. Griffith, M. Yu, Y. Okawachi, J. Cardenas, A. Mohanty, A. L. Gaeta, and M. Lipson, "Coherent mid-infrared frequency combs in silicon-microresonators in the presence of Raman effects," Opt. Express **24**(12), 13,044–13,050 (2016).

[5] N. Singh, D. D. Hudson, Y. Yu, C. Grillet, S. D. Jackson, A. Casas-Bedoya, A. Read, P. Atanackovic, S. G. Duvall, S. Palomba, B. Luther-Davies, S. Madden, D. J. Moss, and B. J. Eggleton, "Midinfrared supercontinuum generation from 2 to 6 μm in a silicon nanowire," Optica **2**(9), 797 (2015).

[6] R. Shankar, I. Bulu, and M. Lončar, "Integrated high-quality factor silicon-on-sapphire ring resonators for the mid-infrared," Appl. Phys. Lett. **102**(5), 051,108 (2013).

[7] X. Ji, F. A. S. Barbosa, S. P. Roberts, A. Dutt, J. Cardenas, Y. Okawachi, A. Bryant, A. L. Gaeta, and M. Lipson, "Ultra-low-loss on-chip resonators with sub-milliwatt parametric oscillation threshold," Optica **4**(6), 619–624 (2017).

[8] Y. Xuan, Y. Liu, L. T. Varghese, A. J. Metcalf, X. Xue, P.-H. Wang, K. Han, J. A. Jaramillo-Villegas, A. A. Noman, C. Wang, S. Kim, M. Teng, Y. J. Lee, B. Niu, L. Fan, J. Wang, D. E. Leaird, A. M. Weiner, and M. Qi, "High-Q silicon nitride microresonators exhibiting low-power frequency comb initiation," Optica **3**(11), 1171–1180 (2016).

[9] K. Luke, Y. Okawachi, M. R. E. Lamont, A. L. Gaeta, and M. Lipson, "Broadband mid-infrared frequency comb generation in a Si_3N_4 microresonator," Opt. Lett. **40**(21), 4823–4826 (2015).

[10] T. Udem, R. Holzwarth, and T. W. Hänsch, "Optical frequency metrology," Nature **416**, 233–237 (2002).

[11] S. T. Cundiff and J. Ye, "Colloquium: Femtosecond optical frequency combs," Rev. Mod. Phys. **75**(1), 325–342 (2003).

[12] V. Brasch, M. Geiselmann, T. Herr, G. Lihachev, M. H. P. Pfeiffer, M. L. Gorodetsky, and T. J. Kippenberg, "Photonic chip–based optical frequency comb using soliton Cherenkov radiation," Science **351**(6271), 357–360 (2016).

[13] Y. Okawachi, K. Saha, J. S. Levy, Y. H. Wen, M. Lipson, and A. L. Gaeta, "Octave-spanning frequency comb generation in a silicon nitride chip," Opt. Lett. **36**(17), 3398–3400 (2011).

[14] Y. Okawachi, M. R. E. Lamont, K. Luke, D. O. Carvalho, M. Yu, M. Lipson, and A. L. Gaeta, "Bandwidth shaping of microresonator-based frequency combs via dispersion engineering," Opt. Lett. **39**(12), 3535–3538 (2014).

[15] S. H. Lee, D. Y. Oh, Q.-F. Yang, B. Shen, H. Wang, K. Y. Yang, Y.-H. Lai, X. Yi, X. Li, and K. Vahala, "Towards visible soliton microcomb generation," Nat. Commun. **8**(1), 1295 (2017).

[16] T. Herr, V. Brasch, J. D. Jost, C. Y. Wang, N. M. Kondratiev, M. L. Gorodetsky, and T. J. Kippenberg, "Temporal solitons in optical microresonators," Nat. Photonics **8**(2), 145–152 (2014).

[17] P. Del'Haye, T. Herr, E. Gavartin, M. L. Gorodetsky, R. Holzwarth, and T. J. Kippenberg, "Octave Spanning Tunable Frequency Comb from a Microresonator," Phys. Rev. Lett. **107**(6), 063,901 (2011).

[18] H. Jung, K. Y. Fong, C. Xiong, and H. X. Tang, "Electrical tuning and switching of an optical frequency comb generated in aluminum nitride microring resonators," Opt. Lett. **39**(1), 84–87 (2014).

[19] H. Jung, C. Xiong, K. Y. Fong, X. Zhang, and H. X. Tang, "Optical frequency comb generation from aluminum nitride microring resonator," Opt. Lett. **38**(15), 2810–2813 (2013).

[20] K. Saha, Y. Okawachi, B. Shim, J. S. Levy, R. Salem, A. R. Johnson, M. A. Foster, M. R. E. Lamont, M. Lipson, and A. L. Gaeta, "Modelocking and

femtosecond pulse generation in chip-based frequency combs," Opt. Express **21**(1), 1335–1343 (2013).

[21] C. Joshi, J. K. Jang, K. Luke, X. Ji, S. A. Miller, A. Klenner, Y. Okawachi, M. Lipson, and A. L. Gaeta, "Thermally controlled comb generation and soliton modelocking in microresonators," Opt. Lett. **41**(11), 2565–2568 (2016).

[22] X. Yi, Q.-F. Yang, K. Y. Yang, M.-G. Suh, and K. Vahala, "Soliton frequency comb at microwave rates in a high-Q silica microresonator," Optica **2**(12), 1078–1085 (2015).

[23] B. J. M. Hausmann, I. Bulu, V. Venkataraman, P. Deotare, and M. Lončar, "Diamond nonlinear photonics," Nat. Photonics **8**(5), 369–374 (2014).

[24] A. A. Savchenkov, D. Eliyahu, W. Liang, V. S. Ilchenko, J. Byrd, A. B. Matsko, D. Seidel, and L. Maleki, "Stabilization of a Kerr frequency comb oscillator," Opt. Lett. **38**(15), 2636–2639 (2013).

[25] X. Xue, Y. Xuan, Y. Liu, P.-H. Wang, S. Chen, J. Wang, D. E. Leaird, M. Qi, and A. M. Weiner, "Mode-locked dark pulse Kerr combs in normal-dispersion microresonators," Nat. Photonics **9**(9), 594–600 (2015).

[26] N. Volet, X. Yi, Q.-F. Yang, E. J. Stanton, P. A. Morton, K. Y. Yang, K. J. Vahala, and J. E. Bowers, "Micro-Resonator Soliton Generated Directly with a Diode Laser," Laser Photonics Rev. **0**(0), 1700,307 (2018).

[27] M. Pu, L. Ottaviano, E. Semenova, and K. Yvind, "Efficient frequency comb generation in AlGaAs-on-insulator," Optica **3**(8), 823 (2016).

[28] D. J. Wilson, D. J. Wilson, S. Hönl, K. Schneider, M. Anderson, T. J. Kippenberg, and P. Seidler, "Gallium Phosphide Microresonator Frequency Combs," in *Conference on Lasers and Electro-Optics, paper SW3A.1*, p. SW3A.1 (Optical Society of America, 2018).

[29] C. Wang, M. Zhang, R. Zhu, R. Zhu, H. Hu, H. Hu, H. Chen, and M. Lončar, "On-Chip Kerr Frequency Comb Generation in Lithium Niobate Microresonators," in *Conference on Lasers and Electro-Optics, paper SW4M.3*, p. SW4M.3 (Optical Society of America, 2018).

[30] X. Liu, C. Sun, B. Xiong, L. Wang, J. Wang, Y. Han, Z. Hao, H. Li, Y. Luo, J. Yan, T. Wei, Y. Zhang, and J. Wang, "Integrated High-Q Crystalline AlN

Microresonators for Broadband Kerr and Raman Frequency Combs," ACS Photonics **5**(5), 1943–1950 (2018).

[31] C. Y. Wang, T. Herr, P. Del'Haye, A. Schliesser, J. Hofer, R. Holzwarth, T. W. Hänsch, N. Picqué, and T. J. Kippenberg, "Mid-infrared optical frequency combs at 2.5 μm based on crystalline microresonators," Nat. Commun. **4**, 1345 (2013).

[32] M. Yu, Y. Okawachi, A. G. Griffith, M. Lipson, and A. L. Gaeta, "Mode-locked mid-infrared frequency combs in a silicon microresonator," Optica **3**(8), 854–860 (2016).

[33] W. Liang, D. Eliyahu, V. S. Ilchenko, A. A. Savchenkov, A. B. Matsko, D. Seidel, and L. Maleki, "High spectral purity Kerr frequency comb radio frequency photonic oscillator," Nat. Commun. **6**, 7957 (2015).

[34] M. Yu, Y. Okawachi, A. G. Griffith, N. Picqué, M. Lipson, and A. L. Gaeta, "Silicon-chip-based mid-infrared dual-comb spectroscopy," Nat. Commun. **9**(1), 1869 (2018).

[35] M.-G. Suh, Q.-F. Yang, K. Y. Yang, X. Yi, and K. J. Vahala, "Microresonator soliton dual-comb spectroscopy," Science **354**(6312), 600–603 (2016).

[36] N. G. Pavlov, G. Lihachev, S. Koptyaev, E. Lucas, M. Karpov, N. M. Kondratiev, I. A. Bilenko, T. J. Kippenberg, and M. L. Gorodetsky, "Soliton dual frequency combs in crystalline microresonators," Opt. Lett. **42**(3), 514–517 (2017).

[37] A. Dutt, C. Joshi, X. Ji, J. Cardenas, Y. Okawachi, K. Luke, A. L. Gaeta, and M. Lipson, "On-chip dual-comb source for spectroscopy," Sci. Adv. **4**(3), e1701,858 (2018).

[38] P. Trocha, M. Karpov, D. Ganin, M. H. P. Pfeiffer, A. Kordts, S. Wolf, J. Krockenberger, P. Marin-Palomo, C. Weimann, S. Randel, W. Freude, T. J. Kippenberg, and C. Koos, "Ultrafast optical ranging using microresonator soliton frequency combs," Science **359**(6378), 887–891 (2018).

[39] M.-G. Suh and K. J. Vahala, "Soliton microcomb range measurement," Science **359**(6378), 884–887 (2018).

[40] D. T. Spencer, T. Drake, T. C. Briles, J. Stone, L. C. Sinclair, C. Fredrick, Q. Li, D. Westly, B. R. Ilic, A. Bluestone, N. Volet, T. Komljenovic,

L. Chang, S. H. Lee, D. Y. Oh, M.-G. Suh, K. Y. Yang, M. H. P. Pfeiffer, T. J. Kippenberg, E. Norberg, L. Theogarajan, K. Vahala, N. R. Newbury, K. Srinivasan, J. E. Bowers, S. A. Diddams, and S. B. Papp, "An optical-frequency synthesizer using integrated photonics," Nature **557**(7703), 81–85 (2018).

[41] J. Pfeifle, V. Brasch, M. Lauermann, Y. Yu, D. Wegner, T. Herr, K. Hartinger, P. Schindler, J. Li, D. Hillerkuss, R. Schmogrow, C. Weimann, R. Holzwarth, W. Freude, J. Leuthold, T. J. Kippenberg, and C. Koos, "Coherent terabit communications with microresonator Kerr frequency combs," Nat. Photonics **8**(5), 375–380 (2014).

[42] M.-G. Suh, X. Yi, Y.-H. Lai, S. Leifer, I. S. Grudinin, G. Vasisht, E. C. Martin, M. P. Fitzgerald, G. Doppmann, J. Wang, D. Mawet, S. B. Papp, S. A. Diddams, C. Beichman, and K. Vahala, "Searching for Exoplanets Using a Microresonator Astrocomb," arXiv:1801.05174 (2018).

[43] E. Obrzud, M. Rainer, A. Harutyunyan, M. H. Anderson, M. Geiselmann, B. Chazelas, S. Kundermann, S. Lecomte, M. Cecconi, A. Ghedina, E. Molinari, F. Pepe, F. Wildi, F. Bouchy, T. J. Kippenberg, and T. Herr, "A Microphotonic Astrocomb," arXiv:1712.09526 (2017).

[44] L. A. Lugiato and R. Lefever, "Spatial Dissipative Structures in Passive Optical Systems," Phys. Rev. Lett. **58**(21), 2209–2211 (1987).

[45] M. Haelterman, S. Trillo, and S. Wabnitz, "Dissipative modulation instability in a nonlinear dispersive ring cavity," Optics Communications **91**(5), 401–407 (1992).

[46] A. B. Matsko, A. A. Savchenkov, W. Liang, V. S. Ilchenko, D. Seidel, and L. Maleki, "Mode-locked Kerr frequency combs," Opt. Lett. **36**(15), 2845–2847 (2011).

[47] Y. K. Chembo and C. R. Menyuk, "Spatiotemporal Lugiato-Lefever formalism for Kerr-comb generation in whispering-gallery-mode resonators," Phys. Rev. A **87**(5), 053,852 (2013).

[48] S. Coen and M. Erkintalo, "Universal scaling laws of Kerr frequency combs," Opt. Lett. **38**(11), 1790–1792 (2013).

[49] M. R. E. Lamont, Y. Okawachi, and A. L. Gaeta, "Route to stabilized ultrabroadband microresonator-based frequency combs," Opt. Lett. **38**(18), 3478–3481 (2013).

[50] F. Leo, S. Coen, P. Kockaert, S.-P. Gorza, P. Emplit, and M. Haelterman, "Temporal cavity solitons in one-dimensional Kerr media as bits in an all-optical buffer," Nat. Photonics **4**(7), 471–476 (2010).

[51] F. Leo, L. Gelens, P. Emplit, M. Haelterman, and S. Coen, "Dynamics of one-dimensional Kerr cavity solitons," Opt. Express **21**(7), 9180–9191 (2013).

[52] J. K. Jang, M. Erkintalo, S. G. Murdoch, and S. Coen, "Ultraweak long-range interactions of solitons observed over astronomical distances," Nat. Photonics **7**(8), 657–663 (2013).

[53] K. Luo, J. K. Jang, S. Coen, S. G. Murdoch, and M. Erkintalo, "Spontaneous creation and annihilation of temporal cavity solitons in a coherently driven passive fiber resonator," Opt. Lett. **40**(16), 3735–3738 (2015).

[54] S. Wabnitz, "Suppression of interactions in a phase-locked soliton optical memory," Opt. Lett. **18**(8), 601–603 (1993).

[55] D. Turaev, A. G. Vladimirov, and S. Zelik, "Long-Range Interaction and Synchronization of Oscillating Dissipative Solitons," Phys. Rev. Lett. **108**(26), 263,906 (2012).

[56] P. Parra-Rivas, D. Gomila, M. A. Matías, S. Coen, and L. Gelens, "Dynamics of localized and patterned structures in the Lugiato-Lefever equation determine the stability and shape of optical frequency combs," Phys. Rev. A **89**(4), 043,813 (2014).

[57] C. Bao, J. A. Jaramillo-Villegas, Y. Xuan, D. E. Leaird, M. Qi, and A. M. Weiner, "Observation of Fermi-Pasta-Ulam Recurrence Induced by Breather Solitons in an Optical Microresonator," Phys. Rev. Lett. **117**(16), 163,901 (2016).

[58] C. Godey, I. V. Balakireva, A. Coillet, and Y. K. Chembo, "Stability analysis of the spatiotemporal Lugiato-Lefever model for Kerr optical frequency combs in the anomalous and normal dispersion regimes," Phys. Rev. A **89**(6), 063,814 (2014).

[59] H. Zhou, S.-W. Huang, Y. Dong, M. Liao, K. Qiu, and C. W. Wong, "Stability and Intrinsic Fluctuations of Dissipative Cavity Solitons in Kerr Frequency Microcombs," IEEE Photonics J. **7**(3), 1–13 (2015).

[60] S. Coen, H. G. Randle, T. Sylvestre, and M. Erkintalo, "Modeling of octave-spanning Kerr frequency combs using a generalized mean-field Lugiato–Lefever model," Opt. Lett. **38**(1), 37–39 (2013).

[61] D. C. Cole, J. R. Stone, and S. B. Papp, "Direct generation of solitons with a reversed soliton step in a microresonator pumped by a phase-modulated laser," in *Conference on Lasers and Electro-Optics (2018), paper SW3A.6*, p. SW3A.6 (Optical Society of America, 2018).

[62] E. Obrzud, S. Lecomte, and T. Herr, "Temporal solitons in microresonators driven by optical pulses," Nat. Photonics **11**(9), 600–607 (2017).

[63] C. Bao, Y. Xuan, D. E. Leaird, S. Wabnitz, M. Qi, and A. M. Weiner, "Spatial mode-interaction induced single soliton generation in microresonators," Optica **4**(9), 1011–1015 (2017).

[64] M. Zhang, C. Wang, B. Buscaino, A. Shams-Ansari, A. Shams-Ansari, J. M. Kahn, and M. Loncar, "Electro-optic Frequency Comb Generation in Ultrahigh-Q Integrated Lithium Niobate Micro-resonators," in *Conference on Lasers and Electro-Optics, paper FW3E.4*, p. FW3E.4 (Optical Society of America, 2018).

[65] B. Stern, X. Ji, Y. Okawachi, A. L. Gaeta, and M. Lipson, "Fully integrated ultra-low power Kerr comb generation," ArXiv180400357 Phys. (2018). 1804.00357.

[66] F. C. Cruz, D. L. Maser, T. Johnson, G. Ycas, A. Klose, F. R. Giorgetta, I. Coddington, and S. A. Diddams, "Mid-infrared optical frequency combs based on difference frequency generation for molecular spectroscopy," Opt. Express **23**(20), 26,814–26,824 (2015).

[67] I. Pupeza, D. Sánchez, J. Zhang, N. Lilienfein, M. Seidel, N. Karpowicz, T. Paasch-Colberg, I. Znakovskaya, M. Pescher, W. Schweinberger, V. Pervak, E. Fill, O. Pronin, Z. Wei, F. Krausz, A. Apolonski, and J. Biegert, "High-power sub-two-cycle mid-infrared pulses at 100 MHz repetition rate," Nat. Photonics **9**(11), 721–724 (2015).

[68] C. R. Phillips, J. Jiang, C. Mohr, A. C. Lin, C. Langrock, M. Snure, D. Bliss, M. Zhu, I. Hartl, J. S. Harris, M. E. Fermann, and M. M. Fejer, "Widely tunable midinfrared difference frequency generation in orientation-patterned GaAs pumped with a femtosecond Tm-fiber system," Opt. Lett. **37**(14), 2928–2930 (2012).

[69] A. Gambetta, N. Coluccelli, M. Cassinerio, D. Gatti, P. Laporta, G. Galzerano, and M. Marangoni, "Milliwatt-level frequency combs in the 8 μm range via difference frequency generation from an Er:fiber oscillator," Opt. Lett. **38**(7), 1155–1157 (2013).

[70] F. Adler, K. C. Cossel, M. J. Thorpe, I. Hartl, M. E. Fermann, and J. Ye, "Phase-stabilized, 1.5 W frequency comb at 2.8–4.8 μm," Opt. Lett. **34**(9), 1330–1332 (2009).

[71] L. Maidment, P. G. Schunemann, and D. T. Reid, "Molecular fingerprint-region spectroscopy from 5 to 12 μm using an orientation-patterned gallium phosphide optical parametric oscillator," Opt. Lett. **41**(18), 4261–4264 (2016).

[72] V. O. Smolski, H. Yang, S. D. Gorelov, P. G. Schunemann, and K. L. Vodopyanov, "Coherence properties of a 2.6–7.5 μm frequency comb produced as a subharmonic of a Tm-fiber laser," Opt. Lett. **41**(7), 1388–1391 (2016).

[73] M. Vainio and J. Karhu, "Fully stabilized mid-infrared frequency comb for high-precision molecular spectroscopy," Opt. Express **25**(4), 4190–4200 (2017).

[74] S. Antipov, D. D. Hudson, A. Fuerbach, and S. D. Jackson, "High-power mid-infrared femtosecond fiber laser in the water vapor transmission window," Optica **3**(12), 1373–1376 (2016).

[75] S. Duval, M. Bernier, V. Fortin, J. Genest, M. Piché, and R. Vallée, "Femtosecond fiber lasers reach the mid-infrared," Optica **2**(7), 623–626 (2015).

[76] X. Gai, Y. Yu, B. Kuyken, P. Ma, S. J. Madden, J. V. Campenhout, P. Verheyen, G. Roelkens, R. Baets, and B. Luther-Davies, "Nonlinear absorption and refraction in crystalline silicon in the mid-infrared," Laser Photonics Rev. **7**(6), 1054–1064 (2013).

[77] K. C. Cossel, E. M. Waxman, I. A. Finneran, G. A. Blake, J. Ye, and N. R. Newbury, "Gas-phase broadband spectroscopy using active sources: progress, status, and applications [Invited]," J. Opt. Soc. Am. B, JOSAB **34**(1), 104–129 (2017).

[78] I. Coddington, N. Newbury, and W. Swann, "Dual-comb spectroscopy," Optica **3**(4), 414–426 (2016).

[79] T. J. Kippenberg, R. Holzwarth, and S. A. Diddams, "Microresonator-Based Optical Frequency Combs," Science **332**(6029), 555–559 (2011).

[80] J. S. Levy, A. Gondarenko, M. A. Foster, A. C. Turner-Foster, A. L. Gaeta, and M. Lipson, "CMOS-compatible multiple-wavelength oscillator for on-chip optical interconnects," Nat. Photonics **4**(1), 37–40 (2010).

[81] T. Herr, K. Hartinger, J. Riemensberger, C. Y. Wang, E. Gavartin, R. Holzwarth, M. L. Gorodetsky, and T. J. Kippenberg, "Universal formation dynamics and noise of Kerr-frequency combs in microresonators," Nat. Photonics **6**(7), 480–487 (2012).

[82] S. B. Papp, K. Beha, P. Del'Haye, F. Quinlan, H. Lee, K. J. Vahala, and S. A. Diddams, "Microresonator frequency comb optical clock," Optica **1**(1), 10–14 (2014).

[83] Y. Liu, Y. Xuan, X. Xue, P.-H. Wang, S. Chen, A. J. Metcalf, J. Wang, D. E. Leaird, M. Qi, and A. M. Weiner, "Investigation of mode coupling in normal-dispersion silicon nitride microresonators for Kerr frequency comb generation," Optica **1**(3), 137–144 (2014).

[84] S.-W. Huang, H. Zhou, J. Yang, J. F. McMillan, A. Matsko, M. Yu, D.-L. Kwong, L. Maleki, and C. W. Wong, "Mode-Locked Ultrashort Pulse Generation from On-Chip Normal Dispersion Microresonators," Phys. Rev. Lett. **114**(5), 053,901 (2015).

[85] A. A. Savchenkov, V. S. Ilchenko, F. D. Teodoro, P. M. Belden, W. T. Lotshaw, A. B. Matsko, and L. Maleki, "Generation of Kerr combs centered at 4.5 ¯m in crystalline microresonators pumped with quantum-cascade lasers," Opt. Lett. **40**(15), 3468–3471 (2015).

[86] A. Schliesser, N. Picqué, and T. W. Hänsch, "Mid-infrared frequency combs," Nat. Photonics **6**(7), 440–449 (2012).

[87] I. Coddington, W. C. Swann, and N. R. Newbury, "Coherent Multiheterodyne Spectroscopy Using Stabilized Optical Frequency Combs," Phys. Rev. Lett. **100**(1), 013,902 (2008).

[88] B. Bernhardt, A. Ozawa, P. Jacquet, M. Jacquey, Y. Kobayashi, T. Udem, R. Holzwarth, G. Guelachvili, T. W. Hänsch, and N. Picqué, "Cavity-enhanced dual-comb spectroscopy," Nat. Photonics **4**(1), 55–57 (2010).

[89] F. Adler, P. Masłowski, A. Foltynowicz, K. C. Cossel, T. C. Briles, I. Hartl, and J. Ye, "Mid-infrared Fourier transform spectroscopy with a broadband frequency comb," Opt. Express **18**(21), 21,861–21,872 (2010).

[90] M. A. Foster, J. S. Levy, O. Kuzucu, K. Saha, M. Lipson, and A. L. Gaeta, "A Silicon-Based Monolithic Optical Frequency Comb Source," Opt. Express **19**(15), 14,233–14,239 (2011).

[91] T. Herr, V. Brasch, J. D. Jost, I. Mirgorodskiy, G. Lihachev, M. L. Gorodetsky, and T. J. Kippenberg, "Mode Spectrum and Temporal Soliton Formation in Optical Microresonators," Phys. Rev. Lett. **113**(12), 123,901 (2014).

[92] H. Guo, M. Karpov, E. Lucas, A. Kordts, M. H. P. Pfeiffer, V. Brasch, G. Lihachev, V. E. Lobanov, M. L. Gorodetsky, and T. J. Kippenberg, "Universal dynamics and deterministic switching of dissipative Kerr solitons in optical microresonators," Nat. Phys. **13**(1), 94–102 (2017).

[93] F. Zhu, A. Bicer, R. Askar, J. Bounds, A. A. Kolomenskii, V. Kelessides, M. Amani, and H. A. Schuessler, "Mid-infrared dual frequency comb spectroscopy based on fiber lasers for the detection of methane in ambient air," Laser Phys. Lett. **12**(9), 095,701 (2015).

[94] A. Griffith, J. Cardenas, C. B. Poitras, and M. Lipson, "High quality factor and high confinement silicon resonators using etchless process," Opt. Express **20**(19), 21,341–21,345 (2012).

[95] H. Rong, A. Liu, R. Jones, O. Cohen, D. Hak, R. Nicolaescu, A. Fang, and M. Paniccia, "An all-silicon Raman laser," Nature **433**(7023), 292–294 (2005).

[96] A. C. Turner-Foster, M. A. Foster, J. S. Levy, C. B. Poitras, R. Salem, A. L. Gaeta, and M. Lipson, "Ultrashort free-carrier lifetime in low-loss silicon nanowaveguides," Opt. Express **18**(4), 3582–3591 (2010).

[97] R. K. W. Lau, M. R. E. Lamont, Y. Okawachi, and A. L. Gaeta, "Effects of multiphoton absorption on parametric comb generation in silicon microresonators," Opt. Lett. **40**(12), 2778–2781 (2015).

[98] T. Hansson, D. Modotto, and S. Wabnitz, "Mid-infrared soliton and Raman frequency comb generation in silicon microrings," Opt. Lett. **39**(23), 6747–6750 (2014).

[99] T. J. Kippenberg, S. M. Spillane, and K. J. Vahala, "Kerr-Nonlinearity Optical Parametric Oscillation in an Ultrahigh-Q Toroid Microcavity," Phys. Rev. Lett. **93**(8), 083,904 (2004).

[100] X. Xue, Y. Xuan, C. Wang, P.-H. Wang, Y. Liu, B. Niu, D. E. Leaird, M. Qi, and A. M. Weiner, "Thermal tuning of Kerr frequency combs in silicon nitride microring resonators," Opt. Express **24**(1), 687–698 (2016).

[101] K. Ikeda, R. E. Saperstein, N. Alic, and Y. Fainman, "Thermal and Kerr nonlinear properties of plasma-deposited silicon nitride/silicon dioxide waveguides," Opt. Express **16**(17), 12,987–12,994 (2008).

[102] N. Akhmediev and A. Ankiewicz, eds., *Dissipative Solitons: From Optics to Biology and Medicine*, Lecture Notes in Physics (Springer-Verlag, Berlin Heidelberg, 2008).

[103] P. Del'Haye, A. Schliesser, O. Arcizet, T. Wilken, R. Holzwarth, and T. J. Kippenberg, "Optical frequency comb generation from a monolithic microresonator," Nature **450**(7173), 1214–1217 (2007).

[104] L. Razzari, D. Duchesne, M. Ferrera, R. Morandotti, S. Chu, B. E. Little, and D. J. Moss, "CMOS-compatible integrated optical hyper-parametric oscillator," Nat. Photonics **4**(1), 41–45 (2010).

[105] F. Ferdous, H. Miao, D. E. Leaird, K. Srinivasan, J. Wang, L. Chen, L. T. Varghese, and A. M. Weiner, "Spectral line-by-line pulse shaping of on-chip microresonator frequency combs," Nat. Photonics **5**(12), 770–776 (2011).

[106] A. B. Matsko, A. A. Savchenkov, and L. Maleki, "On excitation of breather solitons in an optical microresonator," Opt. Lett. **37**(23), 4856–4858 (2012).

[107] M. Remoissenet, *Waves Called Solitons: Concepts and Experiments* (Springer-Verlag, Berlin Heidelberg, 1994).

[108] K. Nozaki and N. Bekki, "Chaotic Solitons in a Plasma Driven by an rf Field," J. Phys. Soc. Jpn. **54**(7), 2363–2366 (1985).

[109] M. Anderson, F. Leo, S. Coen, M. Erkintalo, and S. G. Murdoch, "Observations of spatiotemporal instabilities of temporal cavity solitons," Optica **3**(10), 1071–1074 (2016).

[110] B. Bernhardt, E. Sorokin, P. Jacquet, R. Thon, T. Becker, I. T. Sorokina, N. Picqué, and T. W. Hänsch, "Mid-infrared dual-comb spectroscopy with 2.4 μm Cr^{2+}:ZnSe femtosecond lasers," Appl. Phys. B **100**(1), 3–8 (2010).

[111] E. Baumann, F. R. Giorgetta, W. C. Swann, A. M. Zolot, I. Coddington, and N. R. Newbury, "Spectroscopy of the methane $\nu 3$ band with an accurate midinfrared coherent dual-comb spectrometer," Phys. Rev. A **84**(6), 062,513 (2011).

[112] T. Ideguchi, S. Holzner, B. Bernhardt, G. Guelachvili, N. Picqué, and T. W. Hänsch, "Coherent Raman spectro-imaging with laser frequency combs," Nature **502**(7471), 355–358 (2013).

[113] T. Ideguchi, B. Bernhardt, G. Guelachvili, T. W. Hänsch, and N. Picqué, "Raman-induced Kerr-effect dual-comb spectroscopy," Opt. Lett. **37**(21), 4498–4500 (2012).

[114] Z. Zhang, T. Gardiner, and D. T. Reid, "Mid-infrared dual-comb spectroscopy with an optical parametric oscillator," Opt. Lett. **38**(16), 3148–3150 (2013).

[115] G. Villares, A. Hugi, S. Blaser, and J. Faist, "Dual-comb spectroscopy based on quantum-cascade-laser frequency combs," Nat. Commun. **5**, 5192 (2014).

[116] D. A. Long, A. J. Fleisher, K. O. Douglass, S. E. Maxwell, K. Bielska, J. T. Hodges, and D. F. Plusquellic, "Multiheterodyne spectroscopy with optical frequency combs generated from a continuous-wave laser," Opt. Lett. **39**(9), 2688–2690 (2014).

[117] Y. Wang, M. G. Soskind, W. Wang, and G. Wysocki, "High-resolution multi-heterodyne spectroscopy based on Fabry-Perot quantum cascade lasers," Appl. Phys. Lett. **104**(3), 031,114 (2014).

[118] Y. Jin, S. M. Cristescu, F. J. M. Harren, and J. Mandon, "Femtosecond optical parametric oscillators toward real-time dual-comb spectroscopy," Appl. Phys. B **119**(1), 65–74 (2015).

[119] P. Martín-Mateos, B. Jerez, and P. Acedo, "Dual electro-optic optical frequency combs for multiheterodyne molecular dispersion spectroscopy," Opt. Express **23**(16), 21,149–21,158 (2015).

[120] V. Durán, S. Tainta, and V. Torres-Company, "Ultrafast electrooptic dual-comb interferometry," Opt. Express **23**(23), 30,557–30,569 (2015).

[121] M. Yan, P.-L. Luo, K. Iwakuni, G. Millot, T. W. Hänsch, and N. Picqué, "Mid-infrared dual-comb spectroscopy with electro-optic modulators," Light Sci. Appl. **6**(10), e17,076 (2017).

[122] V. O. Smolski, H. Yang, J. Xu, and K. L. Vodopyanov, "Massively parallel dual-comb molecular detection with subharmonic optical parametric oscillators," arXiv:1608.07318 (2016).

[123] B. Süss, F. Ringleb, and J. Heberle, "New ultrarapid-scanning interferometer for FT-IR spectroscopy with microsecond time-resolution," Review of Scientific Instruments **87**(6), 063,113 (2016).

[124] M. Vainio and L. Halonen, "Mid-infrared optical parametric oscillators and frequency combs for molecular spectroscopy," Phys. Chem. Chem. Phys. **18**(6), 4266–4294 (2016).

[125] B. Spaun, P. B. Changala, D. Patterson, B. J. Bjork, O. H. Heckl, J. M. Doyle, and J. Ye, "Continuous probing of cold complex molecules with infrared frequency comb spectroscopy," Nature **533**(7604), 517–520 (2016).

[126] D. J. Jones, S. A. Diddams, J. K. Ranka, A. Stentz, R. S. Windeler, J. L. Hall, and S. T. Cundiff, "Carrier-Envelope Phase Control of Femtosecond Mode-Locked Lasers and Direct Optical Frequency Synthesis," Science **288**(5466), 635–639 (2000).

[127] A. Marian, M. C. Stowe, J. R. Lawall, D. Felinto, and J. Ye, "United Time-Frequency Spectroscopy for Dynamics and Global Structure," Science **306**(5704), 2063–2068 (2004).

[128] S. A. Diddams, L. Hollberg, and V. Mbele, "Molecular fingerprinting with the resolved modes of a femtosecond laser frequency comb," Nature **445**(7128), 627–630 (2007).

[129] G. Millot, S. Pitois, M. Yan, T. Hovhannisyan, A. Bendahmane, T. W. Hänsch, and N. Picqué, "Frequency-agile dual-comb spectroscopy," Nat. Photonics **10**(1), 27–30 (2016).

[130] S. Okubo, K. Iwakuni, H. Inaba, K. Hosaka, A. Onae, H. Sasada, and F.-

L. Hong, "Ultra-broadband dual-comb spectroscopy across 1.0–1.9 ¯m," Appl. Phys. Express **8**(8), 082,402 (2015).

[131] P. Maslowski, K. F. Lee, A. C. Johansson, A. Khodabakhsh, G. Kowzan, L. Rutkowski, A. A. Mills, C. Mohr, J. Jiang, M. E. Fermann, and A. Foltynowicz, "Surpassing the path-limited resolution of Fourier-transform spectrometry with frequency combs," Phys. Rev. A **93**(2), 021,802 (2016).

[132] C. Gohle, B. Stein, A. Schliesser, T. Udem, and T. W. Hänsch, "Frequency Comb Vernier Spectroscopy for Broadband, High-Resolution, High-Sensitivity Absorption and Dispersion Spectra," Phys. Rev. Lett. **99**(26), 263,902 (2007).

[133] M. Siciliani de Cumis, R. Eramo, N. Coluccelli, M. Cassinerio, G. Galzerano, P. Laporta, P. De Natale, and P. Cancio Pastor, "Tracing part-per-billion line shifts with direct-frequency-comb Vernier spectroscopy," Phys. Rev. A **91**(1), 012,505 (2015).

[134] A. Gambetta, M. Cassinerio, D. Gatti, P. Laporta, and G. Galzerano, "Scanning micro-resonator direct-comb absolute spectroscopy," Sci. Rep. **6**, 35,541 (2016).

[135] N. Coluccelli, M. Cassinerio, B. Redding, H. Cao, P. Laporta, and G. Galzerano, "The optical frequency comb fibre spectrometer," Nat. Commun. **7**, 12,995 (2016).

[136] P. Jacquet, J. Mandon, B. Bernhardt, R. Holzwarth, G. Guelachvili, T. W. Hänsch, and N. Picqué, "Frequency Comb Fourier Transform Spectroscopy with kHz Optical Resolution," in *Advances in Imaging (2009), paper FMB2*, p. FMB2 (Optical Society of America, 2009).

[137] S. A. Meek, A. Hipke, G. Guelachvili, T. W. Hänsch, and N. Picqué, "Doppler-free Fourier transform spectroscopy," Opt. Lett. **43**(1), 162–165 (2018).

[138] L. Rutkowski, P. Masłowski, A. C. Johansson, A. Khodabakhsh, and A. Foltynowicz, "Optical frequency comb Fourier transform spectroscopy with sub-nominal resolution and precision beyond the Voigt profile," Journal of Quantitative Spectroscopy and Radiative Transfer **204**, 63–73 (2018).

[139] A. Hugi, G. Villares, S. Blaser, H. C. Liu, and J. Faist, "Mid-infrared frequency comb based on a quantum cascade laser," Nature **492**(7428), 229–233 (2012).

[140] P. Del'Haye, A. Coillet, T. Fortier, K. Beha, D. C. Cole, K. Y. Yang, H. Lee, K. J. Vahala, S. B. Papp, and S. A. Diddams, "Phase-coherent microwave-to-optical link with a self-referenced microcomb," Nat. Photonics **10**(8), 516–520 (2016).

[141] A. Spott, J. Peters, M. L. Davenport, E. J. Stanton, C. D. Merritt, W. W. Bewley, I. Vurgaftman, C. S. Kim, J. R. Meyer, J. Kirch, L. J. Mawst, D. Botez, and J. E. Bowers, "Quantum cascade laser on silicon," Optica **3**(5), 545–551 (2016).

[142] D. M. Kita, B. Miranda, D. Favela, D. Bono, J. Michon, H. Lin, T. Gu, and J. Hu, "Digital Fourier transform spectroscopy: a high-performance, scalable technology for on-chip spectrum analysis," arXiv:1802.05270 (2018).

[143] M.-G. Suh and K. Vahala, "Gigahertz-repetition-rate soliton microcombs," Optica **5**(1), 65–66 (2018).

[144] M. Yu, Y. Okawachi, A. G. Griffith, M. Lipson, and A. L. Gaeta, "Microresonator-based high-resolution gas spectroscopy," Opt. Lett. **42**(21), 4442–4445 (2017).

[145] A. R. Johnson, Y. Okawachi, M. R. E. Lamont, J. S. Levy, M. Lipson, and A. L. Gaeta, "Microresonator-based comb generation without an external laser source," Opt. Express **22**(2), 1394–1401 (2014).

[146] M. Peccianti, A. Pasquazi, Y. Park, B. E. Little, S. T. Chu, D. J. Moss, and R. Morandotti, "Demonstration of a stable ultrafast laser based on a nonlinear microcavity," Nat. Commun. **3**, 765 (2012).

[147] A. Pasquazi, L. Caspani, M. Peccianti, M. Clerici, M. Ferrera, L. Razzari, D. Duchesne, B. E. Little, S. T. Chu, D. J. Moss, and R. Morandotti, "Self-locked optical parametric oscillation in a CMOS compatible microring resonator: a route to robust optical frequency comb generation on a chip," Opt. Express **21**(11), 13,333–13,341 (2013).

[148] S. Ramelow, A. Farsi, S. Clemmen, J. S. Levy, A. R. Johnson, Y. Okawachi, M. R. E. Lamont, M. Lipson, and A. L. Gaeta, "Strong polarization mode coupling in microresonators," Opt. Lett. **39**(17), 5134–5137 (2014).

[149] B. Stern, X. Ji, A. Dutt, and M. Lipson, "Compact narrow-linewidth integrated laser based on a low-loss silicon nitride ring resonator," Opt. Lett. **42**(21), 4541–4544 (2017).

[150] H. Rong, R. Jones, A. Liu, O. Cohen, D. Hak, A. Fang, and M. Paniccia, "A continuous-wave Raman silicon laser," Nature **433**(7027), 725–728 (2005).

[151] R. Claps, D. Dimitropoulos, V. Raghunathan, Y. Han, and B. Jalali, "Observation of stimulated Raman amplification in silicon waveguides," Opt. Express **11**(15), 1731–1739 (2003).

[152] T. R. Hart, R. L. Aggarwal, and B. Lax, "Temperature Dependence of Raman Scattering in Silicon," Phys. Rev. B **1**(2), 638–642 (1970).

[153] Y. Y. Wang, C. Wu, F. Couny, M. G. Raymer, and F. Benabid, "Quantum-Fluctuation-Initiated Coherence in Multioctave Raman Optical Frequency Combs," Phys. Rev. Lett. **105**(12), 123,603 (2010).

[154] B. Min, L. Yang, and K. Vahala, "Controlled transition between parametric and Raman oscillations in ultrahigh-Q silica toroidal microcavities," Appl. Phys. Lett. **87**(18), 181,109 (2005).

[155] I. H. Agha, Y. Okawachi, M. A. Foster, J. E. Sharping, and A. L. Gaeta, "Four-wave-mixing parametric oscillations in dispersion-compensated high-Q silica microspheres," Phys. Rev. A **76**(4), 043,837 (2007).

[156] I. S. Grudinin, L. Baumgartel, and N. Yu, "Impact of cavity spectrum on span in microresonator frequency combs," Opt. Express **21**(22), 26,929–26,935 (2013).

[157] W. Liang, A. B. Matsko, A. A. Savchenkov, V. S. Ilchenko, D. Seidel, and L. Maleki, "Generation of Kerr combs in MgF2 and CaF2 microresonators," in *2011 Joint Conference of the IEEE International Frequency Control and the European Frequency and Time Forum (FCS) Proceedings*, pp. 1–6 (2011).

[158] P. Latawiec, V. Venkataraman, M. J. Burek, B. J. M. Hausmann, I. Bulu, and M. Lončar, "On-chip diamond Raman laser," Optica **2**(11), 924–928 (2015).

[159] S. Kumar and S. K. Biswas, "Impact of Kerr nonlinearity and stimulated Raman scattering on the whispering gallery modes of an optical microsphere," J. Opt. Soc. Am. B **33**(8), 1677–1687 (2016).

[160] X. Liu, C. Sun, B. Xiong, L. Wang, J. Wang, Y. Han, Z. Hao, H. Li, Y. Luo, J. Yan, T. Wei, Y. Zhang, and J. Wang, "Aluminum nitride-on-sapphire platform for integrated high-Q microresonators," Opt. Express **25**(2), 587–594 (2017).

[161] Q.-F. Yang, X. Yi, K. Y. Yang, and K. Vahala, "Stokes solitons in optical microcavities," Nat. Phys. **13**(1), 53–57 (2017).

[162] X. Yi, Q.-F. Yang, K. Y. Yang, and K. Vahala, "Theory and measurement of the soliton self-frequency shift and efficiency in optical microcavities," Opt. Lett. **41**(15), 3419–3422 (2016).

[163] M. Karpov, H. Guo, A. Kordts, V. Brasch, M. H. P. Pfeiffer, M. Zervas, M. Geiselmann, and T. J. Kippenberg, "Raman Self-Frequency Shift of Dissipative Kerr Solitons in an Optical Microresonator," Phys. Rev. Lett. **116**(10), 103,902 (2016).

[164] V. Raghunathan, D. Borlaug, R. R. Rice, and B. Jalali, "Demonstration of a Mid-infrared silicon Raman amplifier," Opt. Express **15**(22), 14,355–14,362 (2007).

[165] H. M. Pask, "The design and operation of solid-state Raman lasers," Progress in Quantum Electronics **27**(1), 3–56 (2003).

[166] V. G. Savitski, S. Reilly, and A. J. Kemp, "Steady-State Raman Gain in Diamond as a Function of Pump Wavelength," IEEE J. Quantum Electron. **49**(2), 218–223 (2013).

[167] "Optical Engineering of Diamond," https://www.wiley.com/en-us/Optical+Engineering+of+Diamond-p-9783527411023.